Pericyte and Microglia Reprogramming in Hypertensive Cerebral Small Vessel Disease

Thesis

for the degree of

doctor rerum naturalium

(Dr. rer. nat.)

approved by the Faculty of Natural Sciences of

Otto von Guericke University Magdeburg

By: M.D., M. Sc., Lorena Morton Moreno

Born on 10.10.1988 in Monterrey, Mexico

Examiners: Prof. Dr. rer. nat. habil. Ildiko Rita Dunay

Prof. Dr. med. Gabor Petzold

Submitted on: 04.06.2024

Defended on: 18.12.2024

Life is too short not to pour your soul into something

Research Contributions

A part of this work has been published under the following titles:

Morton L, Garza AP, Debska-Vielhaber G, Villafuerte LE, Henneicke S, Arndt P, Meuth SG, Schreiber S, Dunay IR. Pericytes and Extracellular Vesicle Interactions in Neurovascular Adaptation to Chronic Arterial Hypertension. J Am Heart Assoc. 2025 Jan 7;14(1):e038457. doi: 10.1161/JAHA.124.038457. Epub 2024 Dec 24. PMID: 39719419.

Morton L*, Arndt P*, Garza AP, Henneicke S, Mattern H, Gonzalez M, Dityatev A, Yilmazer-Hanke D, Schreiber S, Dunay IR. Spatio-temporal dynamics of microglia phenotype in human and murine cSVD: impact of acute and chronic hypertensive states. Acta Neuropathol Commun. 2023 Dec 19;11(1):204. doi: 10.1186/s40478-023-01672-0. PMID: 38115109; PMCID: PMC10729582.

Other scientific publications achieved during doctoral studies:

Khoshneviszadeh M, Henneicke S, Pirici D, Senthilnathan A, **Morton L**, Arndt P, Kaushik R, Norman O, Jukkola J, Dunay IR, Seidenbecher C, Heikkinen A, Schreiber S, Dityatev A. Microvascular damage, neuroinflammation and extracellular matrix remodeling in Col18a1 knockout mice as a model for early cerebral small vessel disease. Matrix Biol. 2024 Apr;128:39-64. doi: 10.1016/j.matbio.2024.02.007. Epub 2024 Feb 21. PMID: 38387749.

Binder LB, Rosa PB, de Sousa BM, Chagas LS, Dubljević O, Martineau FS, Mottarlini F, Castany S, **Morton L**, Krstanović F, Tassinari ID, Choconta JL,Pereira-Santos AR, Weinhard L, Pallegar PN, Vahsen BF, Lepiarz-Raba I, Compagnion AC, Lorente-Picón M. Neuro-immune interactions in health and disease: Insights from FENS-Hertie 2022 Winter School. Eur J Neurosci. 2024 Apr;59(8):1977-1992. doi: 10.1111/ejn.16262. Epub 2024 Feb 4. PMID: 38311960.

Schreiber S, Bernal J, Arndt P, Schreiber F, Müller P, **Morton L**, Braun-Dullaeus RC, Valdés-Hernández MDC, Duarte R, Wardlaw JM, Meuth SG, Mietzner G, Vielhaber S, Dunay IR, Dityatev A, Jandke S, Mattern H. Brain vascular health in ALS is mediated by the microvascular integrity of the motor cortex. Cells. 2023 Mar 21;12(6):957. doi: 10.3390/cells12060957. PMID: 36980297; PMCID: PMC10047140.

Garza AP*, **Morton L***, Pállinger É, Buzás EI, Schreiber S, Schott BH, Dunay IR. Initial and ongoing tobacco smoking elicits vascular damage and distinct inflammatory response linked to neurodegeneration. Brain Behav Immun Health. 2023 Jan 29;28:100597. doi: 10.1016/j.bbih.2023.100597. PMID: 36817509; PMCID: PMC9931921.

Ulbrich P*, **Morton L***, Briese M, Lämmlin N, Mattern H, Hasanuzzaman M, Westhues M, Khoshneviszadeh M, Appenzeller S, Gündel D, Toussaint M, Brust P, Kniess T, Oelschlegel A, Goldschmidt J, Meuth S, Heinze H-J, Debska-Vielhaber G, Vielhaber S, Becker A, Dityatev A, Jandke S, Sendtner M, Dunay I+, Schreiber S+. Vascular and neural transcriptomics reveal stage-dependent pathways to inflammation and cognitive dysfunction in a rat model of hypertension. bioRxiv. https://doi.org/10.1101/2023.01.20.524921. *Under Review J Neuroinflammation.*

Figueiredo CA, Steffen J, **Morton L**, Arumugam S, Liesenfeld O, Deli MA, Kröger A, Schüler T, Dunay IR. Immune response and pathogen invasion at the choroid plexus in the onset of cerebral toxoplasmosis. J Neuroinflammation. 2022 Jan 13;19(1):17. doi: 10.1186/s12974-021-02370-1. PMID: 35027063; PMCID: PMC8759173.

Dudeck J, Kotrba J, Immler R, Hoffmann A, Voss M, Alexaki VI, **Morton L**, Jahn SR, Katsoulis-Dimitriou K, Winzer S, Kollias G, Fischer T, Nedospasov SA, Dunay IR, Chavakis T, Müller AJ, Schraven B, Sperandio M, Dudeck A. Directional mast cell degranulation of tumor necrosis factor into blood vessels primes neutrophil extravasation. Immunity. 2021 Mar 9;54(3):468-483.e5. doi: 10.1016/j.immuni.2020.12.017. Epub 2021 Jan 22. PMID: 33484643.

Lang D, Schott BH, van Ham M, **Morton L**, Kulikovskaja L, Herrera-Molina R, Pielot R, Klawonn F, Montag D, Jänsch L, Gundelfinger ED, Smalla KH, Dunay IR. Chronic Toxoplasma infection is associated with distinct alterations in the synaptic protein composition. J Neuroinflammation. 2018 Aug 1;15(1):216. doi: 10.1186/s12974-018-1242-1. PMID: 30068357; PMCID: PMC6090988.

*These authors contributed equally

Abstract

Cerebral small vessel disease (cSVD) is the leading cause of stroke and dementia, yet its cellular and molecular mechanisms remain incompletely understood. This dissertation investigates the roles of pericytes and microglia, crucial components of the neurovascular unit, in the pathogenesis of hypertensive cSVD. Utilizing the Spontaneously Hypertensive Stroke-Prone Rat (SHRSP) model and human post-mortem brain tissue, this thesis investigates the phenotypic and metabolic changes these cells undergo under chronic hypertension. This research posits that chronic hypertension induces significant transformations in pericytes and microglia, exacerbating cSVD pathology. The aims include characterizing pericyte phenotypic alterations, investigating the metabolic profile of pericytes and their effects on blood-brain barrier (BBB) integrity, defining microglial activation states, and examining the impact of microglial reactivity on BBB dysfunction and neuroinflammation. An array of techniques was employed, including vascular and microglial single-cell isolation, immunofluorescence, flow cytometric analysis, and Seahorse XP metabolic analyses, along with gene expression profiling of vessel fragments, *in vitro* pericyte expansion, and extracellular vesicle (EVs) analysis. The findings in this thesis reveal the upregulation of genes involved in lipid metabolism, angiogenesis, and inflammation during early hypertension, indicating active vascular remodeling, which declines in late stages, suggesting metabolic exhaustion. Pericytes exhibit profound phenotypic and metabolic reprogramming towards glycolysis, with hypertensive plasma-derived EVs impairing mitochondrial function in control pericytes, highlighting the role of EVs in vascular pathology. Microglia show diverse phenotypic characteristics and activation states, suggesting a synergistic relationship between endothelial alterations, microglial reactivity, and aging, which contributes to cSVD. Chronic hypertension induces morphological changes in microglia, modifies BBB permeability, and promotes neuroinflammation. This dissertation proposes a novel pericyte-microglia lactate shuttle in which pericytes under hypertensive stress increase glycolysis, producing lactate that may be transferred to microglia via the MCT4 receptor. This shuttle can be crucial for understanding the metabolic dynamics of hypertensive cSVD, and represents a potential therapeutic target. This dissertation advances our understanding of cSVD pathogenesis by highlighting the potential of targeting metabolic pathways and EVs to mitigate vascular complications.

Table of Contents

List of Figures

List of Tables

List of Abbreviations

Abbreviation	Definition
Aβ	β-amyloid
ACD	acid citrate dextrose
AD	Alzheimer's disease
AG	aerobic glycolysis
Angpt1	angiopoietin 1
Anpep	alanyl aminopeptidase
ATP	adenosine triphosphate
BBB	blood-brain barrier
Bdkrb1	bradykinin receptor B1
BDNF	brain-derived neurotrophic factor
BHI	bioenergetic health index
BPTES	glutaminase inhibitor
BSA	bovine serum albumin
CADASIL	cerebral autosomal dominant arteriopathy with subcortical infarcts and leukoencephalopathy
CBF	cerebral blood flow
CCCP	carbonyl cyanide m-chlorophenyl hydrazone
Ccl2	chemokine (C-C motif) ligand 2
Ccl5	chemokine (C-C motif) ligand 5
CD13	aminopeptidase N / Anpep
CD31	platelet endothelial cell adhesion molecule-1
CNS	central nervous system
Ctrl	Control
Cspg4	chondroitin sulfate proteoglycan 4
CX3CR1	CX3C chemokine receptor 1
DAMs	Disease associated microglia
DMEM/F12	Dulbecco's Modified Eagle Medium/Nutrient Mixture F-12
DNAse	deoxyribonuclease
Epas1	endothelial PAS domain protein 1
EVs	Extracellular vesicles
F2r	coagulation factor II (thrombin) receptor
FACS	fluorescence-activated cell sorting
FBS	fetal bovine serum
FCCP	carbonyl cyanide-p-trifluoromethoxyphenylhydrazone
Fgf2	fibroblast growth factor 2
FITC	fluorescein isothiocyanate

Abbreviation	Definition
GO analyses	gene ontology analyses
GDC	glycolysis-derived glucose consumption
GTP	guanosine triphosphate
HTN	Hypertension
ICAM1	intercellular adhesion molecule 1
Ifng	interferon gamma
IgG	immunoglobulin G
Il1b	interleukin 1 beta
Il6	interleukin 6
JC-10	lipophilic mitochondrial membrane potential fluorescent dye
LPS	lipopolysaccharide
MCTs	monocarboxylate transporters
MCT4	monocarboxylate transporter 4
miRNAs	microRNAs
MIP-1α	macrophage inflammatory protein-1 alpha
MMPs	matrix metalloproteinases
MRI	magnetic resonance imaging
MSCs	mesenchymal stem cells
NFT	neurofibrillary tangles
Nfkb1	nuclear factor kappa B1
NG2	neural/glial antigen 2; chondroitin sulfate proteoglycan 4
NGF	nerve growth factor
Notch3	neurogenic locus notch homolog protein 3
Nos1	nitric oxide synthase 1
Nos2	nitric oxide synthase 2
Nox4	NADPH oxidase 4
NT-3	neurotrophin-3
NVU	Neurovascular Unit
OCR	oxygen consumption rate
OxPhos	oxidative phosphorylation
PAR1	Protease-Activated Receptor 1
PBS	phosphate-buffered saline
PDGF-BB	platelet-derived growth factor-BB
PDGFRß	platelet-derived growth factor receptor beta
PET	positron emission tomography
Ptgs2	prostaglandin-endoperoxide synthase 2
P2Y12R	purinergic receptor P2Y12
Ren	renin

Abbreviation	Definition
Rgs5	regulator of G-protein signaling 5
RNA	ribonucleic acid
SHR	spontaneously hypertensive rats
SHRSP	spontaneously hypertensive stroke-prone rat
Sod1	superoxide dismutase 1
Stat3	signal transducer and activator of transcription 3
STL	solanum tuberosum lectin
STRING	search tool for the retrieval of interacting genes/proteins
TCA	tricarboxylic acid cycle
TGFβ	transforming growth factor beta
TIMPs	tissue inhibitors of metalloproteinases
TNFa	tumor necrosis factor alpha
UEA-1	Ulex europaeus lectin I
VAMs	vascular associated microglia
VEGF	vascular endothelial growth factor
VEGF-B	vascular endothelial growth factor B
VCAM1	vascular cell adhesion molecule 1
VCI	Vascular cognitive impairment
VNC	vasculo-neuronal coupling
WMH	White matter hyperintensities
ZO-1	zonula occludens-1
ΔΨm	membrane potential

1 Introduction

Chronic arterial hypertension plays a critical role in the development of cerebral small vessel disease, which contributes significantly to accelerated cognitive decline and an increased risk of dementia. In this thesis, I will demonstrate how pericytes and microglia within the neurovascular unit respond to hypertensive stress by utilizing the Spontaneously Hypertensive Stroke-Prone Rat model of cSVD and human post-mortem brain tissue.

1.1 The effects of chronic arterial hypertension on cognitive decline and cerebral small vessel disease

Chronic arterial hypertension, defined as systolic blood pressure (SBP) ≥140 mmHg or diastolic blood pressure (DBP) ≥90 mmHg (1), particularly in midlife, is associated with accelerated cognitive decline and an increased risk of developing all-cause dementia, including neurodegenerative Alzheimer's disease (AD) and vascular cognitive impairment (VCI) (2–5). Arterial hypertension leads to the development of sporadic hypertensive cerebral small vessel disease (cSVD), which is the primary cause of VCI and a significant contributor to extensive intracerebral hemorrhage (6–9). In clinical practice, cSVD is currently diagnosed through the detection of downstream, often irreversible brain pathologies, such as lacunes, increased perivascular spaces, white matter hyperintensities (WMH), microbleeds or hemorrhages, which are secondary manifestations of initial microvascular dysfunction (6,10) (Fig. 1). However, the lack of specific biomarkers and suitable translational imaging measures makes it difficult to detect cSVD at an early stage in the clinical setting.

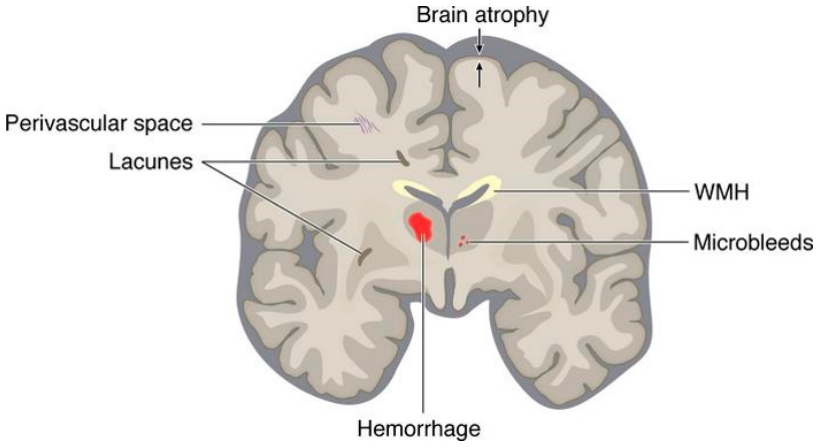

Fig. 1 Neuroimaging hallmark features of cerebral small vessel disease
Key Magnetic Resonance Imaging features associated with cSVD. (Fig. from (11)).

The initial microvascular dysfunction in cSVD is associated with chronic low-grade oxidative microvascular injury (12). This type of injury has been shown to lead to structural and functional changes, including the disruption of the blood-brain barrier (BBB) and neuroinflammation (2,12,13). Studies from autopsy and molecular imaging have provided evidence to support the role of neuroinflammation as a significant contributor to the development of hypertensive cSVD (10,14–16). Arteriolosclerosis, a common cSVD subtype characterized by thickening and stiffening of the vessel walls, is frequently observed in the elderly population and in individuals with vascular risk factors. This condition leads to significant changes in cerebral microcirculation, thereby increasing the susceptibility to ischemic episodes (17). Additionally, given the significant role of neuroinflammation in the pathogenesis of AD, it is possible that neuroinflammation represents a crucial connection between neurovascular and neurodegenerative diseases (18).

Chronic arterial hypertension impairs cerebral microvascular function through several mechanisms including neurovascular uncoupling, decreased vascular reactivity, and reduced cerebral blood flow (2,19–21). Therefore, chronic hypertension poses a threat to healthy aging of the brain but also provides a window for prevention and treatment when detected early. Although considerable progress has been made in the treatment of hypertension and a greater understanding of its effects on cognitive function, only about half of adult hypertensive patients achieve adequate blood pressure control, even though it has been shown that blood pressure reduction can lower mild cognitive impairment and dementia incidence (2,22). This demonstrates a substantial opportunity to prevent cognitive decline through blood pressure management, particularly during midlife. However, in later stages, the preservation of cognitive health through blood pressure reduction alone is restricted owing to the accumulation of irreversible tissue damage and impairment of microvascular function (22). Nevertheless, hypertension is commonly viewed as a disease state rather than a spectrum, with pathomechanisms that vary based on the stage of progression. Current research, incorporating both experimental and imaging-based human studies, indicates that hypertension is associated with various pathological mechanisms, such as endothelial dysfunction, compromised blood-brain barrier integrity, neuroinflammation, vascular wall remodeling, and increased amyloid pathologies (3,12,23).

1.2 The role of the neurovascular unit in hypertension

The intricate pathophysiological mechanisms associated with hypertensive cSVD are multifaceted and involve complex processes such as microvascular dysfunction, BBB disruption, and

neuroinflammation (12,24). The focus has been primarily on studying the clinically symptomatic downstream negative consequences of these mechanisms, including lacunes, WMH, and intracerebral hemorrhages. Nonetheless, it is the subtle early microvascular alterations that ultimately lead to these severe outcomes.

The neurovascular unit (NVU), a vital structural and functional interface formed by brain endothelial cells, pericytes, astrocytes, neurons, and microglia, is the core of these early microvascular alterations (25). Effective communication among these elements contributes to the continuous regulation of arterioles and capillary blood flow (25). This communication also supplies neurons with energy substrates and removes brain waste metabolites. This phenomenon of increased local tissue perfusion in response to neural activity, known as functional hyperemia, is facilitated by a series of mechanisms collectively referred to as neurovascular coupling (NVC) (26). However, the interactions at the NVU are bidirectional, where there is ongoing vessel-to-neuronal signaling, also known as vasculo-neuronal coupling (VNC), which plays a vital role in maintaining brain homeostasis by facilitating essential body-to-brain communication (27). Therefore, the NVU represents a pivotal vulnerability point in the brain. Understanding the response of the NVU to hypertensive stress is relevant, as it can offer a valuable perspective on the initial stressors that trigger the development of cSVD (Fig. 2).

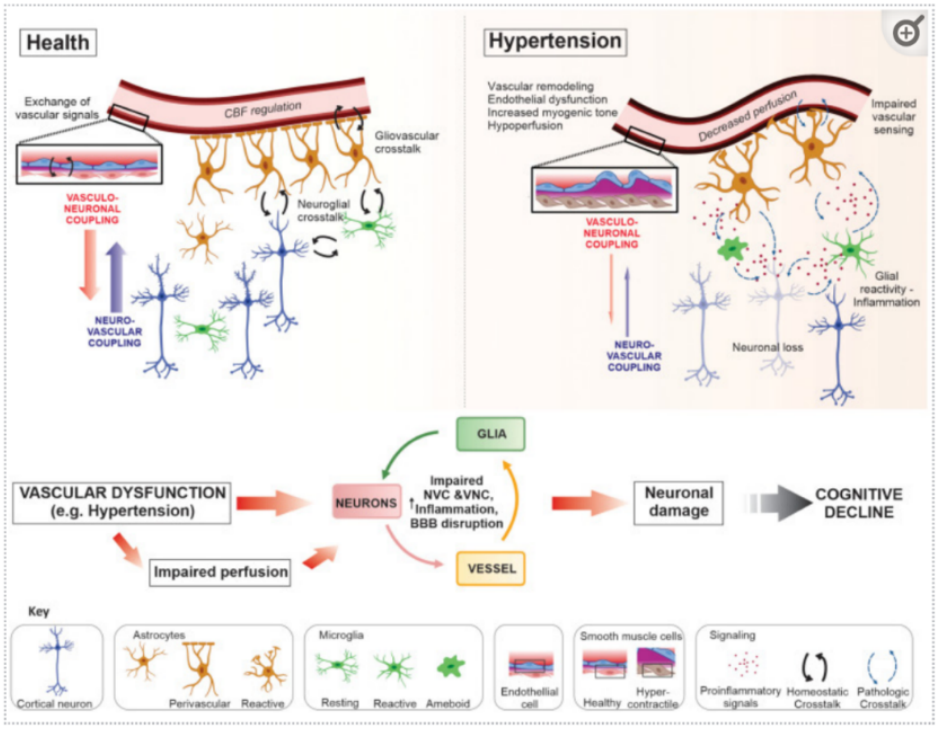

Fig. 2 Neurovascular unit crosstalk in health and hypertension

The healthy brain is characterized by dynamic interactions at the NVU to maintain an optimal environment for neuronal function. Astrocytes and microglia respond to neuronal signals via specific receptors or extracellular vesicles, exerting functions such as neuronal support, synaptic development, phagocytosis, and modulation of neuronal activity. Additionally, the release of vasoactive signals from vascular, glial, and neuronal cells helps regulate cerebral blood flow through neurovascular coupling and vasculo-neuronal coupling, maintain the BBB, provide immune surveillance, and ensure ionic and neurotransmitter homeostasis. Under conditions such as hypertension, the NVU undergoes changes that progressively impair cellular communication, transitioning from a state of homeostasis to one of pathology. Vascular dysfunction, including extracellular matrix remodeling, endothelial and pericyte dysfunction, and vascular and glial inflammation (astrogliosis and microgliosis), contribute to impaired perfusion and loss of BBB integrity. These detrimental processes diminish the stability of the NVU and impair neuronal function, which in turn contribute to neurodegeneration and cognitive decline. (Fig. and fig. legend adapted from(27)).

1.3 Cerebral pericytes

Given the vital function of the NVU in maintaining brain homeostasis, it is clear that the NVU response to hypertensive stress is a critical determinant in the development of cSVD. The cerebral microvasculature, which is essential for brain health, plays a pivotal role in maintaining vascular stability and homeostasis (28–32). Pericytes, one of the key components of the NVU, play a vital role in maintaining the vascular stability and integrity of the BBB (33,34).

Pericytes are contractile cells situated within the walls of microvessels, including precapillary arterioles, capillaries, and postcapillary venules (35). Embedded in the basement membrane, which envelops endothelial cells, pericytes are integral to vascular architecture (36–39). These cells are present across various organs, yet are particularly abundant in the brain, where they are key in the function of the NVU (32,39,40) (Fig. 3a). Brain pericytes are indispensable for regulating angiogenesis, sustaining vascular stability, controlling BBB permeability, clearing toxic metabolites, and modulating neuroinflammatory responses (38,39,41,42) (Fig. 3b).

Pericytes are essential for maintaining cerebral blood flow (CBF) and exert their influence by modulating the diameter of capillaries, which in turn affects the distribution of blood flow within the brain (43,44). The implications of their dysfunction (Fig. 3b) extend to a spectrum of cerebrovascular conditions, ranging from stroke to dementia, demonstrating their significance in various pathological disorders (45–49). Under steady-state conditions, pericytes suppress the expression of molecules such as intercellular adhesion molecule 1 (ICAM-1) to mediate immune cell infiltration, collectively contributing to immunosurveillance and overall cerebrovascular health

(42,50–52). Therefore, pericyte dysfunction can lead to increased immune cell entry into the CNS, contributing to neurodegenerative changes and cognitive impairment (49).

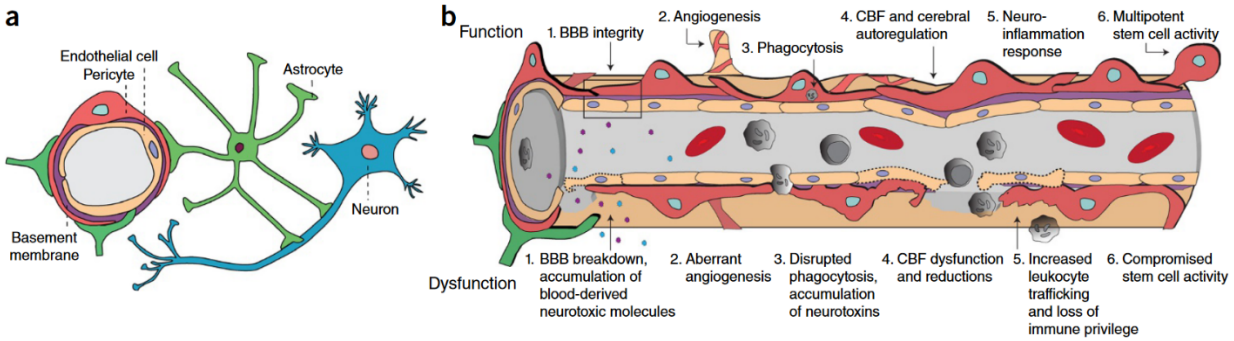

Fig. 3 The multifunctional role of CNS pericytes at the NVU

(a) A simplified diagram of the neurovascular unit (NVU), illustrating the interactive cellular network at the brain capillary level, including vascular cells, glial cells, and neurons. (b) Under physiological conditions (top row), pericytes play crucial roles in: (1) maintaining the integrity of the BBB, including the formation of tight and adherens junctions and transcytosis across the BBB; (2) facilitating angiogenesis, which involves microvascular remodeling, stability, and architecture; (3) performing phagocytosis to eliminate toxic metabolites from the central nervous system (CNS); (4) regulating cerebral blood flow (CBF) and capillary diameter; (5) controlling neuroinflammation through the trafficking of leukocytes into the brain; and (6) supporting the activity of multipotent stem cells. Pericyte dysfunction (bottom row) leads to: (1) the breakdown of the BBB, resulting in the leakage of neurotoxic blood-derived molecules into the brain (e.g., fibrinogen, thrombin, plasminogen, erythrocyte-derived free iron, and anti-brain antibodies); (2) abnormal angiogenesis; (3) impaired phagocytosis, causing the accumulation of neurotoxins in the CNS; (4) CBF dysfunction and ischemic capillary obstruction; (5) increased leukocyte trafficking, promoting neuroinflammation; and (6) reduced stem cell-like ability to differentiate into neuronal and hematopoietic cells. Pericyte dysfunction has been implicated in numerous neurological conditions and contributes to disease pathogenesis. (Figure and Fig. legend from(39)).

Pericyte dysfunction may impair protein clearance, linking vascular and BBB failures to the development of neurodegenerative and neurovascular diseases (21,40). BBB breakdown is a hallmark of disorders such as AD, amyotrophic lateral sclerosis, and cerebral autosomal dominant arteriopathy with subcortical infarcts and leukoencephalopathy (CADASIL) (53–56). These conditions often result in the accumulation of pathological proteins, such as β-amyloid in AD or aggregates of Notch3 in CADASIL, which compromise BBB integrity and precede functional impairments in cerebral vessels (57–59). BBB breakdown is increasingly being recognized as an early event in CSVD development (6). In conditions such as chronic arterial hypertension (12), pericyte dysfunction may be linked to BBB disruption by endothelial cell malfunction and cerebrovascular remodeling, with consequent cSVD onset (60,61).

Pericytes were initially described by Rouget in 1873 and were later named by Zimmermann in 1923 (62). Despite the discovery of pericytes more than a century ago, their complete function has remained elusive, and they continue to be the subject of intensive research. Pericytes are present throughout the body and their density, morphology, and function vary across different locations (63,64). Pericytes are traditionally identified by their proximity to the endothelium; however, recent studies have revealed heterogeneity in their surface markers. Despite their physiological importance, the functional heterogeneity and differentiation process of pericytes are not yet fully understood, in part due to the challenges in differentiating them from other mural cell populations. Recent single-cell RNA sequencing analyses have identified tissue-specific pericyte populations in various organs, including the lung, heart, kidney, and bladder, which express markers, such as Cspg4 (NG2) and platelet-derived growth factor receptor beta (PDGFRβ) (65,66). Although all pericytes express PDGFR-β, the expression of specific markers varies depending on the tissue in which they reside.

Pericytes are commonly identified by the expression of PDGFRβ, neuron/glial antigen 2 (NG2), CD13 (aminopeptidase N), and alpha-smooth muscle actin (αSMA) (66–68). However, none of these markers are consistently co-expressed on all pericytes, and thus, a combination of markers is necessary for accurate identification. Using a mouse model that combined PDGFRβ and NG2 promoters, researchers have achieved specific pericyte targeting, where pericyte ablation demonstrated a rapid neurodegeneration cascade that linked pericyte loss to acute circulatory collapse (69). This leads to an increase in BBB permeability, cerebral edema, and neuronal loss (69). A recent study (70) demonstrated the use of a laminin knockout model specific to pericytes and smooth muscle cells (SMCs) in aged mice. This model revealed a decrease in pericyte density and an increase in immunoglobulin G (IgG) and dextran-fluorescein isothiocyanate (FITC) deposits, which were attributed to the breakdown of the BBB. Additionally, they found a reduction in the tight junction proteins claudin-5 and zonula occludens-1 (ZO-1), which are crucial for maintaining BBB integrity (70).

During angiogenesis, pericytes detach from the endothelium to enhance endothelial cell plasticity during vascular remodeling, facilitating the movement and stabilization of new blood vessels (39,67). In this process, angiopoietin receptor Tie2, vascular endothelial growth factor (VEGF), and matrix metalloproteinases (MMPs) play essential roles in vascular remodeling (71–73). Pericytes also produce essential growth factors such as transforming growth factor beta (TGFβ),

vascular endothelial growth factor A (VEGF-A), and tissue inhibitors of metalloproteinases (TIMPs), which influence further influences BBB integrity, angiogenesis, and remodeling (63,72,73).

Recent studies have revealed unexpected immunomodulatory functions for pericytes. Under basal conditions, pericytes exhibit anti-inflammatory effects that contribute to the active regulation of immune surveillance in the CNS (67,72). They also produce neuroprotective growth factors, such as pleiotrophin, nerve growth factor (NGF), brain-derived neurotrophic factor (BDNF), and Neurotrophin-3 (NT-3), which promote neuron survival (69,74). In addition, pericytes can respond to bacterial components by activating Toll-like receptor 4, leading to inflammation, similar to that of classical immune cells (42). In *vivo* studies have demonstrated that pericytes are the primary producers of chemokines, such as CCL2, after LPS stimulation and mediate early neuroinflammatory responses (75,76).

Elevated levels of tumor necrosis factor-alpha (TNF-α) have consistently been associated with various complications and disease progression in chronic arterial hypertension. Research has demonstrated that patients with hypertension exhibit elevated TNF-α levels, contributing to increased arterial stiffness, decreased arterial compliance, and increased inflammation (77,78). Among the various cell types within the NVU, pericytes are particularly sensitive to TNF-α and display a distinct cytokine and chemokine release profile. Notably, pericytes release high levels of MIP-1α and IL-6, which play critical roles in enhancing microglial activation. Additionally, these cells produce various pro-inflammatory mediators, including IL-1α, IL-6, CCL2, CCL5, and IFNγ (79). These findings suggest that brain pericytes may act as unique sensors and effectors of TNF-α, thereby significantly contributing to the induction of brain inflammation.

1.4 Microglia

Considering the crucial role of pericytes in the NVU, it is important to explore the complex interactions and contributions of microglia within this complex system (Fig. 4). Microglia, resident macrophages of the brain parenchyma, participate in various essential functions of the CNS, including glio-, vasculo-, and neurogenesis, as well as synaptic and myelination processes.

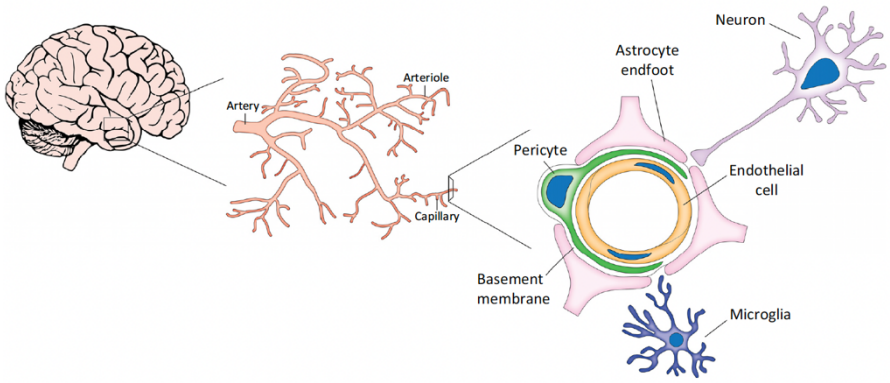

Fig. 4 The multifunctional role of microglia at the NVU

Depiction of the NVU, demonstrating the cellular interactions crucial for maintaining cerebral homeostasis. The left portion of the figure portrays the brain's vascular network, including arteries, arterioles, and capillaries. The right panel enlarges a capillary cross-section within the brain, emphasizing the endothelial cells that form the BBB, pericytes that regulate blood flow and BBB integrity, and astrocytic end-feet that support BBB maintenance. Neurons depend on the NVU for their metabolic requirements. Microglia, which are the resident immune cells of the central nervous system, play a vital role in monitoring the brain environment, responding to injury, and mediating neuroinflammatory responses. Their interactions with other NVU components are crucial for maintaining homeostasis and are essential in pathological conditions. (Figure from(42)).

These functions are facilitated by motility, the release of soluble factors, and phagocytic ability (Fig. 5). Microglia, which serve as the resident immune cells of the CNS, are integral to maintaining homeostasis in response to pathological events by mediating neuroinflammatory processes (80). Microglia are highly dynamic; in constant monitoring, and depending on the brain region, they are sensitive to changes in their microenvironment. Microglia play a central role in neuroinflammation (81–83). Resident microglia are commonly distinguished from infiltrating myeloid cells by markers including CD45, CD11b, Tmem119, and P2Y purinoceptor 12 (P2RY12) (84). Flow cytometric analyses have identified a diverse range of microglial phenotypes with markers such as CD45, CD11b, CD68, CD86, MHC-II, and CD200R, which contribute to the characterization of microglial heterogeneity in neuroinflammatory diseases (85,86). Microglia can be activated in response to low-grade inflammation in the periphery. Their overactivation can lead to increased microvascular permeability, disrupting the BBB, as demonstrated in murine models of autoimmune diseases and systemic inflammation (87,88). The release of pro-inflammatory cytokines and chemokines, which are commonly found in AD and VCI, can also trigger the expression of adhesion molecules in brain endothelial cells. This leads to the infiltration of leukocytes, synaptic pruning, and demyelination (80,89,90).

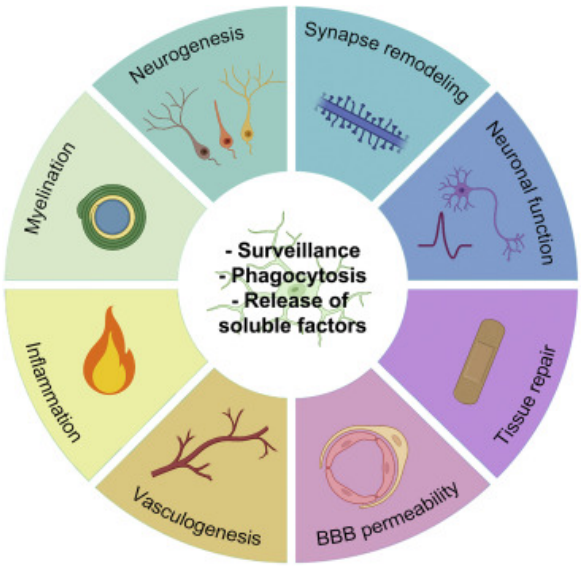

Fig. 5 Multifaceted roles of microglia in the CNS

Diverse functions of microglia within the CNS. Central to their role are surveillance, phagocytosis, and the release of soluble factors. Surrounding their core function, microglia contribute to various processes including synapse remodeling, neuronal function, tissue repair, BBB permeability, vasculogenesis, inflammation, myelination, and neurogenesis. (Figure from (91)).

Hypertensive cSVD exhibits regions of increased microglial reactivity that do not overlap with areas of heightened BBB permeability. This suggests spatial separation between the two processes (16). Microglia play a crucial role in modulating neuronal responses via purinergic mechanisms by interacting with both neurons and blood vessels (92). Altered microglial activity and accompanying inflammatory changes can disrupt cerebral blood flow and impair neurovascular coupling, which has been shown to precede the onset of symptoms in several neurodegenerative disorders (16,82). Emerging data suggest that the microglial response to capillary lesions is dependent on the P2Y12 purinergic receptor (P2Y12R) for BBB repair, as demonstrated in studies where suppression of these receptors diminished microglial motility (93,94). Moreover, P2Y12R accumulation at endothelial cell contacts is essential for vasodilation, and a localized deficiency of P2Y12R has been associated with synaptic degeneration, demonstrating a relationship between vascular inflammation and synaptic/neural dysfunction (92). However, the precise mechanisms by which microglia interact with the vasculature and react during peripheral low-grade chronic inflammation in hypertensive cSVD are yet to be described.

The precise spatial, temporal, and causal associations between microglial reactivity, BBB leakage, and peripheral low-grade inflammation in hypertensive cSVD remain unclear. Although microglial positron emission tomography studies have found a correlation between BBB disruption and increased neuroinflammation in AD and cSVD (16), the causal relationship between these events is not fully understood. Research on microglial dynamics in hypertensive cSVD must address whether low-grade peripheral inflammation triggers central neuroinflammation, or vice versa, or whether both are mutually reinforcing. Additionally, recent evidence suggests that microglia

exhibit dynamic changes in diversity throughout life, with high heterogeneity during early development, a more homogenous population in adulthood, and re-emergence of heterogeneity during senescence and under pathological conditions (91,95,96). For example, microglial diversity was observed in an animal model of AD in which microglial clusters with distinct gene expression profiles were identified in cortical regions (97,98).

Upon exposure to various stimuli, microglia can become activated and transform into disease-associated microglia (DAM) in response to systemic inflammation or neurodegeneration (96). However, to date, there are insufficient data describing distinct microglial profiles that can be used to better understand microglia function in hypertensive states and manipulate specific subpopulations in the hypertensive brain. To date, no studies have evaluated regional differences in microglial activation in lifelong hypertensive patients who develop cSVD. Given their capacity to react rapidly to alterations in the brain microenvironment, microglia may play a critical role in the development and progression of hypertensive cSVD.

1.5 Role of extracellular vesicles in intercellular communication and disease

Extracellular vesicles (EVs) have recently gained considerable interest for their role in intercellular communication as they influence cell behavior by transferring bioactive molecules (99,100). EVs are lipid bilayer membrane-delimited nano- to micro-sized particles that are released into the surrounding field upon the fusion of multivesicular bodies and the plasma membrane (101). Based on the most recent guidelines, EVs can be classified according to their size into small EVs (< 200 nm in diameter) and large EVs (> 200 nm in diameter). These vesicles, which are released by all cell types into the circulation, facilitate unique cellular interactions by carrying cargo of proteins, lipids, and nucleic acids, capable of modulating the function of recipient cells and thus contributing to disease processes (102). EVs have been recognized as potential candidates for biomarkers and therapeutic applications owing to research conducted over the past decade, which has revealed that they contain misfolded proteins associated with Alzheimer's, Parkinson's, and prion diseases (103–105). Additionally, altered genetic cargo, often in the form of miRNAs, has been identified in EVs from patients with these diseases, suggesting that EVs may serve as sources of disease biomarkers (106). Furthermore, studies have demonstrated that microglia release tau via exosome secretion, and inhibiting exosome synthesis has been shown to significantly reduce tau propagation in both *in vitro* and *in vivo* settings (107). Inflammation-related miRNAs carried by EVs from endothelial cells mediate inflammatory responses in pericytes, leading to the production of VEGF (108). *In*

vivo, pericyte-derived EVs have been shown to reduce blood-spinal cord barrier damage and apoptosis in a mouse model of spinal cord injury, highlighting their potent therapeutic effects (109). The production and function of pericyte-derived EVs are influenced by various stimuli; for example, platelet-derived growth factor-B chain (PDGF-BB) stimulation leads to EVs enriched with growth factors, such as BDNF and VEGF, whereas LPS stimulation results in EVs containing pro-inflammatory cytokines, such as IL-6 and CCL2 (72). Notably, EVs from mesenchymal stem cells (MSCs) have demonstrated therapeutic potential by promoting recovery in animal models, where adipose tissue mesenchymal stem cell-derived extracellular vesicles can attenuate myocardial impairments and reduce inflammation in renovascular hypertension through anti-inflammatory properties (110).

1.6 Metabolic dysregulation in hypertension

EVs also play a role in regulating metabolism, affecting cellular pathways such as glycolysis and oxidative phosphorylation (OxPhos) (100). Metabolism is defined as the sum of all chemical reactions within cells, and is vital for providing the energy required to sustain life (111). Efficient production of ATP is ensured through metabolic pathways such as glycolysis, the Krebs cycle, and OxPhos (112). Glycolysis involves intracellular breakdown of glucose, resulting in the production of pyruvate and ATP. Acetyl coenzyme A (acetyl-CoA), which is formed during glycolysis from the oxidized derivative of pyruvate, initiates the subsequent stage of glucose metabolism, known as the Krebs or citric acid cycle. This stage generates guanosine triphosphate (GTP) and other essential derivatives, following which OxPhos represents the final stage of cellular respiration (112).

In the brain, metabolic dysregulation is a hallmark of cSVD, with studies showing elevated glycolysis in the non-lesional white matter of individuals with cSVD compared to healthy controls, which suggests that increased glycolysis is a marker of underlying pathology (113). White matter lesions associated with cSVD are associated with an increased risk of ischemic injury, stroke, and cognitive decline. However, little is known about the metabolic changes that occur in non-lesional tissues. Aerobic glycolysis (AG) is crucial for maintaining myelin homeostasis and repair in the white matter (113). Studies using multi-tracer positron emission tomography (PET) have shown increased glycolysis in non-lesional white matter in cSVD, suggesting an adaptive response to ongoing vascular and metabolic stress (114). This phenomenon is consistent with findings demonstrating that the brain AG plays a significant role in synaptic plasticity and learning (115).

The human brain experiences significant metabolic changes with age, including a reduction in brain volume, cortical thickness, and synaptic density, which is accompanied by decreased glucose metabolism and oxygen consumption (116,117). These changes, which are shaped by evolutionary trade-offs and environmental factors, are evident in the metabolic processes of the aging brain. Aerobic glycolysis, also known as the non-oxidative metabolism of glucose in the presence of oxygen, accounts for approximately 10 % to 12 % of the glucose utilized by the adult human brain, and is a critical element of brain metabolism, particularly in maintaining synaptic plasticity (117,118). This process is essential for energy production, such as at excitatory synapses, and supports neuroprotective pathways (118). As the brain ages, a decline in aerobic glycolysis during the resting state reflects a decrease in synaptic plasticity and completion of developmental processes such as myelination (114). Furthermore, aerobic glycolysis plays a role in resilience and/or response to the early stages of amyloid pathology, and it may be impaired because of age-related white matter disease (119).

Recent advancements in PET imaging have enabled the examination of changes in glycolysis in the white and gray matter associated with cSVD. A study has demonstrated that in cSVD, there is a relative increase in glycolysis in the adjacent WM, despite a general reduction in metabolism within the WMH itself (113). This elevated glycolysis near lesion boundaries further supports an adaptive response that may be driven by hypoxia-inducible factors or inflammatory processes involving activated microglia (115,117). Therefore, this phenomenon may indicate an adaptive increase in glycolysis, which is vital for maintaining myelin homeostasis and serves as a protective or compensatory mechanism to support axonal repair in the face of chronic metabolic stress (113,117).

1.7 The Spontaneously Hypertensive Stroke-Prone Rat animal model

The Spontaneously Hypertensive Stroke-Prone (SHRSP) rat model is a well-established model for studying cSVD, vascular dementia, and lacunar infarcts (120,121). This model was initially developed in 1963 by Okamoto and Aoki through selective inbreeding of spontaneously hypertensive Wistar rats, which exhibited a 100 % prevalence of arterial hypertension by the third generation (122), called spontaneously hypertensive rats (SHR). In 1974, the SHRSP developed from an SHR that displayed significantly higher blood pressure, reduced CBF, and increased spontaneous cerebrovascular lesions (123,124). Adult SHRSP rats exhibit systolic blood pressure ranging from 220 to 240 mmHg, as opposed to 180 to 200 mmHg in SHRs, and approximately 80

% of SHRSPs experience a stroke during their lifetime, in contrast to less than 10 % incidence in SHRs (125).

The cerebral cortex and basal ganglia are the primary locations where spontaneous infarcts occur, accompanied by significant reductions in CBF at lesion sites (126–128). It is important to note that the arterial hypertension observed in SHRSP is multifactorial and cannot be attributed to a single cause. Several key factors contribute to the development of hypertension, including alterations in the renin-angiotensin system, which is characterized by elevated plasma renin and angiotensin II levels, increased angiotensin-converting enzyme levels, and higher expression of angiotensin receptors 1a and 1b in the adrenal cortex (129–131). Additionally, in SHRSP at malignant hypertensive stages, there is a notable increase in cerebral endothelin-1 levels, which plays a role in decreasing cerebral blood flow and increasing the risk of stroke (132). Finally, it has been established that nitric oxide synthase dysfunction in the middle cerebral arteries of SHRSP precedes the occurrence of stroke, with consequences for myogenic function and cerebral blood flow regulation (133).

Cerebral microangiopathy in SHRSP is characterized by BBB disruption, endothelial damage, accumulation of plasma proteins such as fibrin and immunoglobulin G (IgG) in small cerebral vessel walls, and degenerative vessel wall thickening that yield arteriolosclerosis and hyalinosis (134,135). These changes become evident in histological examinations starting from 18 weeks of age. Additionally, extended perivascular spaces are detectable, particularly near the regions of BBB damage (136,137). At 28 weeks of age, increased vascular occlusions in arterioles and small arteries can lead to spontaneous infarcts in 10-20 % of animals (134).

Although the SHRSP model was created long before the advent of modern genetic models, it remains invaluable for researching the genetic basis of essential hypertension in humans, which involves complex interactions between many genes that are still not fully understood (125). In vivo imaging suggests a pathophysiological cascade in SHRSP that begins with vascular wall and blood-BBB damage (Fig. 6) (134,138). Initially, endothelial leaks facilitate the accumulation of plasma protein deposits under the endothelium (Fig. 6A). Subsequently, these deposits trigger the formation of nonobstructive thrombi, where trapped erythrocytes appear as stasis on histological staining (Fig. 6B). As the damage progresses, vessel walls rupture, resulting in microbleeds (Fig. 6C). Ultimately, this cascade leads to the formation of necrotic spongy tissue with secondary thrombi (Fig. 6D). A high-salt diet significantly increases the prevalence of bleeding, with 70-100

% of animals experiencing bleeding by 16-18 weeks of age (139). However, when fed a normal diet, the SHRSP perfectly mimics the vulnerable hypertensive patient population in its initial and preclinical disease stages by combining arterial hypertension development and polygenetic susceptibility to cSVD (140). Interestingly, pathological accumulation of amyloid has been detected in the walls of damaged vessels in SHRSP, despite it being a model of non-amyloid cSVD with no known genetic alterations in amyloid metabolism (141,142). This suggests that amyloid accumulation in SHRSP is a consequence of cSVD pathology, triggered by hypoxia and BBB disruption (143). Given the clear delineation of vascular pathology in this model, it provides an established framework for studying the complex interactions among NVU cells, with a specific focus on pericytes and microglia.

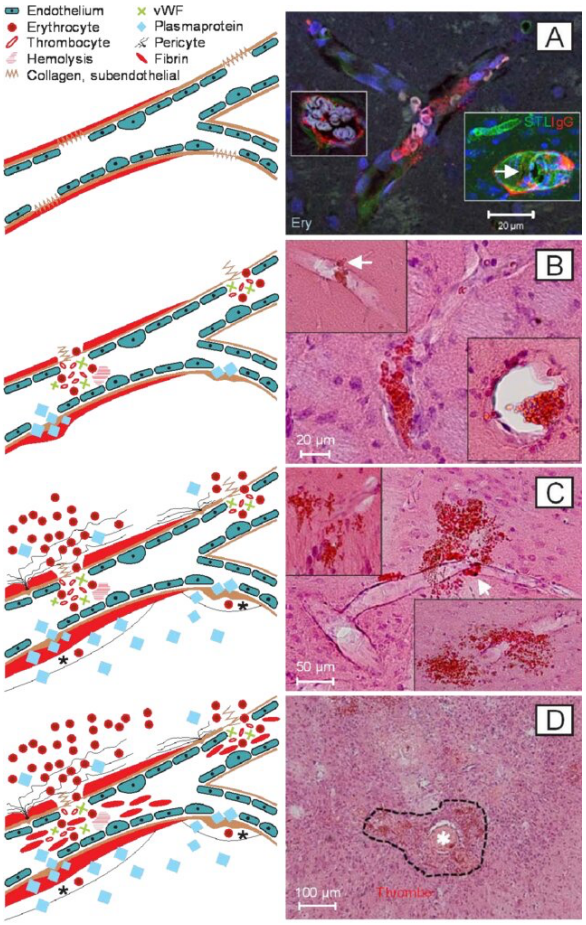

Fig. 6 Pathological progression of cSVD in the SHRSP model

(A-D) illustrate the progression of vascular damage in SHRSP (Spontaneously Hypertensive Stroke-Prone) rats. The sequential stages depicted in the diagrams commence with endothelial leaks progressing with plasma protein deposits, non-obstructive thrombi, and culminate in vessel wall ruptures and microbleeds. (A)The histological images display subendothelial plasma protein deposits, (B) stases and early erythrocyte diapedesis, (C) ruptured vessels accompanied by microbleeds, and (D) necrotic spongy tissue with secondary thrombi (D). (Figure from(138).

1.8 Hypotheses and aims of this dissertation

Cerebral small vessel disease is a major cause of stroke and dementia, however the cellular and molecular mechanisms that drive this pathology are not fully understood. Within the neurovascular unit, pericytes and microglia are critical players, whose dysfunction under chronic hypertension may lead to profound consequences. Pericytes, which regulate BBB integrity, cerebral blood flow, and neuroinflammatory responses, may be particularly susceptible to hypertension. Their dysfunction may lead to BBB breakdown, compromised vascular stability, and subsequent neuroinflammation, potentially exacerbating the pathology of cSVD. Despite their essential role within the NVU, the mechanisms by which pericytes contribute to disease progression, as well as the specific phenotypic and metabolic profiles they undergo in hypertensive cSVD, have not been well characterized.

Microglia, the resident immune cells of the brain, also play a vital role in maintaining NVU integrity. However, the extent to which microglia interact with the vasculature and respond to peripheral low-grade chronic inflammation in hypertensive cSVD is not yet fully understood. The spatial, temporal, and causal associations between microglial reactivity, BBB leakage, and peripheral inflammation in hypertensive cSVD are still unclear. Moreover, recent research has suggested dynamic changes in microglial diversity and activation states, particularly under pathological conditions. Therefore, it is vital to determine whether low-grade peripheral inflammation triggers central neuroinflammation, or vice versa, or whether these processes are mutually reinforcing.

1.8.1 Hypotheses

I. Do chronic hypertensive states induce phenotypic and metabolic changes in pericytes, thereby exacerbating cSVD pathology?

II. Do chronic hypertensive states trigger a distinct activation profile in microglia that promotes the progression of cSVD?

1.8.2 Aims

I. To characterize the phenotypic alterations in pericytes across hypertensive states.

II. To investigate the metabolic reprogramming of pericytes in response to chronic hypertension and its implications for BBB integrity.

III. To define the specific activation states of microglia across hypertensive states.

IV. To study the effects of microglial reactivity on BBB integrity and neuroinflammation development.

2 Methods

2.1 Animal model

All experiments were conducted in strict accordance with the German Animal Welfare Ordinance and approved by the Animal Care Committee of Saxony-Anhalt with licenses identified as 42502-2-1561 Uni MD and 42502-2-1277 Uni MD. This thesis utilized the spontaneously hypertensive stroke-prone rat model (Charles River Laboratories, Wilmington, Massachusetts, USA), which models arterial chronic hypertension at specified ages that reflect the progression from initial disease onset to late chronic arterial hypertension (144,145). Wistar rats were used as age-matched controls (Charles River Laboratories, Research Models and Services, Germany GmbH, Sulzfeld, Germany). A total of 116 male rats were used across various experimental phases to investigate pericyte dysfunction and metabolic adaptation in cSVD (Table 1). For the investigation of microglial activation across cSVD phases a total of 64 rats were used, as detailed in Table 2. SHRSP rats develop a vascular risk profile characterized by arterial hypertension between 6-8 weeks of age (134,142,143,146). For the initial hypertension (HTN) phase, we refer to 6-8 weeks old Wistar as Ctrl and SHRSP rats as HTN. The early chronic hypertension phase includes 25-weeks old rats, and the late chronic hypertension phase comprises 34-36 week-old rats. All animals were housed under a natural light-night cycle, had access to water and food *ad libitum*, and were monitored daily to assess neurological function.

Table 1 Distribution of rodents used for the investigation of pericyte dysfunction and metabolic reprogramming in initial and chronic arterial hypertension

Experimental Phase	Purpose	Wistar Rats	SHRSP Rats	Total per Method
Initial Hypertension	FACS Analysis	6 (2x)	6 (2x)	24
Early Chronic Hypertension	FACS Analysis	6 (2x)	6 (2x)	24
Late Chronic Hypertension	FACS Analysis	5 (2x)	5 (2x)	20
Initial Hypertension	In Vitro Culture	9	9	18
Early Chronic Hypertension	PCR Array & In Vitro Culture	10	10	20
Late Chronic Hypertension	PCR Array	5	5	10
Total		58	58	116

Experimental overview and systematic distribution of Wistar and SHRSP rodents used across the various experimental phases and methodologies of the study. FACS: flow cytometric analysis.

Table 2 Distribution of rodents used for the investigation of microglial reactivity across in chronic arterial hypertension

Experimental Phase	Purpose	Wistar Rats	SHRSP Rats	Total per Method
Early Chronic Hypertension	FACS Analysis / MVs	5 (2x)	5 (2x)	20
Late Chronic Hypertension	FACS Analysis / MVs	6 (2x)	6 (2x)	24
Early Chronic Hypertension	Immunofluorescence	5	5	10
Late Chronic Hypertension	Immunofluorescence	5	5	10
Total		32	32	64

Experimental overview and systematic distribution of Wistar and SHRSP rodents used across the various experimental phases and methodologies of the study. FACS: flow cytometric analysis; MVs: microvessels isolation.

2.2 Vascular cell isolation for flow cytometric analysis

To characterize pericytes and endothelial cells, vascular cells were isolated from 6-, 25-, and 34-week-old Ctrl and HTN rats using a modified version of Crouch et al. (147) adapted for rat brains. Following anesthesia with pentobarbital, cerebral cortices were isolated with a scalpel and stored in 2 % FBS in PBS until ready for mincing. Minced tissue pieces were centrifuged at 300 × g at 4 °C for 5 min, the supernatant was discarded, and the pellet was resuspended in collagenase/dispase solution. Incubation was performed at 37 °C with constant rotation for 30 minutes. After incubation, the tissue was centrifuged at 300 × g for 5 min, the supernatant was drained, and the DNAse I solution was added. The homogenate was pipetted thoroughly approximately one fifty times with a 1000 µL pipette to fully disaggregate. The cell suspension was then transferred to a 22 % Percoll gradient (Cat. no. GE17-0891-01; Sigma-Aldrich) in PBS to remove myelin and other impurities. The isolated cells were washed, counted, centrifuged, resuspended, and stained (Fig. 7). Unstained cells, Fluorescence Minus One (FMO), and single-staining controls with compensation beads were used as controls. Prior to fluorochrome-conjugated antibody labeling, the cells were incubated with purified mouse anti-rat CD32 FcγII (clone D34-485, Rat BD Fc Block) for non-specific binding. Cell viability was assessed using a dead dye (Zombie NIR™, Biolegend), and cells were stained with a panel of fluorophore-conjugated antibodies, including anti-CD45 (clone: OX-1), anti-CD31 (clone: TLD-3A12), anti-Pdgfrß (clone: rabbit polyclonal), anti-NG2 (clone: D120.43), and anti-CD13 (clone: WM15), followed by fixation, permeabilization, and anti-Ki-67

(clone: SolA15) staining. Data were acquired and analyzed using AttuneNxT (Thermo Fisher Scientific) and FlowJo Analysis Software v10.5.3 (BD). Uniform Manifold Approximation and Projection (UMAP) analysis was performed on exported live, single, CD45-negative, CD31, and PDGFRß-positive cells downsampled to 7,500 cells per group and time point. Concatenated data were projected to UMAP using vascular compensated markers and 25 nearest neighbors with a minimum distance of 0.8 as running parameters.

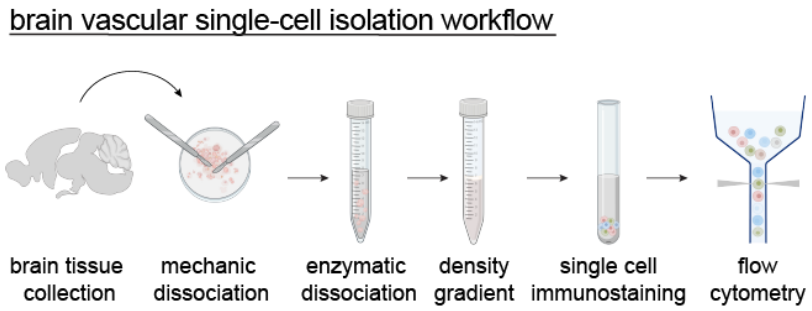

Fig. 7 Workflow for isolation and characterization of vascular cells

Summary of single-cell isolation workflow for subsequent flow cytometric analysis. Created with Biorender.com.

2.3 Tissue dissociation and microvessels isolation

Brains from control (Ctrl) and hypertensive (HTN) rats aged 8, 25, and 34 weeks were harvested following transcardial perfusion with PBS-EDTA. For microvessels isolation, cerebral cortices were cleaned of meninges, cerebellum, and brain stem, then mechanically reduced into small pieces of ~1 × 1 mm in size, as previously described (86,148,149). The tissue was enzymatically digested with Collagenase Type II (1 mg/ml) and DNase I (15 µg/ml) in DMEM/F12 supplemented with penicillin (100 units/ml), streptomycin (100 µg/ml), and glutamine (2mM). Before placing the tissue in the incubator, the homogenate was further mechanically dissociated with a 5 ml pipette (up/down strokes) and digested on a shaker at 37 °C for 50 minutes. To remove myelin and neurons, the homogenate underwent centrifugation in 20 % BSA-DMEM/F12 at 1000 g for 20 min, repeating the process three times, with careful removal of the myelin layer and BSA supernatant after each cycle. The microvessels obtained were collected from each centrifugation pellets (3x) into new sterile tubes and further digested with collagenase-dispase (1 mg/ml) and DNase I (6.7 µg/ml) in DMEM for 60 min at 37 °C. Microvessels were layered on top of a continuous isotonic 33 % Percoll gradient (Cat. no. GE17-0891-01, Sigma-Aldrich) and centrifuged for 10 min at 1000 g at 4 °C with slow deceleration. The isolated microvessels were washed twice, filtered through a

40 µm cell strainer, cell strainer was reversed, washed into a new sterile tube, and centrifuged at 400 g for 10 min at 4 °C. The purity and structural integrity of the microvessels were assessed microscopically before being stored in RNAlater (AM7020, Thermo Fisher Scientific) for further processing, or seeded for *in vitro* culture assays for pericyte *in vitro* expansion.

2.4 RNA isolation, RT^2 profiler PCR array, and RT-qPCR

Collected microvessels were pelleted at 20,000 g for 10 min and resuspended in 350 µl of RLT Plus Buffer from the RNeasy® Micro Kit (QIAGEN). Total RNA was isolated following the manufacturer's instructions, as previously described (86), with RNA quality and concentration determined using a NanoDrop 2000 spectrophotometer (Thermo Fisher Scientific).

2.4.1 RT^2 profiler PCR array

Isolated RNA was used in combination with Power SYBR® Green RNA-to-CT™ 1-Step Kit (Cat. no. 4389986, Thermo Fisher Scientific) on a custom RT^2 profiler PCR Array (QIAGEN) using a LightCycler® 96 (Roche). Reverse transcription was carried out for 30 minutes at 48 °C, followed by enzyme inactivation at 95 °C for 10 min. PCR amplification then proceeded for 55 cycles, each consisting of a denaturation step for 15 seconds at 95 °C, followed by annealing and elongation for 60 seconds at 60 °C. Cycle Threshold (C_T) values were exported to an Excel file to create a table. This table was then uploaded to the data analysis web portal at http://www.qiagen.com/geneglobe. Samples were assigned to control and test groups. C_T values were normalized based on the selection of reference genes. The data analysis web portal calculated fold change and gene regulation using the $2^{-\Delta\Delta Ct}$ method (150). *Hprt* gene was used to normalize the results. Data were further normalized to the respective mean level in age-matched early Ctrl. The full list of genes included in the custom PCR array is provided in Table 3. Downstream GO analyses, data presentation, and statistical analyses of exported gene regulation tables were performed using STRING database version 12.0 and GraphPad Prism 10.

Table 3 Full gene list of the custom RT2 profiler PCR array analysis

Unigene	Refseq	Symbol	Description	RT2 Catalog
Rn.2275	NM_012675	Tnf	Tumor necrosis factor (TNF superfamily, member 2)	PPR06411F
Rn.4772	NM_031530	Ccl2	Chemokine (C-C motif) ligand 2	PPR06714B
Rn.9869	NM_031512	Il1b	Interleukin 1 beta	PPR06480B
Rn.9873	NM_012589	Il6	Interleukin 6	PPR06483B

Rn.9868	NM_012854	Il10	Interleukin 10	PPR06479A
Rn.10795	NM_138880	Ifng	Interferon gamma	PPR45050C
Rn.12	NM_012967	Icam1	Intercellular adhesion molecule 1	PPR42235A
Rn.11267	NM_012889	Vcam1	Vascular cell adhesion molecule 1	PPR45334A
Rn.2609	NM_012950	F2r	Coagulation factor II (thrombin) receptor	PPR42797C
Rn.10762	NM_030851	Bdkrb1	Bradykinin receptor B1	PPR45035A
Rn.198550	NM_053549	Vegfb	Vascular endothelial growth factor B	PPR51827B
Rn.10209	NM_031055	Mmp9	Matrix metallopeptidase 9	PPR44728C
Rn.119634	NM_012886	Timp3	TIMP metallopeptidase inhibitor 3	PPR06533A
Rn.161953	NM_053546	Angpt1	Angiopoietin 1	PPR57511C
Rn.9159	NM_001105737	Tek	TEK tyrosine kinase, endothelial	PPR44285B
Rn.31808	NM_019305	Fgf2	Fibroblast growth factor 2	PPR06641B
Rn.11266	NM_012513	Bdnf	Brain-derived neurotrophic factor	PPR45333A
Rn.14744	NM_053524	Nox4	NADPH oxidase 4	PPR45975A
Rn.17420	NM_031701	Cldn5	Claudin 5	PPR46476A
Rn.195319	NM_031004	Acta2	Smooth muscle alpha-actin	PPR59337B
Rn.98311	NM_031525	Pdgfrb	Platelet derived growth factor receptor, beta polypeptide	PPR06697F
Rn.1150	NM_019341	Rgs5	Regulator of G-protein signaling 5	PPR42418A
Rn.11132	NM_031012	Anpep	Alanyl (membrane) aminopeptidase	PPR45251B
Rn.9831	NM_012642	Ren	Renin	PPR44510A
Rn.9814	NM_030985	Agtr1a	Angiotensin II receptor, type 1a	PPR44498A
Rn.10852	NM_024359	Hif1a	Hypoxia-inducible factor 1, alpha subunit (basic helix-loop-helix transcription factor)	PPR45087B
Rn.55138	NM_023090	Epas1	Endothelial PAS domain protein 1	PPR50863A
Rn.8019	NM_031116	Ccl5	Chemokine (C-C motif) ligand 5	PPR06854F
Rn.10573	NM_052799	Nos1	Nitric oxide synthase 1, neuronal	PPR44930E
Rn.10400	NM_012611	Nos2	Nitric oxide synthase 2, inducible	PPR44835A
Rn.44369	NM_017232	Ptgs2	Prostaglandin-endoperoxide synthase 2	PPR49747F
Rn.22168	NM_001277055	Ngf	Nerve growth factor (beta polypeptide)	PPR47274A
Rn.228683	NM_020087	Notch3	Notch homolog 3 (Drosophila)	PPR50707A
Rn.25733	NM_017022	Itgb1	Integrin, beta 1	PPR48046F
Rn.10247	NM_012747	Stat3	Signal transducer and activator of transcription 3	PPR44745C
Rn.34914	NM_053842	Mapk1	Mitogen activated protein kinase 1	PPR48780A
Rn.4090	NM_053829	Mapk8	Mitogen-activated protein kinase 8	PPR43333A
Rn.6059	NM_017050	Sod1	Superoxide dismutase 1, soluble	PPR43506A

Rn.2411	NM_001276711	Nfkb1	Nuclear factor of kappa light polypeptide gene enhancer in B-cells 1	PPR42746A
Rn.11365	NM_017001	Epo	Erythropoietin	PPR06628C
Rn.10562	NM_012922	Casp3	Caspase 3	PPR06384B
Rn.47	NM_012583	Hprt1	Hypoxanthine phosphoribosyltransferase 1	PPR42247F
N/A	U26919	GDC	Rat Genomic DNA Contamination	PPR63338A
N/A	SA_00104	RTC	Reverse Transcription Control	PPX63340

List of genes assessed in the custom array profiler (Cat.no. 330171 Custom Array) serving as a resource for our analysis of vascular remodeling in chronic hypertension. The table lists the Unigene identifiers, Refseq numbers, Symbol of each gene, detailed name description, and the RT^2 catalog numbers specific for each gene.

2.4.2 RT-qPCR

Gene expression levels of tight junction proteins and adhesion molecules were assessed in triplicates using 10 ng isolated RNA. Relative gene expression was determined using the TaqMan® RNA-to-CT™ 1-Step Kit (Thermo Fisher Scientific). Reactions were developed in a LightCycler® 96 (Roche). Reverse transcription was performed for 30 min at 48 ºC, followed by inactivation for 10 min at 95 ºC. Subsequently, a two-step amplification was run for 55 cycles, comprising of denaturation for 15 s at 95 ºC and annealing/elongation for 1 min at 60 ºC. Gene expression was quantified using the comparative 2^-ΔΔCt method, normalized against reference gene *Gapdh.* Results were further normalized to control values and expressed as fold changes. The full list of TaqMan® Gene Expression Assays used for mRNA amplification are listed in Table 4.

Table 4 TaqMan assays used for RT-qPCR analyses

Gene Symbol	Gene Name	Assay ID
Cldn5	claudin 5	Rn01753146_s1
Gapdh	glyceraldehyde-3-phosphate dehydrogenase	Rn01775763_g1
Icam1	intercellular adhesion molecule 1	Rn00564227_m1
Ocln	occludin	Rn00580064_m1
Tjp1	tight junction protein 1	Rn07315717_m1
Vcam1	vascular cell adhesion molecule 1	Rn00563627_m1

List of genes analyzed in isolated microvessels including their symbol, full gene name, and corresponding TaqMan® assay ID. Genes were selected given their involvement in various cellular functions such as tight junction and barrier integrity, cellular adhesion, metabolic processes, and growth factor signaling.

2.5 Pericyte *in vitro* subcultures

Rat cerebral pericytes were cultured from isolated brain microvessels containing a mix of pericytes and endothelial cells, as previously described (148). Initial microvessel seeding was established in DMEM/F12 supplemented with 15 % platelet-derived serum, 1 ng/ml bFGF, and 100 µg/ml heparin for the first 2 days. The medium was then switched to DMEM supplemented with 10 % FBS, 1 % non-essential amino acids, and 1 % penicillin/streptomycin to support pericyte survival and proliferation. To enrich pericyte populations and eliminate endothelial cells, cultures were treated in the absence of puromycin allowing pericyte expansion. Subsequent cell expansions were done using Accutase® Cell Solution (Biolegend) for gentle detachment, ensuring optimal cell viability. For cryopreservation, cultures were frozen in CryoStor® CS10 (Stemcell Technologies) and stored in liquid nitrogen.

2.6 Immunofluorescence staining of *in vitro* pericytes

Pericytes were expanded *in vitro* from seeded 8-week-old rat microvessels. At passages 11-13 pericytes at 90-95 % confluence from T-75 cell culture flasks (Greiner CELLSTAR), were seeded at a density of 20,000 cells/well in 12-well plates containing 20 mm coverslips. Coverslips were sterilized and coated with rat tail collagen 24 h prior to pericyte expansion. Cells were fixed with 4 % PFA and washed 48 h after seeding. Thereafter, cells were blocked with 3 % horse serum for 2 h. Primary antibodies were incubated overnight at room temperature in the same solution. After PBS washes, cells were incubated with secondary antibodies diluted 1:1000 in 0.1 % Triton X-100. Mounting was performed with ProLong mounting medium containing DAPI (Cat. no. P36935, Thermo Fisher Scientific), and coverslips were dried in darkness before microscopy analysis. Imaging was performed to visualize and confirm pericyte identity and purity using a TCS SP8 X Laser Confocal Microscope (Leica Microsystems) software (LAS-AF 1.8.1.13759). Full list of antibodies and their specificities can be found in Table 5.

Table 5 Antibody specifications for vascular cells immunofluorescence analysis

Vascular cell immunofluorescence					
Target	**Clone**	**Host**	**Dilution**	**Manufacturer**	**Catalog number**
CD31	390	Rat	1:500	Invitrogen	14-0311-85
NG2	D120.43	Mouse	1:500	Invitrogen	37-2700
PDGFRβ	R.140.4	Rabbit	1:500	Invitrogen	MA5-14851
CD13	WM15	Mouse	1:1000	BioLegend	1972330
Anti-Mouse	polyclonal	Goat/IgG	1:1000	Invitrogen	A-11001
Anti-Rat	polyclonal	Goat/IgG	1:1000	Invitrogen	A-11006
Anti-Rabbit	polyclonal	Goat/IgG	1:1000	Invitrogen	A32733

Selection of primary and secondary antibodies employed for the immunofluorescence staining of vascular cells, detailing the target antigen, clone, host species, dilution ratios, and manufacturer details.

2.7 Immunofluorescence image processing and analysis

Immunofluorescence images were processed using ImageJ (https://imagej.nih.gov/ij/, 1997-2018)), and viewed as hyperstacks in default color mode. The scale was changed from grayscale to specific colors for each channel. Channels were split, with contrast and brightness adjusted uniformly across samples to maintain consistent parameters. Individual adjusted and composite images created were saved as TIFF files. For z-stack images, after color adjustment and maximum intensity projection, images were processed similarly by splitting and merging channels, as described above, with the final composite image converted to RGB and saved as TIFF. The Mean Fluorescence Intensity (MFI) of PDGFRβ, NG2, and CD13 from individual cells was exported from processed images, as described previously (151). Quantitative data were used to plot the MFI for each marker, allowing for the analysis of expression patterns in control versus hypertensive pericytes.

2.8 Flow cytometric analysis of *in vitro* pericytes

At passages 11-13 pericytes at 90-95 % confluence from T-75 cell culture flasks were dissociated with Accutase® Cell Solution (BioLegend) and prepared for flow cytometry to analyze subtype distribution *in vitro*, comparing control vs. hypertensive-derived cells. Cells were stained with antibodies against PDGFRβ, NG2, and CD13 and analyzed using an Attune NxT Flow Cytometer. FMO controls and unstained samples were used to set gates. Post-acquisition data analysis was performed using FlowJo software (v10.5.3). Data were biexponentially transformed for scaling and t-distributed Stochastic Neighbor Embedding (tSNE) was employed on compensated PDGFRβ-

positive cells at a perplexity of 10 and 1,500 iterations to examine the differential expression of CD13 and NG2 in control versus hypertensive pericytes.

2.9 Plasma-derived extracellular vesicles

Peripheral blood was collected from the portal vein of anesthetized animals using a 21G butterfly needle, immediately mixed with acid citrate dextrose (ACD), and subjected to two inversions for agent incorporation. Samples were processed within 1 h, as previously described (152). Briefly, plasma separation was initially achieved by centrifugation at 1500 g for 10 min, which was then transferred to sterile 1.5 ml Eppendorf tubes. To isolate EVs, the plasma underwent two centrifugation cycles at 1500 g for 10 min maintaining supernatant, followed by two rounds of ultracentrifugation at 14,000 g for 70 min, discarding supernatants and resuspending pellets in 0.22 µm filtered PBS (fPBS -/-). The final EV pellet was resuspended in 200 µL of fPBS -/- and stored at -80 °C. For EV characterization, 10 µl of isolated EVs was then mixed with 90 µl of fPBS -/-, and samples were labeled with CD9, CD63, and CD81 (APC-conjugated, Clones HI9A, H5C6 and 5A6, respectively, Biolegend). Samples were analyzed using an Attune NxT Flow Cytometer equipped with a small particle side scatter filter. Size gating (300-1000 nm) was established using silica beads (Creative Diagnostics). Acquisition of samples was performed at a speed of 25 µl per min, with SSC threshold set to 0.18 x 103 and FSC threshold set to 0.15 x 103. A stop option was activated upon reaching 150,000 events within the size gate. Each sample measurement was followed by a 10 % bleach and 0.22 µm filtered distilled water rinse. Data analysis was conducted using FlowJo 10.9.0 and GraphPad Prism 10 for subsequent downstream analyses.

2.10 JC-10 Mitochondrial membrane potential assay

Enriched pericytes at 90-95 % confluence from T-75 cell flasks derived from control rats were expanded and seeded in 96-well plates at a density of 10,000 cells/well for 24 h prior. Cells were subjected to a JC-10 mitochondrial membrane potential assay (Cat. no. 421902, BioLegend) to assess metabolic responses to plasma and plasma-derived extracellular vesicles (pdEVs). Before stimulation cells were incubated in pericyte ultracentrifuged (18 h, 110,000 g) basal medium containing 1 % FCS. Treatments included 10 % v/v normotensive or hypertensive plasma, or normotensive or hypertensive pdEVs standardized to a protein concentration of 13.5 µg. All stimulations were induced for 6 h. JC-10 dye was added following the manufacturer's instructions, and changes in mitochondrial membrane potential were measured by calculating the ratio of

red/green fluorescence ratio indicative of mitochondrial health using the AttuneNxT and Flowjo Analysis Software (v10.5.3).

2.11 Extracellular flux analysis

Metabolic profiles of hypertensive and control rat pericytes were determined using a Seahorse XFp Extracellular Flux Analyzer (Agilent Technologies, CA, USA). Mitochondrial respiration, glycolysis rate, and real-time ATP production rate were measured using suitable kits (Cell Mito Stress Test, Glycolysis Stress Test, Real –Time ATP Rate Assay) according to the manufacturer's instructions and as already shown (153). Briefly, after cell harvesting, pericytes were resuspended in culture medium and seeded at 1.5 x 104 cells/well in Seahorse cell culture microplates and incubated overnight in a CO_2 incubator. After replacing the growth medium with pre-warmed assay XF DMEM medium pH 7.4 supplemented with 1 mM pyruvate, 2 mM glutamine, and 10 mM glucose for Mito Stress Test and ATP production rate and only with 2 mM glutamine for Glycolysis Stress Test, the cells were preincubated at 37 °C for 45 min. in a non-CO_2 incubator. The cartridges were loaded with assay medium and with standard inhibitors/substrates: 5 µM oligomycin, 2.25 µM FCCP, and 1 µM rotenone/ antimycin A mixture for Mito Stress Test and with 10 mM glucose, 5 µM oligomycin, and 50 mM 2-deoxy-glucose for Glycolysis Stress Test or with 5 µM oligomycin and 1 µm rotenone/antimycin A mix for ATP production rate measurement. For experiments with metabolic inhibitors first port of cartridge was loaded with cocktail of mitochondrial inhibitors (2 µM UK5099, 3 µM BPTES, 4 µM Etomoxir or glycolysis inhibitor (50 mM 2-DG) and last 3 ports with standard inhibitors. After the cartridges were calibrated, measurements were initiated. For ATP production rate measurements, the assay medium in cell microplates was again changed to fresh one. The Seahorse assays were analyzed using XF Wave 2.6.1 software, according to manufacturer´s instructions. After the measurements, cells were collected and lysed using RIPA buffer, and diluted with PBS. Total protein concentrations were measured on an absorbance microplate reader Sunrise (TECAN, Switzerland) using BCA Protein Assay (Sigma-Aldrich, CA, USA). For all calculations, oxygen consumption rate (OCR) and extracellular acidification rate (ECAR) were normalized to the total amount of protein in each well and expressed per µg of protein. Cell Mito Stress Test was used to investigate most important mitochondrial properties: proton leak, ATP linked respiration, maximal respiration, and spare respiratory capacity. Glycolysis Stress Test was used to study glycolytic function of pericytes, and ATP test to explore real-time ATP production rate in control and hypertensive pericytes.

2.12 Human subjects

Brain tissue of 9 human autopsy cases were included into the study. Brains of all subjects underwent routine neuropathological examination and were screened for tauopathies, alpha-synucleinopathies and beta-amyloid (Aβ) deposition. Inclusion criteria for cSVD cases for entering the study were pathologically confirmed white matter lesions (WML). Control cases were randomly selected within the same age range as the cSVD cases. Exclusion criteria for all cases were a history of neurodegenerative disorders, i.e., Alzheimer-related tau pathology exceeding Braak's neurofibrillary stage II (154) or other tauopathy, Parkinson's disease except incidental subcortical Lewy bodies in the lower brain stem (stage <3) according to Braak et al (155), multisystem atrophy or other alpha-synuclein-related pathology. Altogether 4 cases with cSVD (3 females, 1 male) and 5 control cases (3 females, 2 males) were investigated. The age range of the two groups presented as mean ± SD were 64.0 ± 16.0 in the cSVD group and 63.7 ± 12.7 in the control group. Further demographics and relevant data for the patient cohort are provided in Table 6. This retrospective study was performed in compliance with the University Ethics Committee guidelines as well as German federal and state law governing human tissue usage. Informed written permission was obtained from all patients and/or their next of kin for autopsy. This work on human tissue was possible thanks to the collaboration with Prof. Deniz Yilmazer-Hanke from the Clinical Neuroanatomy Department of Neurology, Institute for Biomedical Research, Ulm University, Germany.

Table 6 List of post-mortem human patient samples used for microglia analyses

Randomized Case-Code	Age	Sex	Group	cSVD -Type	NFT Stage (Gallyas)	Aß Stage	Aß Phase	PD (LB)	Diagnosis
Case1	54	f	Control	n/a	I	B	3	0	Ovarian cancer
Case5	65	m	Control	n/a	I	0	0	0	Myocardial infarction
Case4	71	f	Control	n/a	0	0	0	0	Left heart failure
Case8	74	m	Control	n/a	II	0	0	0	COPD, right heart failure, post-tuberculosis
Case9	74	f	Control	n/a	II	A	1	0	Myocardial infarction

Case6	49	m	cSVD	WML	I	A	1	1	Arterial hypertension, cardiac arrhythmia
Case 7	57	f	cSVD	WML	0	0	0	0	Non-hodgkin lymphoma
Case3	69	f	cSVD	WML	I	A	1	0	Pontine bleeding
Case2	81	f	cSVD	WML	I	A	1	0	Post-ischemic infarct (MCA-l)

List of postmortem human patient samples used including randomized case-code, age, sex, group, type of cSVD, NFT stage, Aß stage, Aß phase, PD (LB) and diagnosis. Aß – amyloid beta; COPD – chronic obstructive pulmonary disease; cSVD – cerebral small vessel disease; LB – Lewy bodies; MCA – middle cerebral artery; n/a – not applicable; NFT – neurofibrillary tangles; PD – Parkinson's disease; WML – white matter lesions.

2.13 Histology and neuropathological evaluation in human post-mortem tissue

Routine neuropathological investigations were performed using hematoxylin & acid fuchsine (modified H&E), advanced silver stains, and single- and double-label immunohistochemistry as previously described (156,157). Briefly, brains were fixed in a 4 % solution of formaldehyde and cut in approximately 1 cm-thick coronal slabs. Tissue slabs and blocks of the frontal, mid-hemispheric, and occipital regions, the cerebellum and various brainstem regions (rostral medulla, pontine-mesencephalic junction and midbrain) were embedded in polyethylene glycol (PEG 1000, Merck, Carl Roth Ltd, Karlsruhe, Germany). Multiple 100 µm thick consecutive sections were obtained from each embedded tissue block with the aid of a sliding microtome (Jung, Heidelberg, Germany). Enlargement of subcortical perivascular spaces, hyalinosis of subcortical perforating vessels in the white matter and basal ganglia area as well as presence of WML were assessed in the modified H&E stain (156). Stages of Alzheimer-related neurofibrillary changes were visualized using the Gallyas silver stain (154). Extracellular deposits of Aβ peptide were immunostained with the mouse anti-β-amyloid 17-24 antibody (1:5000, clone 4G8, BioLegend, Koblenz, Germany). Alpha-synuclein pathology was detected with the anti-syn-1 antibody (1:2000, clone number 42; BD Biosciences, CA, USA). For visualization of microglia and vessels, sections were treated with 10 % methanol and 3 % concentrated H2O2 in Tris-buffered saline (TBS). Epitopes were unmasked using pretreatment with 1.3 µg/ml proteinase K for 10-15 min at 37 °C (Invitrogen, Darmstadt, Germany). After blocking of unspecific binding sites with bovine serum albumin (BSA), sections

were incubated with the primary antibody against IBA1 (1:500, Abcam, Cambridge, UK) over night, a secondary biotinylated antibody (1:200; 2 h, room temperature, Vector Laboratories, Burlingame, CA, USA), and the avidin-biotin-peroxidase complex (ABC Vectastain, Vector Laboratories, Burlingame, CA, USA). The immunoreaction was visualized using 3,3′-diaminobenzidine tetrahydrochloride (DAB; Sigma Taufkirchen, Germany). Next, sections were washed with TBS at 95 °C for 5 min, retreated with 10 % methanol and 3 % concentrated H2O2, and incubated for 48 h with Ulex europaeus lectin I (UEA-l; 1: 800, biotin-coupled, GeneTex, Irvine, CA, USA). Subsequently, sections were incubated with the ABC kit solution, and the reaction product was visualized with a blue chromogen (SK-4700, Vector Laboratories). Omission of all primary antibodies and the lectin resulted in lack of staining.

2.14 Image acquisition in human post-mortem tissue

Images were taken using an Eclipse LV100ND microscope equipped with a digital DS-Fi3 camera and the NIS-Elements software (NIKON GmbH, Düsseldorf, Germany) from the cingulate gyrus of 100 µm-thick hemisphere sections labeled with double-label immunohistochemistry for IBA-1 and UEA-l. The position for image acquisition was randomly selected with the 4x objective and z-stack images were acquired with the 20x objective (image area size 675,470 µm2). The N.I.H. ImageJ software was used to generate minimum intensity projections (MIP) from the z-stack images after image brightness was optimized, noise reduction was performed (despeckle command), and the median filter (radius 2.0) was applied in z-stacks. Next, Adobe Photoshop was used for autothresholding and autocontrasting, and to invert the colors of MIP images. The latter step allowed to obtain microglia and vessels with bright colors in a dark background for the quantification of microglia morphologies with established image analyses pipelines. Using ImageJ, the background of inverted images was subtracted (rolling ball radius 50.0 pixels, using “separate colors“ and “sliding paraboloid“ options), and images were reopened in Adobe Photoshop. The inverted blue color of microglia was assigned green and the inverted magenta color of vessels were assigned red using the channel mixer in Adobe Photoshop to further improve the color contrast between microglia and vessels. Inverted images with double labeling were used to quantify the overall microglia cell density and the density of vascular associated mircoglia (VAM) (analyzed in MIP generated from z-stacks with 25 images; 2880 x 2048 pixels with a voxel size of 0.11 x 0.11 x 1.5 µm3). The VAMs were defined as IBA1-positive cells with their somata attached to UEA-l-labeled vessels. To analyze single-cell microglia morphologies, new inverted images were generated (19-53 images in z-stack) to maximize the number of microglia analyzed per case in the

MIP images (larger stacks in cases with lower microglia densities, and vice versa to avoid overcrowding / overlay of cells). From these latter images with IBA1-positive cells (green) and UEA-l-labeled vessels (red), red vessels and shades (out-of-focus areas in MIPs) were removed by using the "remove color" function with thresholding in Adobe Photoshop. To characterize microglia morphology, the somata were manually outlined for each cell and quantified using the measure function. To investigate the branching complexity of individual cells, microglia were automatically thresholded using the Triangle option and size filtering of >2000 pixels, so that the single-cell branching area as well as the cellular solidity, i.e., cellular branching area / convex hull area, could be estimated. For simplicity and consistency, the cellular solidity is called two-dimensional (2D) ramification index in the rest of this thesis since it corresponds to the 3D ramification index in rodents. The analyses were performed blinded to the pathological groups.

2.15 Immunofluorescence in rodent tissue

Animals were transcardially perfused under pentobarbital anesthesia (40 mg/kg body weight i.p.) with 120 mL of phosphate buffered saline followed by perfusion with 120 mL of the fixative 4 % paraformaldehyde (PFA) within 8 min. Brains were removed, immersion-fixed in 4 % PFA for 48 h, cryoprotected in 30 % sucrose for 6 days, and frozen in methyl butane at −80 °C. Using a cryostat, brains were sectioned from the frontal to the occipital pole, and 30 µm-thick free-floating sections were collected in PBS. Immunofluorescence staining was performed as previously described (134). Two coronal brain sections were stained, containing the hippocampus and retrosplenial cortex of both hemispheres per animal (coronal sections Bregma -2.5 to -4.5 [19]). Sections were repeatedly washed in phosphate-buffered saline (PBS), blocked with 10 % donkey serum/0.5 % Triton X-100 (Sigma, St Louis, MO, USA), and incubated overnight at 4 °C with STL-FITC (dilution 1:750, solanum tuberosum lectin-fluorescein isothiocyanate, endothelial marker, Vector Laboratories FL-1161) and goat anti-IBA1 (dilution 1:1500, ionized calcium-binding adapter molecule 1, microglial marker, Novus Biologicals NB100-1028). Sections were incubated for two hours the following day with donkey anti-goat Cy5-conjugated secondary antibodies (dilution 1:500, Jackson ImmunoResearch, 703-175-155) and mounted on slides with Fluoromount Aqueos Mounting Medium (Merck, F4680).

2.16 Image acquisition and analysis in the SHRSP model

A total of 20 animals were utilized for the immunofluorescence analysis, with 5 SHRSP assigned to early chronic hypertension, 5 SHRSP for late chronic hypertension, and 5 age-matched

normotensive controls for each stage of hypertension. Immunofluorescence images were acquired using a Zeiss confocal microscope (LSM 700). The 20x objective was used for overall microglia soma counting, size quantification and blood vessel association. Z-stack images (8-bit, 512 × 512 pixels with a voxel size of 1.25 × 1.25 x 1 µm3) were taken from 10 fields of view per animal in the hippocampal CA1 region and overlying retrosplenial cortex, respectively. While a comparatively low hippocampal atrophy has been classically regarded as a parameter that allows the distinction of subcortical cSVD from AD (158), recent evidence suggests that hippocampal atrophy (including subfield CA1) can be associated with cognitive decline in cSVD (159,160). In the present study, we therefore focused on hypertension-related microglial changes in the hippocampal CA1 subfields as well as the retrosplenial cortex that is connected to the hippocampal formation through limbic circuits. Single-cell morphological analyses were performed in high-resolution images acquired with the 40x/oil objective. Z-stack images (8-bit, 1024 x 1024 pixels with a voxel size of 0.16 x 0.16 x 0.3 µm3) were taken out of 4 fields of view per animal per region, retrosplenial cortex and hippocampal CA1 region, respectively. Thereby, 15-20 microglial cells were analyzed per animal in each brain region. Gain and laser power were kept equal for all animals.

For studying vascular-associated microglial, image analyses were performed using openly available ImageJ software and a Phyton3-based in-house routine. For hippocampal images, rectangles were manually cropped out, so that the CA1 region was included. Pre-processing contained z-projection (maximum intensity), subtraction of background (rolling ball radius: 50 pixels), and median filter to remove salt and pepper noise. For microglia soma segmentation, automatic thresholding with moments dark option and size filtering > 60 µm2 was used to quantify the mean microglial soma size of IBA1+ cells. For vessel segmentation in STL-labeled images, the OMELETTE framework was adapted (161) (https://gitlab.com/hmattern/omelette). First, blood vessels were enhanced using a multi-scale Frangi filter (162). To adapt the filter's vessel sensitivity parameter gamma per image, i.e., to provide robust vessel enhancement for varying pixel intensity distributions, gamma was selected empirically to be 40 % of the image's maximum absolute Hessian eigenvalues. Thereafter, a multi-scale Frangi filter was applied (filter scales 1, 2, 3, 4, 5 pixels). Subsequently, the blood vessels were segmented from the enhanced images by applying hysteresis thresholding (163). For hysteresis thresholding, which requires a lower and upper threshold, the three-class Otsu's method (164) was used to estimate the two required thresholds from the enhancement distribution (self-tuned threshold estimation). Finally, the relative number

of microglia soma tangent to the vessel segmentation was estimated. To analyze the three-dimensional (3D) microglia branching morphology in rodents, we applied the 3DMorph automatic analysis workflow via MATLAB on high-resolution images (165). Using the interactive mode guaranteed correct cell segmentation. Thereby we obtained single cell estimates of cell volume, cell territory volume, i.e., the volume of a 3D convex hull connecting the endpoints of branches, 3D ramification index (i.e. cell volume / territory volume), number of endpoints, number of branchpoints, and average branch length. The analysis was conducted in a blinded manner with respect to the pathological groups.

2.17 Microglia cell isolation for flow cytometric analysis

This experimental cohort consisted of a total of 22 rodents, with 5 SHRSP rats assigned to the early hypertension group and their corresponding age-matched normotensive controls, in addition to 6 SHRSP rats assigned to the late hypertension group and their age-matched normotensive controls. Each stage was performed twice as specified in Table 2. For anesthesia, pentobarbital (40 mg/kg body weight) was intraperitoneally injected in all animals. Transcardial perfusion was conducted with 120 ml of sterile PBS. Brains were divided into two sagittal halves, of which one was processed for flow cytometric analysis, and the other half was processed for microvessels isolation (see 2.3). The hemisphere processed for microglia cell characterization via flow cytometric analysis was cleaned of meninges and dissected into specific regions (cortex and hippocampal region). Each region was collected in a separate tube. Tissues were disrupted in a glass homogenizer in a buffer containing Hanks' balanced salt solution (HBSS), 1 mM HEPES (pH 7.3), and 45 % glucose and passed through a 40 µm cell strainer. The suspension was centrifuged at 400 g for 20 min, and 1 ml supernatants from each corresponding brain region were transferred into 2 ml polypropylene collection tubes for cytokine immunoassays. The brain suspension was followed by a discontinuous 30 to 70 % (Percoll) density gradient. After myelin aspiration, immune cells were collected from the 30/70 % Percoll interphase, filtered using a 70 µm cell strainer, washed with RPMI, and resuspended in FACS buffer (2 % fetal calf serum in PBS) containing EDTA. Cells were washed, transferred to flat-bottom 96 well plates, and immediately processed for subsequent flow cytometric analysis. According to the cell yield after isolation, each sample was aliquoted three times up to 1.5 x 10^5 cells adjusted for staining in 100 µl ice-cold FACS buffer. Prior to fluorochrome-conjugated antibody labeling, cells were incubated for 15 min at 4 °C with a purified mouse anti-rat CD32 FcγII (clone D34-485, Rat BD Fc Block) to block unspecific binding. Thereafter, cells were stained with a mixture of fluorochrome-conjugated antibodies in 100 µl of

FACS buffer for 30 min at 4 ºC. Cells were washed twice and resuspended in 200 µl of FACS buffer. The mixture of fluorochrome-conjugated antibodies included Zombie NIR™, anti-CD45 (clone: OX-1), anti-CD11b (clone: OX-42), anti-CX3CR1 (clone: SA011F11), anti-P2Y12R (polyclonal), anti-CD86 (clone: 24F), anti-CD200R (clone: OX-102), anti-RT1B (clone: OX-6), and anti-CD163 (clone: ED2). Single live cells were identified by the exclusion of doublets, cell debris and gating of viable cells using a live/dead dye. Traditionally, microglia are identified as $CD11b^{+}CD45^{int}$, whereas $CD11b^{+}CD45^{high}$ population corresponds to other central nervous system (CNS) macrophages (166). However, microglia respond to inflammatory states upregulating CD45 (84,167) resulting in incorrect classification of microglia as bone marrow-derived macrophages. Therefore, in this study, the main populations of cells were identified through Forward Scatter light (FSC) and CD45 expression for both early and late chronic hypertension with their respective age-matched normotensive controls. Target cells were further gated as $CD45^{+}$ and $CD11b/c^{+}$ cells. Cells positive for CD45, CD11b/c, and P2Y12R were classified as microglia from the hippocampus (Fig. 35a) and cortex (Fig. 35b). P2Y12R has been identified as a receptor selectively expressed on microglia and can be used as a marker to distinguish CNS resident microglia from blood-derived myeloid cells (94,168). We have developed such gating strategy considering microglia activation appropriate for its senescent and inflammatory response that yields them indistinguishable from recruited myeloid cells. Optimization was performed using antibody titrations, and FMO controls to assess background fluorescence in the respective detection channel. Samples were acquired on AttuneNxT and analyzed with Flowjo Analysis Software (v10.5.3).

2.18 Population identification and high-dimensional data analysis

Sample data were acquired on the AttuneNxT Flow Cytometer (Thermo Fisher Scientific), exported into FlowJo version v10 (TreeStar), compensated, and subjected to unbiased analysis as previously described (169,170). First, manually annotated gatings were used to calculate the relative frequencies of microglia and leukocyte populations. Second, microglia manual gating was selected to export live single cells for dimensionality reduction. UMAP analysis was performed for cell visualization from each brain region, i.e., hippocampus and cortex, separately, including exported clean live microglia from both control rats and SHRSP. For the hippocampus: 7,500 microglia cells per animal were randomly subsampled and used to generate the hippocampus UMAP plot. For the analysis of cortex microglia: 10,000 microglia cells per animal were randomly subsampled and used to generate the combined cortical UMAP plots. A total of 75,000-120,000 cells were analyzed per region and included all compensated markers except dead cells dye staining

unless otherwise specified. Microglia cells from both groups were plotted together on a single UMAP for each time point. UMAP parameters were established as follows: local connectivity set to 0.5; size of local neighborhood set to 35; minimum distance of two points set to 0.3; Euclidean distance metric used; and 2 components/dimension estimated. For cluster characterization, the FlowSOM algorithm was run on the merged dataset to cluster every cell after evaluating refined sub-clusters found by Phenograph. Summary tables containing expression levels of each marker, cell frequencies, and cell numbers of UMAP datasets were exported, and total cell fraction per cluster was calculated. Heatmaps display normalized median expression levels from lowest to highest of all markers per merged sub-population group.

2.19 Statistical Analysis

Data analyses were performed using GraphPad Prism software (versions 9.3.1 and 10). All data were assessed for normality using the Shapiro-Wilk test. Data are presented as mean ± standard error of the mean (s.e.m), and the exact numbers for each dataset are detailed in figure legends. Parametric unpaired t-tests were used to compare normally distributed data between two groups. For two group comparisons with unequal variances, the statistical significance was analyzed using a two-tailed Student's *t* test with Welch's correction. For comparison between multiple groups, one-way ANOVA was performed followed by Holm-Sidak to correct for multiple comparisons. For comparison between multiple groups and conditions, the data were analyzed using two-way ANOVA followed by Holm-Sidak post hoc correction. Results from independent experiments, are included, with data shown as independent data points unless specified otherwise. *P*-values were interpreted as follows to denote statistical significance: * for $p \leq 0.05$, ** for $p \leq 0.01$, *** for $p \leq 0.001$, and **** for $p \leq 0.0001$.

2.20 Software

Data analyses and visualization were performed using a variety of software tools tailored for specific needs. FlowJo v.10 with UMAP and Phenograph plugins installed with R (Version 4.3.3) and R libraries: flowCore, FlowSom, pheatmap were utilized for flow cytometric data analyses. For microglia morphological analyses and association to the vasculature Python (Version 3.9) supported advanced data processing was installed, with the open-source UMAP package accessed via (https://umap-learn.readthedocs.io/en/latest/index.html). Microglia IF image analyses were facilitated by MATLAB-based Cyt3 software, and 3D morphological reconstruction was achieved

by employing an open-source script, 3DMorph, also in MATLAB. ImageJ (Rasband, W.S., https://imagej.nih.gov/ij/, 1997-2018) was used for IF image processing and analysis.

For documentation and presentation of findings, Microsoft Word was employed for manuscripts and thesis preparation, while Microsoft Excel was used extensively for data organization and preliminary analysis. Graphical illustrations and figures were created using Adobe Illustrator, GraphPad Prism and BioRender®. Specific microglia image modifications i.e. thresholding and constrast, were performed using Adobe Photoshop. Adobe Acrobat was utilized for creating and editing PDF files to ensure high-quality digital document production.

3 Results

Cerebral pericytes response under hypertensive stress

In the context of cerebral small vessel disease (cSVD), cerebral pericytes play a critical role in maintaining vascular stability and responding to physiological stresses. Utilizing the spontaneously hypertensive stroke-prone rat (SHRSP) model, which closely mimics hypertensive cSVD in humans, this chapter focuses on how cerebral pericytes adapt to the continuous strain of arterial hypertension. Under hypertensive conditions, pericytes exhibited significant phenotypic alterations and metabolic shifts early in disease progression, with increased dependency on glycolytic pathways. This chapter presents novel findings on the phenotypic and metabolic changes in brain pericytes due to prolonged hypertension and explores the involvement of extracellular vesicles (EVs) in mediating vascular pathology observed within the neurovascular unit (NVU).

3.1 Stage-specific brain vascular cells adaptation to hypertensive stress

In our cross-sectional study, we examined the effects of hypertension across three defined stages: initial hypertension (HTN), early chronic HTN, and late chronic HTN stages in the SHRSP model on brain microvascular cells (Fig. 8).

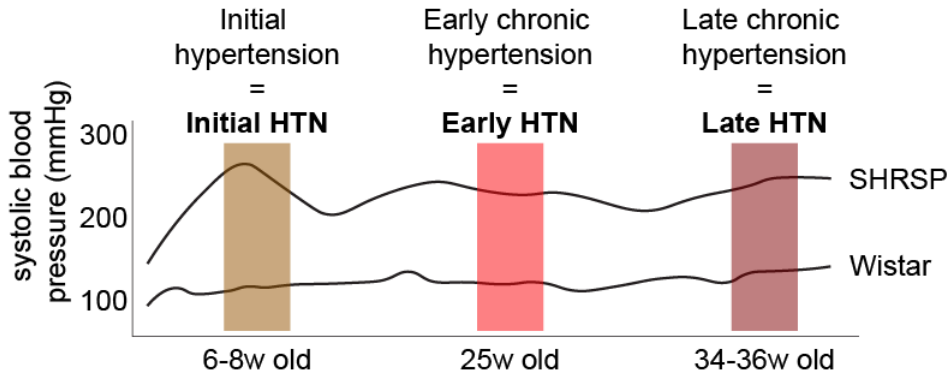

Fig. 8 Longitudinal analysis of systolic blood pressure in SHRSP and Wistar rats across three different stages of arterial hypertension

Depiction of the progression of systolic blood pressure (mmHg) in spontaneously hypertensive stroke-prone (SHRSP) rats, illustrating an increase from initial hypertension (6-8 weeks old) to early chronic hypertension (25 weeks old), and late chronic hypertension (34-36 weeks old). Wistar rats serve as age-matched normotensive controls across the studied time points. The age of the rats at the studied time point is indicated on the x-axis. Distinct color coding represents each hypertension stage and will be consistent in subsequent graphs to facilitate comparison and visual coherence.

We identified brain vascular cells, particularly differentiating endothelial cells ($CD31^{+}$) from pericytes ($PDGFR\beta^{+}$) (Fig. 9).

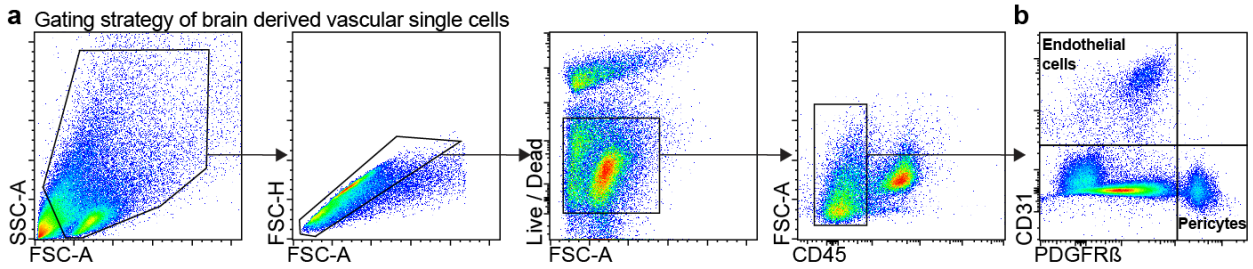

Fig. 9 Gating strategy for flow cytometric analysis of brain vascular single cells

(a) Initial gating based on forward scatter area (FSC-A) and side scatter area (SSC) light properties to distinguish cell populations by size and internal complexity (granularity), respectively. Further selection using FSC-Area (FSC-A) vs. FSC-Height (FSC-H) to select single cells by eliminating cell doublets and aggregates. FSC-A vs. Live/Dead gating was performed to select live single cells, excluding dying or dead cells based on their permeability to the viability dye. CD45 vs. FSC-A gating was performed to exclude CD45-positive hematopoietic cells, focusing on vascular cell populations. (b) Subsequent gate to identify CD31-positive endothelial cells and PDGFRß-positive pericytes.

Our initial identification of pericytes was based on the positive selection of PDGFRß, a marker expressed in all pericyte subtypes (66), and subsequently subdivided pericytes based on their expression of NG2 and CD13(66). Our results showed that at the onset of HTN, the frequency of $CD31^+$ endothelial cells and the vascular pericyte compartment remained consistent between groups (Fig. 10a-c). During early chronic HTN (Fig. 10d, e), the vascular system adapts to persistent hypertensive conditions, resulting in enhanced expression of NG2 and double the amount of CD13 pericytes compared to controls (11 % vs. 23 %, $p = 0.0335$). A significant decrease was observed in frequency of $PDGFR\beta^+$ cells in HTN (13 % vs. 8 %, $p = 0.0399$) (Fig. 10f), while the frequency of $CD31^+$ endothelial cells remained stable between groups. This result showed a specific susceptibility of pericytes to early chronic HTN stress (Fig. 10f). In late chronic HTN, NG2 expression dominated the pericyte population (Fig. 10g, h). Quantitative analysis revealed that in controls, only a small fraction of $PDGFR\beta^+$ cells co-expressed CD13 (3 %), while a substantial majority co-expressed NG2 (77 %). In contrast to early chronic HTN, CD13 co-expression decreased to 7 %, NG2 co-expression remained the same, and $PDGFR\beta^+$ expression increased, indicating a nuanced yet significant shift in pericyte subtypes (Fig. 10h). Furthermore, we observed a significant increase in the frequency of $CD31^+$ endothelial cells in late chronic HTN (20 % vs. 11 % in controls, $p < 0.0001$) and a modest rise in the freq. of $PDGFR\beta^+$ HTN pericytes (12 % vs. 10 % in controls, $p = 0.032$) (Fig. 10i).

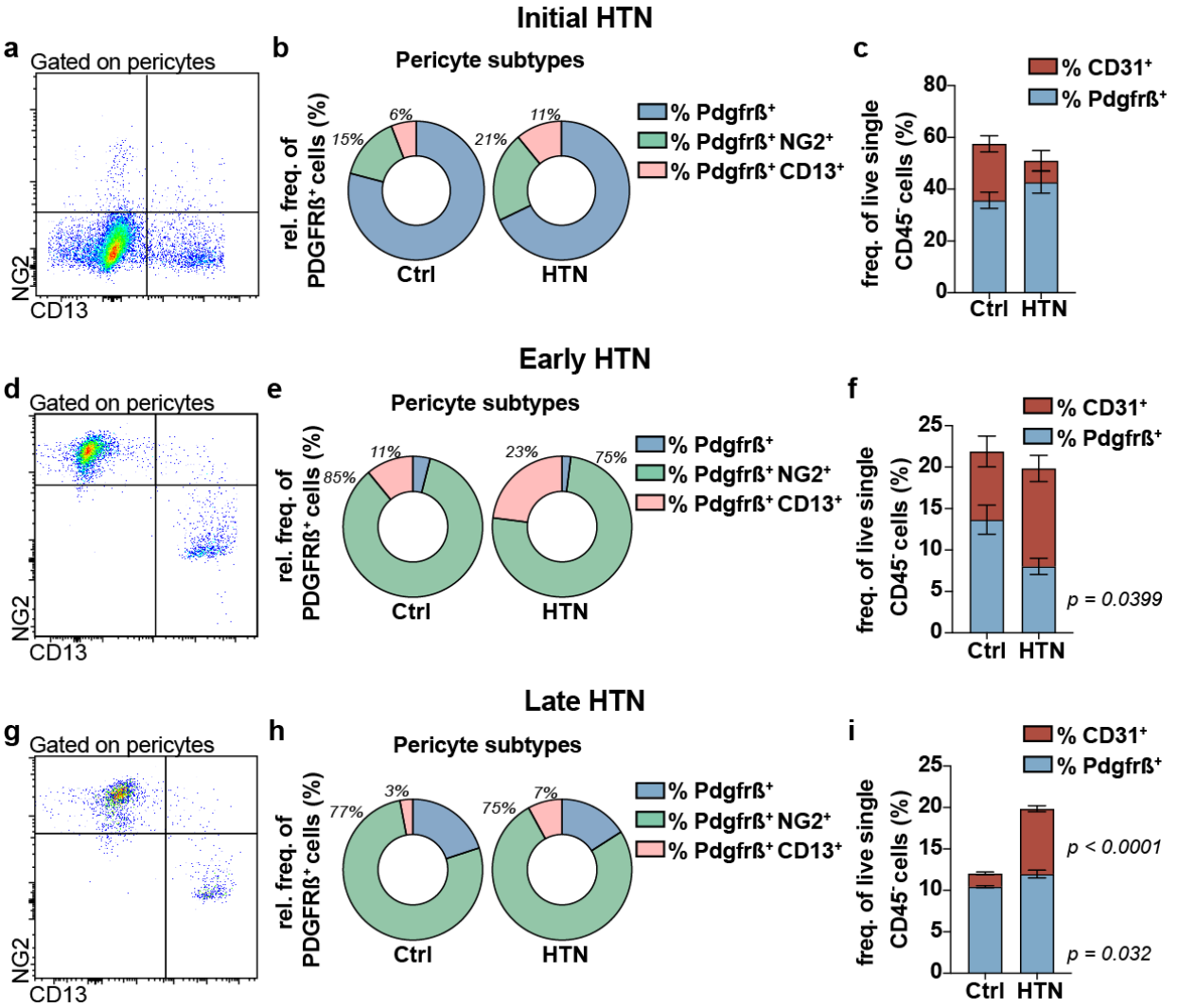

Fig. 10 Progressive phenotypic shifts in brain pericytes across arterial hypertensive states

Pericyte subtypes identification across hypertension states: initial HTN (a), early chronic HTN (d), and late chronic HTN (g) states; subsequent flow cytometry gate after positive selection of PDGFRß$^+$ (Fig. 9b). Differential expression of NG2 and CD13 among PDGFRß$^+$ pericytes is depicted as pie chart to represent the percentage distribution of pericyte subtypes (b, e, h). Bar charts comparing the relative frequencies of CD31$^+$ endothelial and PDGFRß$^+$ pericyte populations (c, f, i). For experimental methodology see section 2.2. n=6 per group for initial and early chronic HTN, n=5 per group for late chronic HTN; experiments were performed twice per group per time point. Data are presented as mean ± s.e.m.

3.2 Differential proliferative capacity of brain endothelial cells and pericytes in hypertensive states

We conducted further analyses to investigate the proliferative responses of endothelial cells and pericytes across hypertension phases. In the initial HTN (Fig. 11a-d), while the absolute numbers of endothelial cells remained stable, there was a significant increase in Ki67 expression in the hypertensive group (Fig. 11a, b). Conversely, there were no discernible differences in the absolute

numbers of PDGFRß$^+$ pericytes or their Ki67 expression between Ctrl and HTN displaying an early resilience in response to hypertensive stress (Fig. 11c, d). In early chronic HTN (Fig. 11e-h), endothelial cells maintained stable numbers without the same proliferative increase observed in pericytes. During this phase, there was a significant reduction in the absolute number of pericytes in HTN alongside an increase in Ki67 expression, depicting pericytes under stress, both decreasing in number and increasing in proliferative activity (Fig. 11g, h), pointing to a unique interplay between the cellular responses of each vascular component. In the late stage of chronic HTN (Fig. 11i-l), while endothelial cells displayed a significant increase in both numbers and Ki67 expression in HTN, our results showed a significant increase in the number of pericytes and a decrease in Ki67 expression.

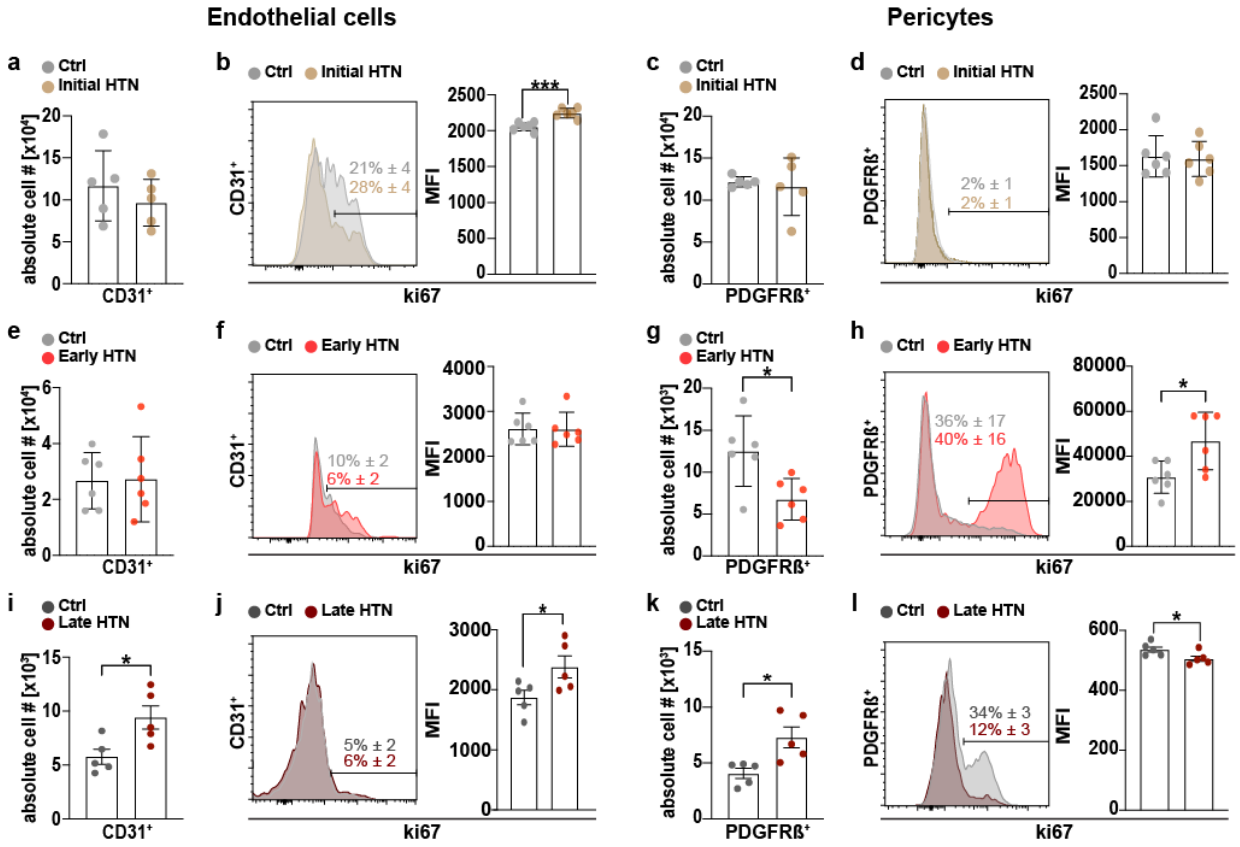

Fig. 11 Vascular cell abundance and proliferation across hypertension states

Analysis of endothelial cells and pericytes abundance across hypertension states. Row-wise representation of initial HTN (a-d), early chronic HTN (e-h), and late chronic HTN stages (i-l), detailing absolute numbers of PDGFRß$^+$ pericytes and CD31$^+$ endothelial cells comparing control (Ctrl) vs. hypertensive (HTN) groups. Histograms and bar graphs represent Ki67 expression and quantification of CD31$^+$ and PDGFRß$^+$ cells. For experimental methodology see section 2.2. Each data point represents one biological sample, experiments were performed twice per group and time point. Data are presented as mean ± s.e.m. *$p < 0.05$, ***$p < 0.001$.

3.3 Tracing the development of vascular markers in hypertension progression

Building on our comprehension of hypertension-associated vascular remodeling, we aimed to delineate the dynamic vascular profile throughout the progression of hypertension. Using UMAP analysis, we projected $CD31^+$ and $PDGFR\beta^+$ cells to discern between shifts in vascular cell properties (Fig. 12a). We set to characterize different aspects of vascular cell behavior that underlie the significant changes observed in cellular marker expression and population dynamics across different stages of hypertension. We investigated the vascular identity of hypertension (Fig. 12b), revealing a multifaceted landscape where CD31, PDGFRß, NG2, and CD13 expressions converge. This analysis revealed an evolving expression pattern of endothelial and pericyte markers, pinpointing the location of PDGFRß clusters and identifying subclusters expressing NG2 and CD13, which point to the intricate interplay within the vascular cell milieu.

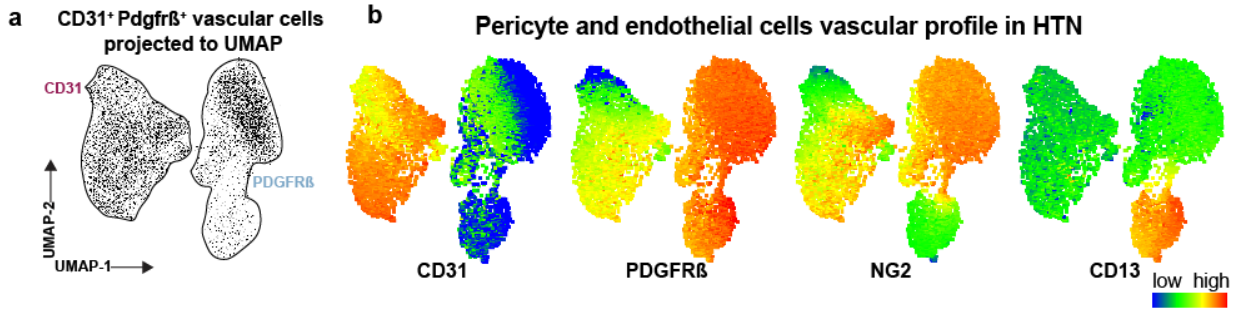

Fig. 12 UMAP analysis and visualization of marker expression in vascular cell clusters

(a) UMAP plot derived from the projection of $CD31^+$ and $PDGFR\beta^+$ cells. UMAP plots are a technique used for dimensionality reduction that helps visualize complex, multidimensional data in two dimensions. Here, the distribution of $CD31^+$ endothelial cells and $PDGFR\beta^+$ pericytes is illustrated, enabling the identification of distinct cell populations within the vascular compartment. (b) Representative heatmaps showing the expression levels of CD31, PDGFRß, NG2, and CD13 within the vascular UMAP vascular clusters to depict overlapping expression of investigated pericyte markers.

Normalizing MFI to the initial control expression levels of CD31, PDGFRß, NG2, and CD13 allowed us to trace the marker expression trajectory throughout hypertension development (Fig. 13a). Initial and late chronic hypertension stages exhibit elevated CD31 expression showing an endothelial component reacting to hypertensive conditions. Conversely, PDGFRß expression peaked in initial controls, while NG2 and CD13 expressions dominated the hypertensive groups, especially in the chronic phases. Lastly, we aimed to encapsulate the spatial and temporal shifts in marker expression profiles to provide a clear visual narrative of each individual marker over time. Our results showed the phenotypic shift in critical vascular markers, illustrating the complex development of vascular identity under the influence of hypertension (Fig. 13b).

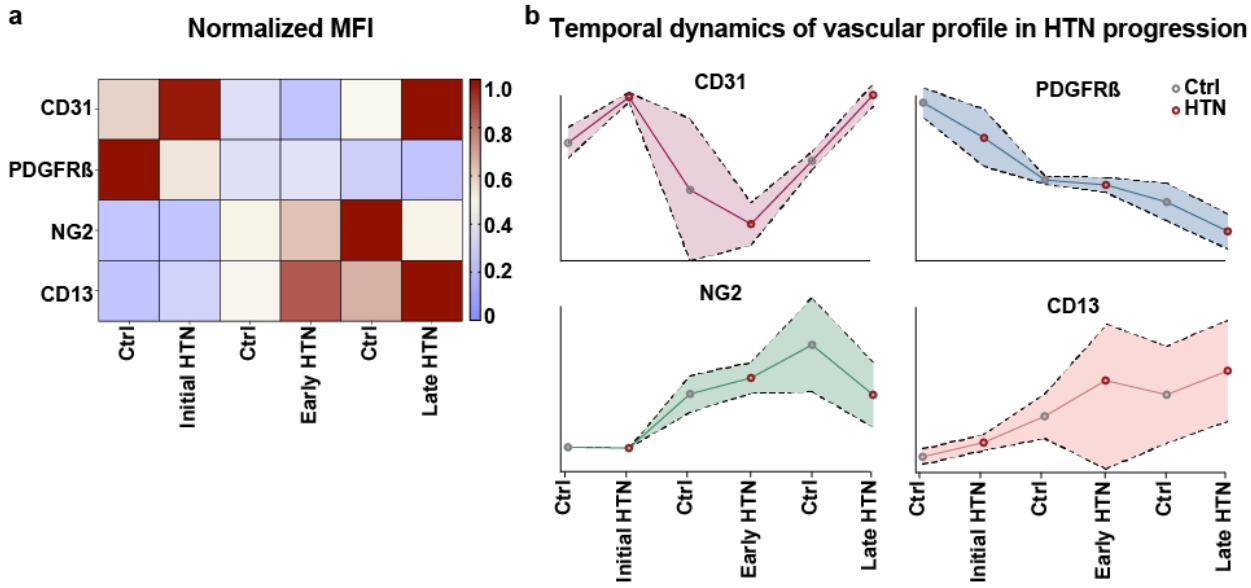

Fig. 13 Temporal dynamics of vascular cell marker expression across hypertension progression

(a) Heatmap of vascular cells expression levels of CD31, PDGFRß, NG2, and CD13 across six groups: initial control, initial hypertension, early chronic control, early chronic hypertension, late chronic control, and late chronic hypertension, from two independent experiments per time point, shown as normalized mean fluorescence intensity (MFI) values to the expression levels of the initial control group. For experimental methodology see section 2.2. (b) Line graphs displaying the temporal progression of marker expression for CD31, PDGFRß, NG2, and CD13, individually across all examined time points.

3.4 Molecular pathways underlying hypertension-induced vascular remodeling

To pinpoint the molecular basis of vascular remodeling in hypertension, we conducted an in-depth analysis of isolated microvessels using a custom PCR array focusing on genes within key pathways pivotal to understanding the vascular consequences of chronic hypertensive states—angiogenesis, BBB integrity, hypoxia, inflammation, and specific pericyte markers. This targeted analysis aimed to link transcriptional changes that accompany and possibly precipitate the vascular alterations seen in hypertension. Our results revealed the microvessel transcriptional landscape, pinpointing genes that undergo significant regulation in response to hypertensive stress. In the early chronic phase (Fig. 14b), a notable upregulation of n = 31 genes (fold change > 1.5, $p < 0.05$), including *Agtr1a, Epas1, Timp3, Tek, Notch3, Vegfb*, and *Mmp9*, displayed a state of heightened vascular reactivity and remodeling. Inflammatory vascular processes were displayed by the upregulation of *TNF, Icam1, Ccl2, Ccl5, IL10, Il1b, Ifng, Bdkrb1*, and *Nos2* (Fig. 14b). On the other hand, in late chronic HTN n = 35 genes were downregulated (Fig. 14c), demonstrating the progression from an active transcriptional response in the early state to a more subdued profile in late chronic HTN.

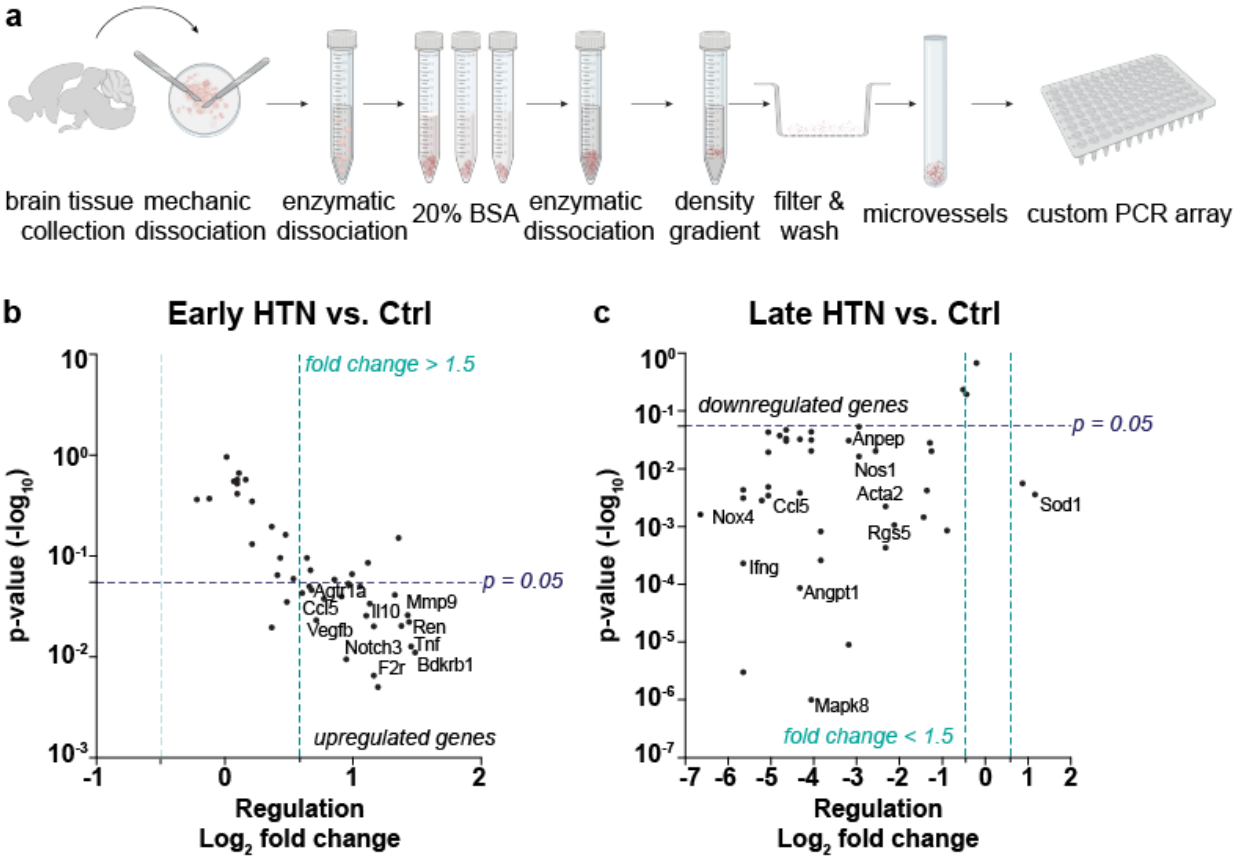

Fig. 14 Isolation of microvascular vessel fragments and gene expression analysis

(a) Schematic representation of the multi-step process used for isolating microvascular fragments from the brains of hypertensive and control rodents. Following microvessels isolation, RNA was extracted to perform a custom PCR array analysis targeting specific genes relevant to pericyte function and hypertensive pathology (b) Early chronic hypertension volcano plot displaying the differential gene expression between control and early chronic hypertensive cells. Each dot represents one gene. The vertical green dotted lines indicate the 1.5-fold change threshold beyond which gene expression differences are considered potentially biologically significant. The horizontal blue dotted line indicates the statistical significance threshold ($p < 0.05$) dividing genes with significant expression changes from those without. (c) Similar to panel b, late chronic hypertension volcano plot showing a notable predominance of gene downregulation. The same thresholds for fold change and significance were applied to aid in the identification of key regulatory genes affected by prolonged arterial hypertension. a, created in Biorender.com.

To examine these transcriptional shifts, we further dissected the expression patterns of each gene relative to their levels in the early HTN control group (Fig. 15). These analyzed genes were specifically selected for the custom PCR array because they represent key molecular pathways underlying hypertension-induced vascular remodeling. These pathways include hypertension/hypoxia (Fig. 15a), specific pericyte markers (Fig. 15b), angiogenesis/blood-brain barrier (Fig. 15c), and inflammation (Fig. 15d). This detailed gene expression analysis helps us understand the specific contributions of these pathways to the vascular remodeling observed in hypertensive conditions.

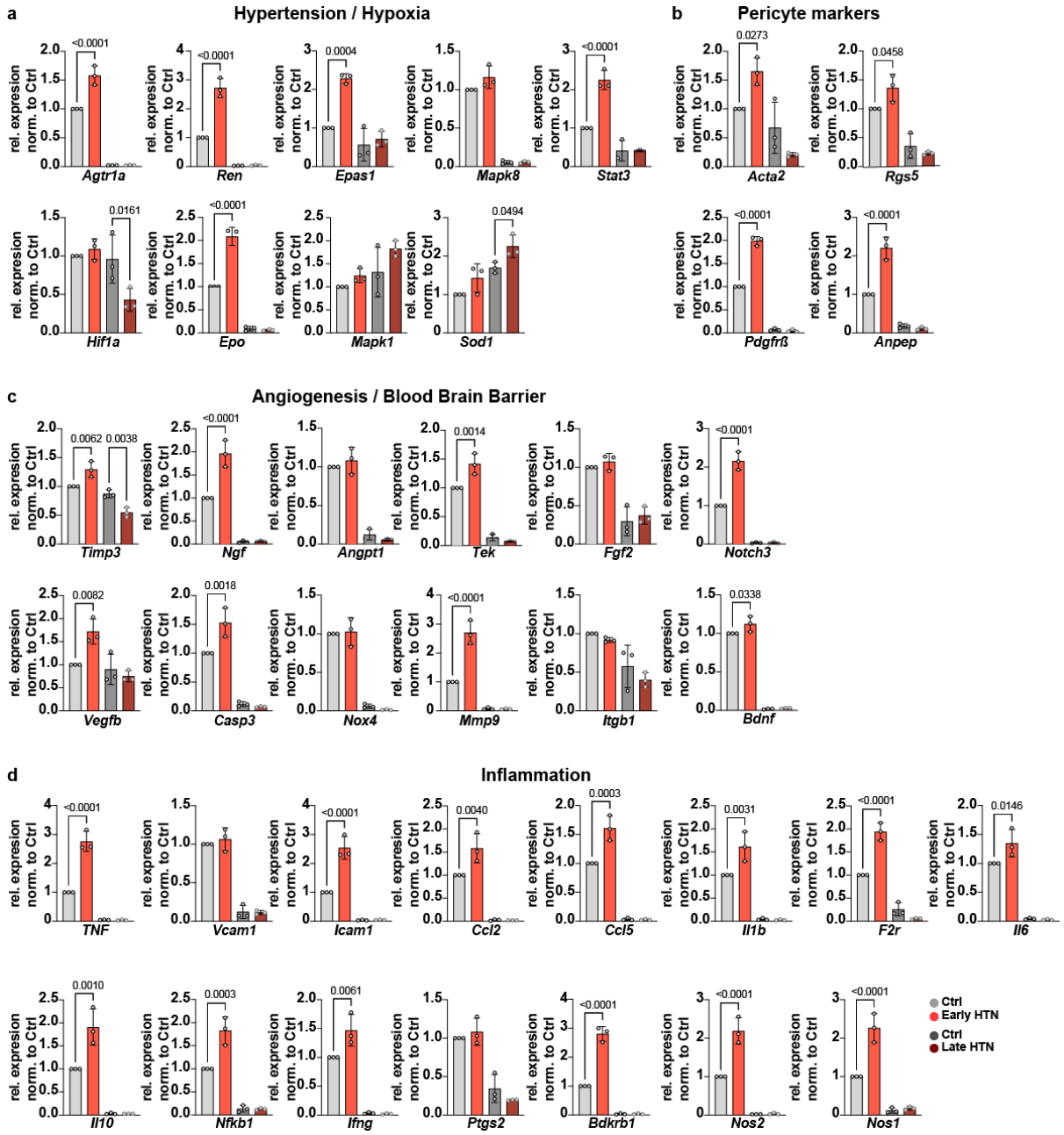

Fig. 15 Differential expression of genes involved in vascular remodeling across chronic hypertensive states

Bar charts comparing gene expression levels between early HTN and late HTN states alongside their respective controls. The genes analyzed are categorized into key molecular pathways implicated in hypertension-induced vascular remodeling: (a) Hypertension/Hypoxia, representative of the response to increased blood pressure and reduced oxygen levels, (b) Pericyte markers (c) Angiogenesis/Blood-Brain Barrier, representative of new blood vessel formation and the integrity of the BBB, (d) Inflammation, representing genes associated with inflammatory processes within the vascular system. Bar graphs represent mean ± s.e.m. calculated from 3 technical replicates. Each data point represents aggregate data derived from n = 5 biological samples. Relative gene expression levels were normalized to *Hprt* and further normalized to the average expression of early Ctrl. Exact *p*-values are displayed and statistical significance between hypertensive states and their respective controls was determined using one-way ANOVA with Holm-Sidak post hoc tests.

Next, we examined the biological pathways that were prominent in the observed transcriptional changes. Our findings revealed that early chronic hypertension is a phase marked by active vascular transformation, with upregulated genes indicating a substantial role of the vasculature in processes including blood flow regulation, lipid response, blood pressure control, angiogenesis, and inflammation (Fig. 16a). The late chronic HTN phase (Fig. 16b) revealed a decrease in the activity of pathways, which indicate a decline in the ability of blood vessels to adapt to high blood pressure, dysfunction in lipid metabolism, inflammation, and programmed cell death with potential failure to respond to the hypertensive challenge.

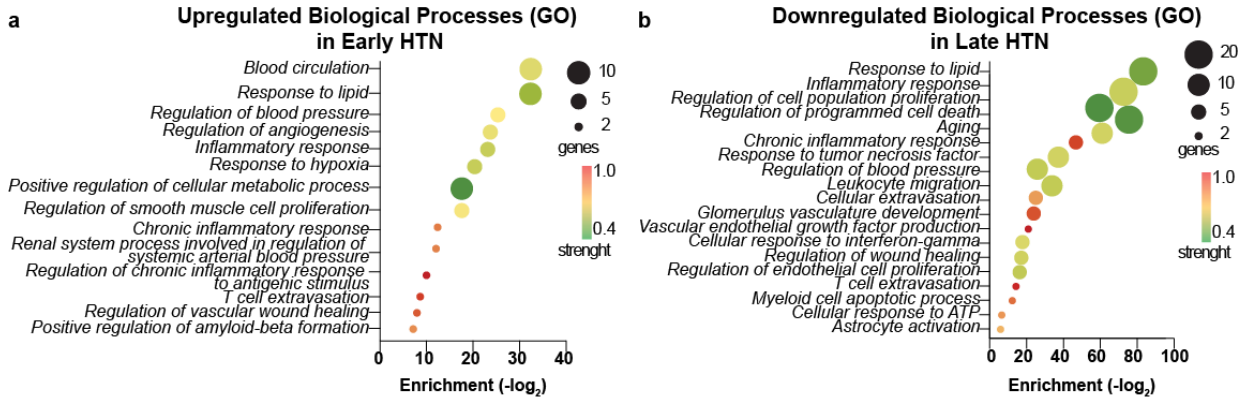

Fig. 16 Gene Ontology and reactome pathway analyses of microvessel transcriptional changes in chronic hypertension

Figure representing the results obtained after gene ontology analyses, to identify key biological processes influenced by chronic hypertension at different states. (a) Early chronic HTN plot displaying the upregulated biological processes related to blood circulation, lipid responses, angiogenesis, inflammatory responses, hypoxia, cellular metabolism, and vascular remodeling. The size of each dot represents the number of altered genes involved in the specific pathway. Color spectrum intensity indicates the strength of gene enrichment (log-transformed). (b) Late chronic HTN plot displaying downregulated processes including response to lipids, inflammation, programmed cell death, blood pressure regulation, and vascular endothelial growth factor production. Similar to a, dot size reflects the number of altered genes in the specific pathway, and color spectrum intensity represents enrichment strength.

3.5 *In vitro* pericyte expression dynamics mirror in vivo findings, showing hypertension-driven reductions in PDGFRß alongside elevations in NG2 and CD13

Following the characterization of vascular cell dynamics across chronic hypertensive states, we shifted our attention to a carefully controlled *in vitro* setting to gain a deeper understanding of the effects of hypertensive stress on pericyte behavior. Our *in vitro* approach began with the isolation of brain microvascular fragments (Fig. 17a), their seeding, expansion, and precise pericyte enrichment, free from endothelial cell influence (Fig. 17b)(148).

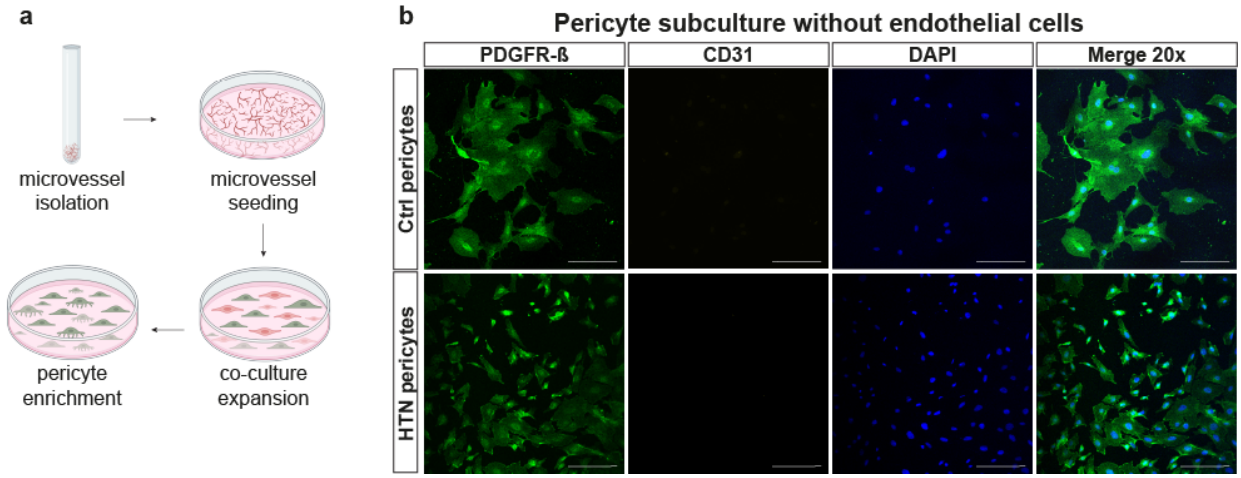

Fig. 17 Visualization of pericyte identity and purity by immunofluorescence

(a) Schematic representation of the experimental workflow showing the initial microvessel seeding, co-culture expansion of pericytes with endothelial cells and subsequent pericyte enrichment for the characterization of enriched pericytes through confocal microscopy and flow cytometric analysis. (b) Immunofluorescence images displaying pericyte cultures without endothelial cells, with each row depicting control and hypertensive pericytes. Columns depict the expression of PDGFRß, the absence of CD31, and DAPI-stained nuclei, with a 20x merged view. All scale bars represent 100 µm. a, created in Biorender.com.

Immunofluorescence analyses (Fig. 18) confirmed the specificity and integrity of our pericyte cultures through PDGFRß expression and paralleled the significant shifts observed in *ex vivo* pericyte marker expression in response to early chronic HTN. *In vitro*, pericytes derived from early chronic HTN displayed a marked upregulation of NG2 and CD13, alongside a reduction in PDGFRß expression (Fig. 18b). And pericytes derived from early chronic controls displayed expression of NG2 and slight expression of CD13, although these control pericytes did not lose PDGFRß expression (Fig. 18b). Flow cytometric analysis (Fig. 18c) provided an additional quantitative perspective on these phenotypic modifications, demonstrating significant changes in the expression pattern of PDGFRß. Ctrl pericytes predominantly exhibited a dichotomous expression profile, characterized by distinct populations with high and intermediate levels of PDGFRß. In contrast, HTN pericytes demonstrated a uniform expression profile skewed towards intermediate levels (Fig. 18d). Further resolution of these changes was achieved through t-distributed Stochastic Neighbor Embedding (tSNE) analysis, which facilitated a detailed examination of NG2 and CD13 marker expressions enabling MFI quantification for each marker (Fig. 18e, f). Moreover, quantification of the relative frequency of PDGFRß$^{+}$ pericytes co-expressing NG2 and CD13 revealed a significant increase in CD13 co-expression among hypertensive pericytes compared to controls (Fig. 18g) These data reinforced our characterization of the dynamic response of pericytes to hypertensive and environmental stress.

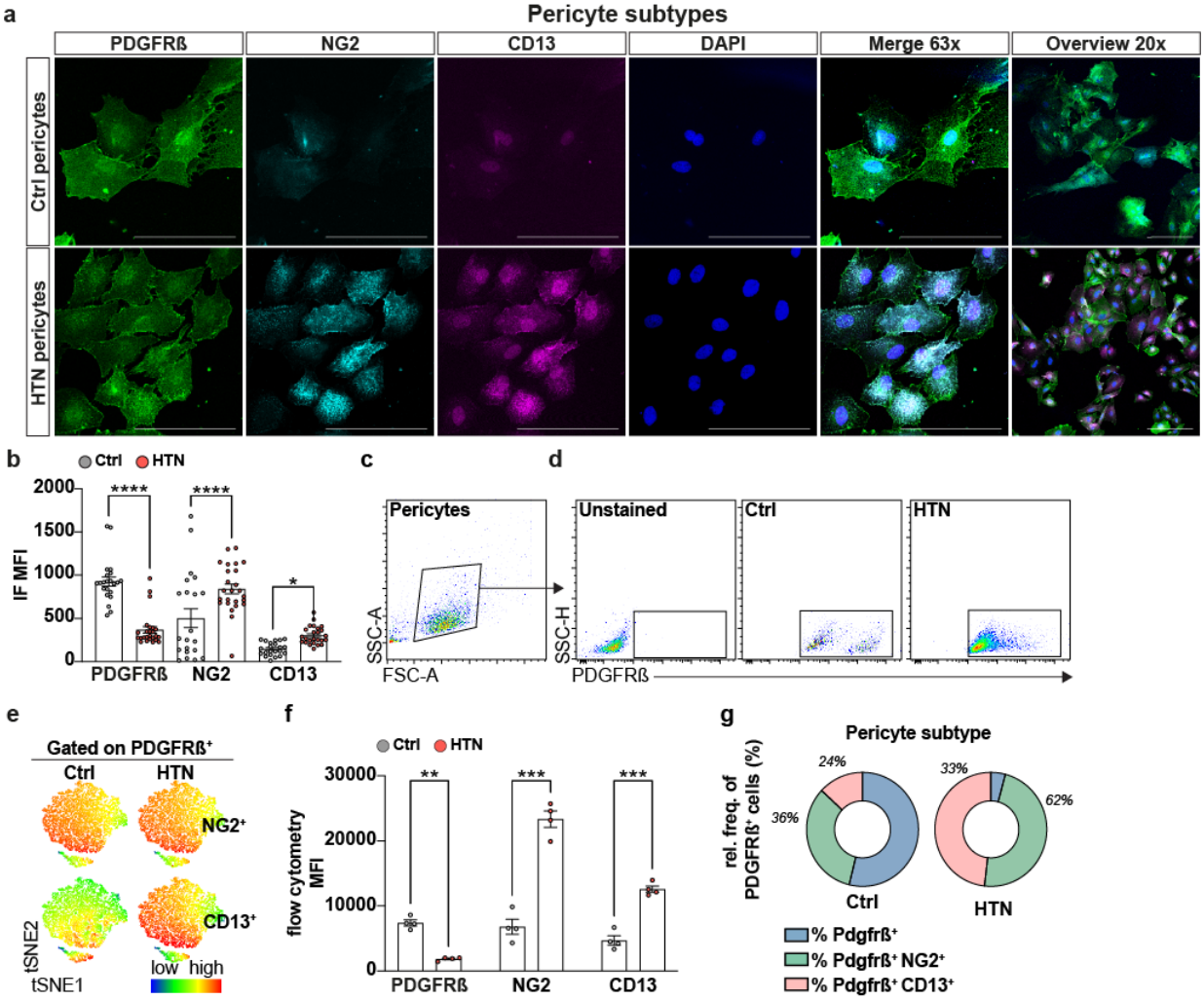

Fig. 18 Pericyte expression dynamics revealed a hypertension-driven reduction in PDGFRß and boost in CD13 expression

(a) Immunofluorescence imaging analysis for pericyte subtype identification in cultures, revealing differential expression of PDGFRß, NG2, and CD13 across control and hypertensive pericytes. Images show 63x high-resolution merges and a 20x overview of pericyte subtype distribution. (b) Quantitative analysis of mean fluorescence intensity (MFI) for PDGFRß, NG2, and CD13; each dot represents the average MFI measurements obtained per field of view. (c-f) Flow cytometric analysis and tSNE plots elaborating further on pericyte subtype characterization in vitro. Initial gating strategies are depicted to validate the expression of PDGFRß in all cells, followed by detailed analysis of NG2 and CD13 expression across pericyte populations using subsequent tSNE visualization and quantification; each dot represents the aggregate data of averaged duplicates derived from *in vitro* expansion that correspond to n = 10 biological samples per group. (g) Relative frequencies of PDGFRß$^{+}$ cells displaying subtype distinctions within control and hypertensive groups *in vitro* derived from flow cytometric data. Microvessel isolation and pericyte enrichment methodologies are detailed in Fig. 14a, Fig. 17a. Data are presented as mean ± s.e.m. $^{**}p < 0.01$, $^{***}p < 0.001$, $^{****}p < 0.0001$. All scale bars represent 100 µm.

3.6 Impact of hypertensive EVs on pericyte mitochondrial function

Expanding on our initial *in vitro* research on pericyte adaptation, we broadened our investigation to examine the impact of hypertensive stimuli on pericyte mitochondrial function at the mitochondrial level, as this is a crucial aspect of maintaining cellular health and vascular integrity during stressful conditions (171). Our methodology centered on isolating plasma and plasma-derived extracellular vesicles (pdEVs) (Fig. 19a) from early chronic hypertensive and age-matched control rodents, utilizing these biological materials to further stimulate normotensive control pericytes *in vitro*. This approach allowed us to directly examine the effects of hypertensive blood components on pericyte mitochondrial function, thereby providing a bridge between systemic hypertension and its vascular repercussions.

Flow cytometric analysis of pdEVs, with size gating and tetraspanin marker expression selection (CD9, CD63, and CD81), confirmed the presence of isolated pdEVs (Fig. 19b), revealing no difference in abundance of circulating pdEVs between early chronic HTN and age-matched Ctrl (Fig. 19c). Utilizing the JC-10 dye to assess mitochondrial membrane potential ($\Delta\Psi m$), our experiments revealed a significant impact of hypertensive pdEVs on Ctrl pericyte mitochondrial function (Fig. 19d). In healthy cells with an intact mitochondrial membrane potential ($\Delta\Psi m$), JC-10 aggregates in the mitochondria, emitting red fluorescence (Fig. 19d). However, when the mitochondrial $\Delta\Psi m$ is compromised, JC-10 fails to aggregate and remains in its monomeric form, emitting green fluorescence. Therefore, this dye provides a quantifiable measure of mitochondrial $\Delta\Psi m$ and overall health.

Contrary to the relatively stable $\Delta\Psi m$ observed in Ctrl pericytes exposed to normotensive plasma and pdEVs, hypertensive pdEVs induced a marked depolarization of the mitochondrial $\Delta\Psi m$ in control pericytes (Fig. 19e, f). Quantitative analysis of $\Delta\Psi m$ revealed the extent of mitochondrial dysfunction, with hypertensive pdEVs significantly reducing the JC-10 aggregate/monomer ratio, which translates to compromised mitochondria function (Fig. 19g).

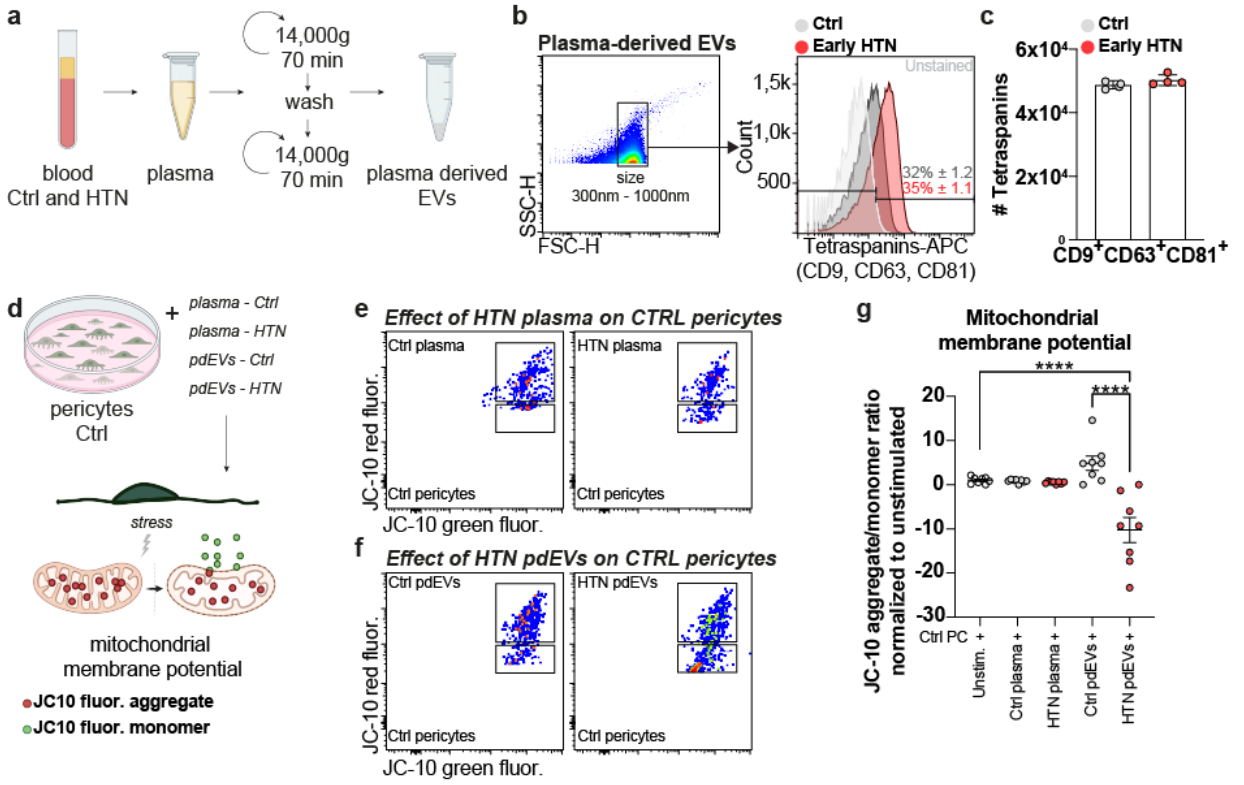

Fig. 19 Hypertensive-derived extracellular vesicles cause selective mitochondrial disruption in control pericytes

(a) Schematic representation of the experimental setup for isolating and enriching plasma-derived extracellular vesicles (pdEVs) from early chronic HTN and age-matched Ctrl rodents. (b) Flow cytometric analysis displaying EV selection based on size gates using 300-1000 nm silica beads, followed by histograms indicating the counts, frequencies, and positive selection of tetraspanins (CD9, CD63, and CD81). (c) Bar graphs comparing the absolute numbers of isolated pdEVs from Ctrl and HTN rodents. Each data point represents aggregate data of duplicates derived from one biological sample; experiment was conducted twice. (d) Depiction of *in vitro* stimulation conditions with Ctrl pericytes derived from 6w old rodents exposed to plasma or pdEVs derived from early chronic HTN and age-matched Ctrl illustrating the experimental approach using JC-10 staining to assess the impact of hypertensive circulating factors on pericyte mitochondrial function. (e) Flow cytometric plots showing JC-10 fluorescence in Ctrl pericytes stimulated with whole plasma from Ctrl or HTN. (f) Flow cytometric plots showing JC-10 fluorescence in Ctrl pericytes stimulated with pdEVs from Ctrl or HTN. (g) Dot plot graph representing the JC-10 aggregate/monomer ratio in Ctrl pericytes under the corresponding stimulation condition normalized to unstimulated pericytes. Each data point represents aggregate data derived from n=10 biological samples measured in duplicates; experiment was conducted twice. Data are presented as mean ± s.e.m. ****$p < 0.0001$. a, and d, created in Biorender.com.

3.7 Metabolic reprogramming of pericytes in hypertension-induced vascular cell dysfunction

After uncovering the disruptions to mitochondrial function caused by hypertensive stimuli, we conducted further research on the metabolic characteristics of pericytes derived from hypertensive conditions. We aimed to dissect their broader metabolic response to hypertension-induced stress to

capture the essence of their metabolic adaptability and resilience. Therefore, we conducted an extensive metabolic profile analysis that examined oxidative phosphorylation (OxPhos) and glycolysis in pericytes isolated from initial and chronic stages of hypertension (Fig. 20). This approach was predicated on the hypothesis that hypertension has distinct effects on pericyte metabolism throughout its progression, potentially revealing metabolic vulnerabilities or adaptations unique to hypertensive vascular pathology.

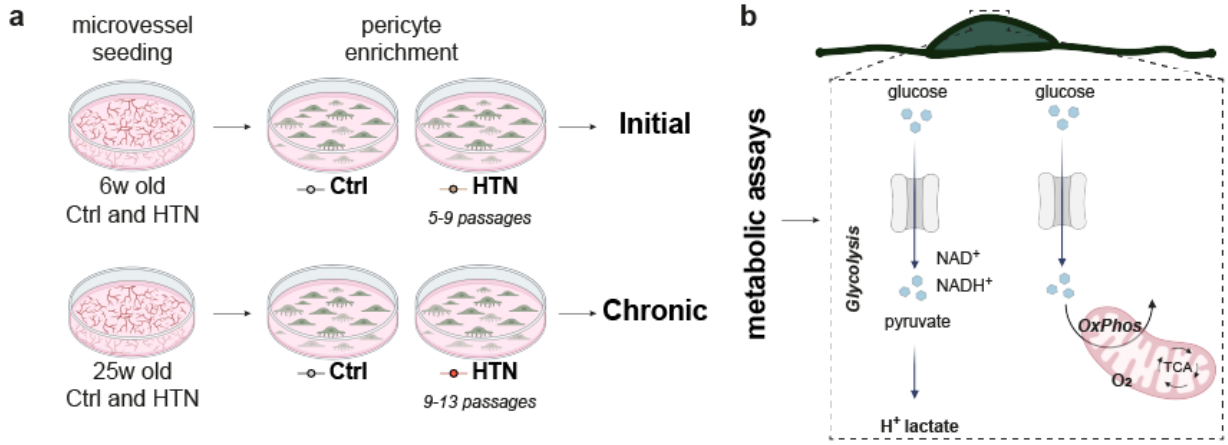

Fig. 20 Pericyte culture and metabolic assays overview

(a) Schematic representation of the process of isolating and culturing pericytes from microvessels derived from both control (Ctrl) and hypertensive (HTN) rodents at different HTN states. Microvessels from 6-week-old and 25-week-old Ctrl and HTN rodents were seeded and underwent several passages to enrich for pericyte populations. Pericyte cultures from 6-week-old rodents underwent metabolic experiments at passages 5, 7 and 9; while those from 25-week-old rodents underwent metabolic experiments at passages 9, 11, and 3, representing initial and chronic HTN states, respectively. (b) Schematic depiction of Oxidative Phosphorylation (OxPhos) and Glycolytic metabolic pathways to study pericyte metabolism under different conditions. This diagram illustrates the assessment of glucose metabolism through glycolysis (cytosol) and the tricarboxylic acid (TCA) cycle (within the mitochondria), including the conversion of glucose to pyruvate and subsequently to lactate or its entry into the TCA cycle. Key metabolites and co-enzymes such as NAD^+, NADH, together with the resultant production of ATP and lactate are also illustrated, which indicate the focus on mitochondrial functionality and overall cellular energy metabolism. Created in Biorender.com.

Oxygen Consumption Rate (OCR) and Extracellular Acidification Rate (ECAR) plots are essential tools for understanding cellular metabolic functions, particularly mitochondrial respiration and glycolysis, respectively (Fig. 21). The OCR plot (Fig. 21a) measures mitochondrial function by tracking various parameters over time, including basal respiration, ATP production, proton leak, spare respiratory capacity, and maximal respiration. Higher OCR values indicate greater mitochondrial activity and respiratory capacity. Specific inhibitors and uncouplers are sequentially added during the assay to isolate each parameter, providing a comprehensive profile of mitochondrial function. Conversely, the ECAR plot (Fig. 21b) is used to evaluate glycolytic

function by monitoring the production of lactate, which acidifies the extracellular environment. Here, key glycolytic parameters such as basal glycolysis, glycolytic reserve and glycolytic capacity are measured. These measurements are obtained by analyzing changes in ECAR following the sequential addition of metabolic inhibitors and stimulators, providing a detailed view of the glycolytic activity of the cell.

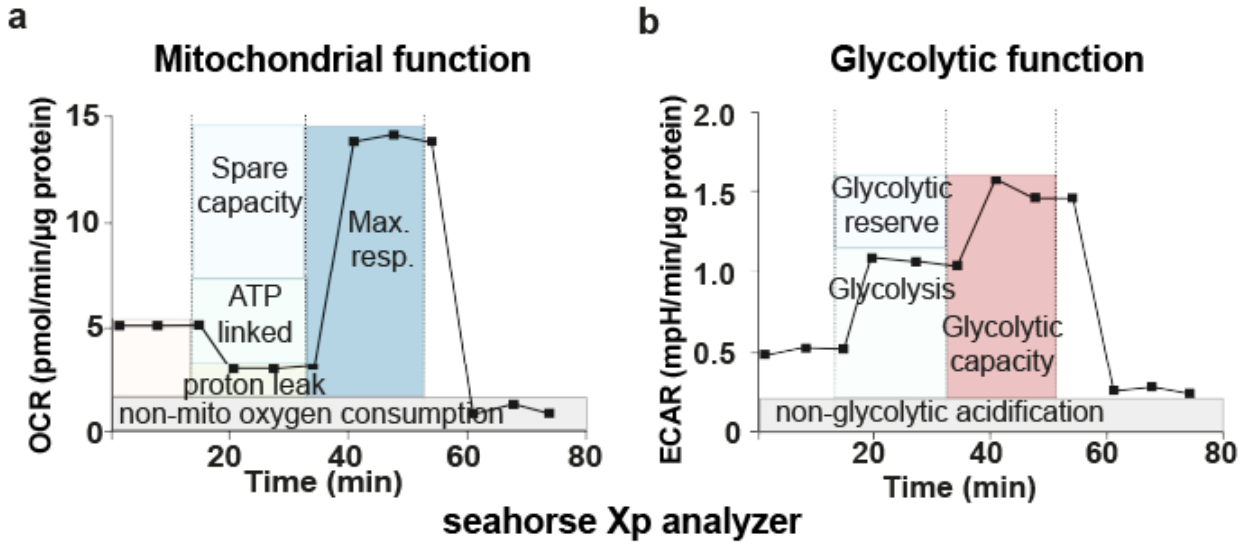

Fig. 21 Metabolic function assessment in cerebral pericytes using the Seahorse Xp Analyzer

(a) Mitochondrial function – the oxygen consumption rate (OCR) plot illustrates the different parameters of mitochondrial respiration in pericytes over time. Initially, basal respiration, ATP production, proton leak, and non-mitochondrial oxygen consumption are measured. The addition of specific inhibitors and uncouplers reveal the spare respiratory capacity and maximal respiration (Max. resp.), demonstrating the ability of the cell to respond to increased energy demands. (*Note*: Common uncouplers used include FCCP and CCCP.) (b) Glycolytic function – the extracellular acidification rate (ECAR) plot demonstrates the glycolytic activity of the cell studied. Basal glycolysis is measured initially, followed by the addition of metabolic modulators to assess glycolytic capacity and reserve. Additionally, non-glycolytic acidification is evaluated to guarantee accurate interpretation of glycolytic flux. Created in Biorender.com.

The OCR traces reveal a clear difference between Ctrl and HTN pericytes (Fig. 22a). During the initial HTN phase, HTN pericytes exhibit a lower OCR compared to controls, which becomes even more apparent when following the addition of the uncoupler FCCP, revealing their maximal respiratory capacity. This decrease is even more pronounced in the chronic HTN phase, which evidences a continuous decline in mitochondrial due to prolonged hypertension (Fig. 22b). Moreover, evaluation of the spare respiratory capacity, which assesses the potential of cells to respond to bioenergetic stress, showed a significant decrease in chronic HTN (Fig. 22b). The assessment of ATP linked to mitochondrial activity showed a significant decrease in ATP production in pericytes from chronic HTN as compared to both their initial hypertensive counterparts and age-matched controls. This decrease indicates a reduced efficiency of the

mitochondria and illustrates a changing energy landscape, where the dependence on ATP synthesis by mitochondria decreases in the presence of hypertensive states. Lastly, the notable reduction in non-mitochondrial oxygen consumption rates in chronic HTN pericytes indicate that the metabolic decline extends beyond mitochondrial function and shows a broader impairment in cellular respiration (Fig. 22b).

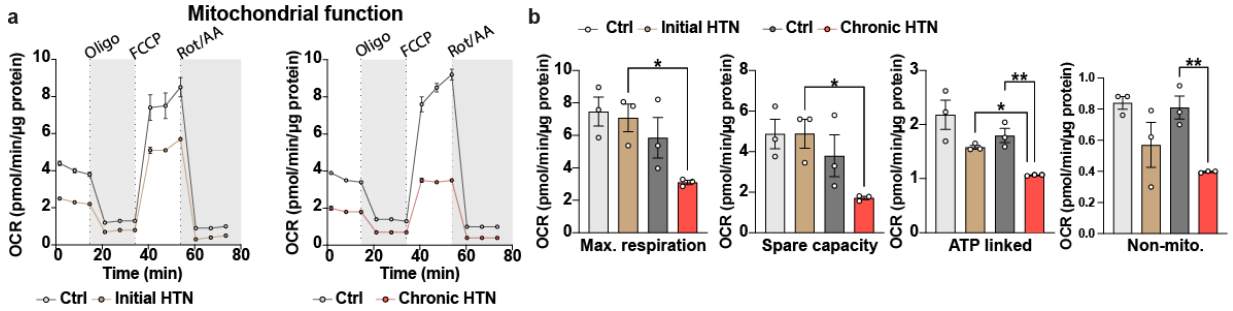

Fig. 22 Hypertension induces significant impairment in mitochondrial function of pericytes

(a) The oxygen consumption rate (OCR) of pericytes isolated from control (Ctrl) and hypertensive (HTN) rodents was measured using the Seahorse Xp Analyzer to assess mitochondrial respiration over time. The plots illustrate the distinct phases of mitochondrial function, including basal respiration, ATP-linked respiration, proton leak, spare respiratory capacity and maximal respiration, for both the initial and chronic stages of HTN. Dotted lines indicate the period and time of oligomycin (Oligo), carbonyl cyanide-p-trifluoromethoxyphenylhydrazone (FCCP), rotenone (ROT), and antimycin (Ant) treatment. The sequential addition of Oligo, FCCP, and Rot/AA was used to induce the different phases. (b) Bar graphs represent the quantification of essential mitochondrial parameters derived from the OCR traces. These parameters include maximal respiration, spare capacity, ATP-linked respiration, and non-mitochondrial oxygen consumption. The values of these parameters are compared between control and hypertensive pericytes at both the initial and chronic stages of hypertension. Data are presented as mean ± s.e.m. of three independent experiments per group per time point, with each experiment including triplicates. Each data point represent aggregate data from initial groups (Ctrl and HTN) derived from n = 8 biological samples each, and chronic groups (Ctrl and HTN) from n=10 biological samples each. Statistical significance is indicated by $*p < 0.05$ and $**p < 0.01$.

Following the sequential additions of glucose, oligomycin (Oligo), and 2-deoxyglucose (2-DG), we analyzed the extracellular acidification rate (ECAR) over time to observe the fluctuating patterns of glycolysis in pericytes (Fig. 23a). Both initial and chronic HTN pericytes exhibited significantly higher ECAR levels compare to controls, indicating a significant elevated glycolytic activity (Fig. 23b). This enhanced glycolysis in HTN pericytes is particularly evident after the addition of glucose and oligomycin, which stimulate the glycolytic pathway. The glycolytic capacity (Fig. 23b), reflecting the maximum rate of glycolysis under stressed conditions, was significantly higher in hypertensive pericytes across both stages, emphasizing enhanced glycolytic dependence as a key feature of pericyte metabolic adaptation to hypertension. Interestingly, the glycolytic reserve (Fig. 23b), which reflect the extent to which cells can further increase glycolysis from their baseline level, showed a significant increase in initial hypertensive pericytes compared

to controls. Notably, non-glycolytic acidification remains largely unchanged, indicating that the observed differences are specific to the glycolytic pathway.

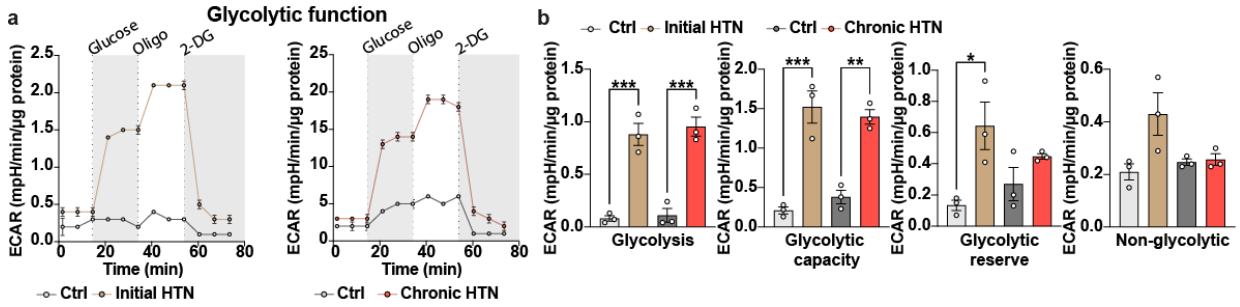

Fig. 23 Arterial hypertension induces metabolic reprogramming in pericytes toward glycolytic reliance for energy production

(a) The extracellular acidification rate (ECAR) of pericytes isolated from control (Ctrl) and hypertensive (HTN) rodents was measured using the Seahorse Xp Analyzer to assess glycolytic activity over time. Dot lines indicate the period and time of glucose, oligomycin (Oligo), and 2-Deoxy-D –glucose (2-DG) addition. Distinct phases of glycolytic function including glycolysis, glycolytic capacity, and glycolytic reserve are shown for both groups at the initial and chronic stages of hypertension. (b) Bar graphs depicting glycolytic capacity, glycolytic reserve, and non-glycolytic ATP production. Bar graphs represent the quantification of essential glycolytic parameters derived from the ECAR traces. Glycolysis, glycolytic capacity, glycolytic reserve, and non-glycolytic acidification are compared between Ctrl and HTN pericytes at both initial and chronic stages of hypertension. Data are presented as mean ± s.e.m. of three independent experiments per group per time point, with each experiment including triplicates. Each data point represent aggregate data from initial groups (Ctrl and HTN) derived from n = 8 biological samples each, and chronic groups (Ctrl and HTN) from n = 10 biological samples each. Statistical significance is indicated by $*p < 0.05$, $**p < 0.01$, and $***p < 0.001$.

In order to investigate the impact of hypertension on the energetic health and ATP production profile of pericytes, the evaluation of the bioenergetic health index (BHI) was performed. This is a ratio that reflects the overall cellular energy capacity derived from both mitochondrial and glycolytic contributions. In chronic HTN pericytes, the BHI was significantly reduced compared to controls (Fig. 24a), evidencing a decline in overall bioenergetic health under chronic hypertensive conditions. Expanding on the OxPhos and glycolysis measurements, we performed an ATP profile to distinguish between mitochondrial ATP and glycolytic ATP. Our results revealed a striking shift in ATP production already at initial HTN (Fig. 24b). Initial hypertensive pericytes differed significantly from their control counterparts by generating a substantial portion of their ATP through glycolysis, as opposed to control pericytes (49 % vs. 11 %). This striking shift persisted in chronic HTN (50 % vs. 8 %). These results evidence a substantial metabolic reprogramming in HTN pericytes, favoring glycolysis over mitochondrial OxPhos as the primary source of ATP production.

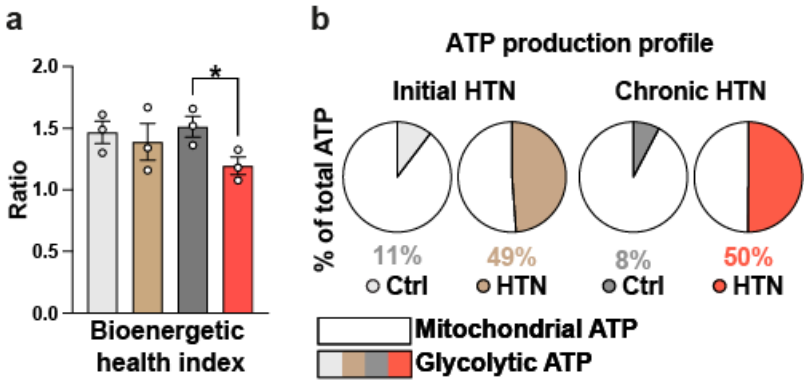

Fig. 24 Hypertension induces bioenergetic impairment and reprogramming in ATP production toward glycolysis in pericytes

(a) Bar graphs representing the Bioenergetic health index as a dynamic measurement of pericyte response to stress at initial and chronic HTN. (b) Pie charts illustrating the percentage of total ATP derived from mitochondrial OxPhos vs. glycolysis in Ctrl and HTN pericytes at initial and chronic HTN. Data are presented as mean ± s.e.m. of three independent experiments per group per time point, with each experiment including triplicates. Each data point represent aggregate data from initial groups (Ctrl and HTN) derived from n = 8 biological samples each, and chronic groups (Ctrl and HTN) from n = 10 biological samples each. Statistical significance is indicated by $*p < 0.05$.

The assessment of metabolic potential under stress conditions validated the influence of hypertension on pericyte energy dynamics (Fig. 25). Our results reveal that at initial HTN stressed OCR levels are similar between groups, while ECAR levels in HTN showed significant lower levels than Ctrl (Fig. 25a). At chronic HTN both OCR and ECAR levels are significantly reduced in chronic HTN pericytes compared to Ctrl (Fig. 25a). These results evidence that HTN pericytes, particularly in the chronic HTN, possess a diminished metabolic flexibility and capacity to meet increased energy demands.

The energetic map illustrates mitochondrial ATP production rate against glycolytic ATP production rate for pericytes under different conditions (Fig. 25b). This map classifies cells into four metabolic categories: aerobic, energetic, glycolytic, and lower energetic. The majority of Ctrl pericytes occupy primarily the aerobic and energetic zones indicating efficient and balanced energy production (Fig. 25b). However, in initial HTN pericytes, there is a shift towards a more glycolytic profile, and chronic HTN pericytes cluster in the lower energetic and glycolytic zones. This evidences their impaired mitochondrial function and increased dependence on glycolysis.

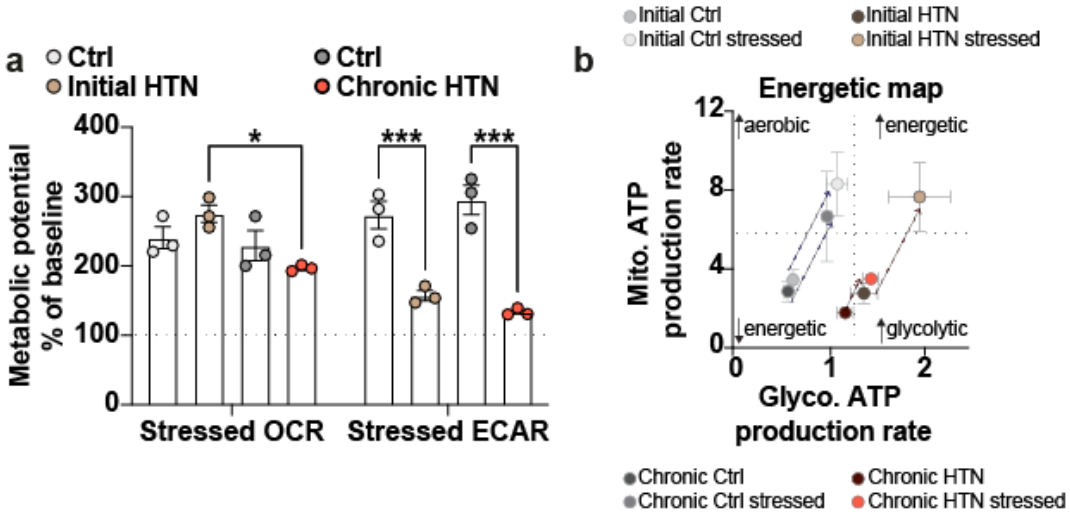

Fig. 25 Metabolic potential and energetic profile of pericytes under stressed conditions

(a) Bar graphs representing the stressed oxygen consumption rate (OCR) and extracellular acidification rate (ECAR) as a percentage of baseline in control (Ctrl) and hypertensive (HTN) pericytes at initial and chronic stages of hypertension. (b) Plot of mitochondrial ATP production rate vs. glycolytic ATP production rate, which categorizes pericytes into four metabolic states: aerobic, energetic, glycolytic, and lower energetic. Bar graphs represent mean ± s.e.m. of three independent experiments per group per time point, with each experiment including triplicates. Each data point represent aggregate data from initial groups (Ctrl and HTN) derived from n = 8 biological samples each, and chronic groups (Ctrl and HTN) from n = 10 biological samples each. Data are presented as mean ± s.e.m. *$p < 0.05$, and ***$p < 0.001$.

3.8 Metabolic inhibition highlights energetic vulnerabilities in hypertensive pericytes

To elucidate the metabolic requirements of pericytes in hypertensive conditions, we employed specific metabolic inhibitors that target key pathways involved in mitochondrial OxPhos and glycolysis (Fig. 26). As depicted in Fig. 26a, we utilized UK5099 to inhibit the mitochondrial pyruvate carrier, etomoxir, to block fatty acid oxidation by suppressing carnitine palmitoyltransferase 1 (CPT1), and BPTES to inhibit glutaminase, thereby disrupting glutamine metabolism. These inhibitors collectively impair the ability of the cell to utilize pyruvate, fatty acids, and glutamine for mitochondrial ATP production. This experimental setup resulted in a decrease OCR in both Ctrl and HTN pericytes (Fig. 26c, d), which indicated a successful mitochondrial pathway inhibition.

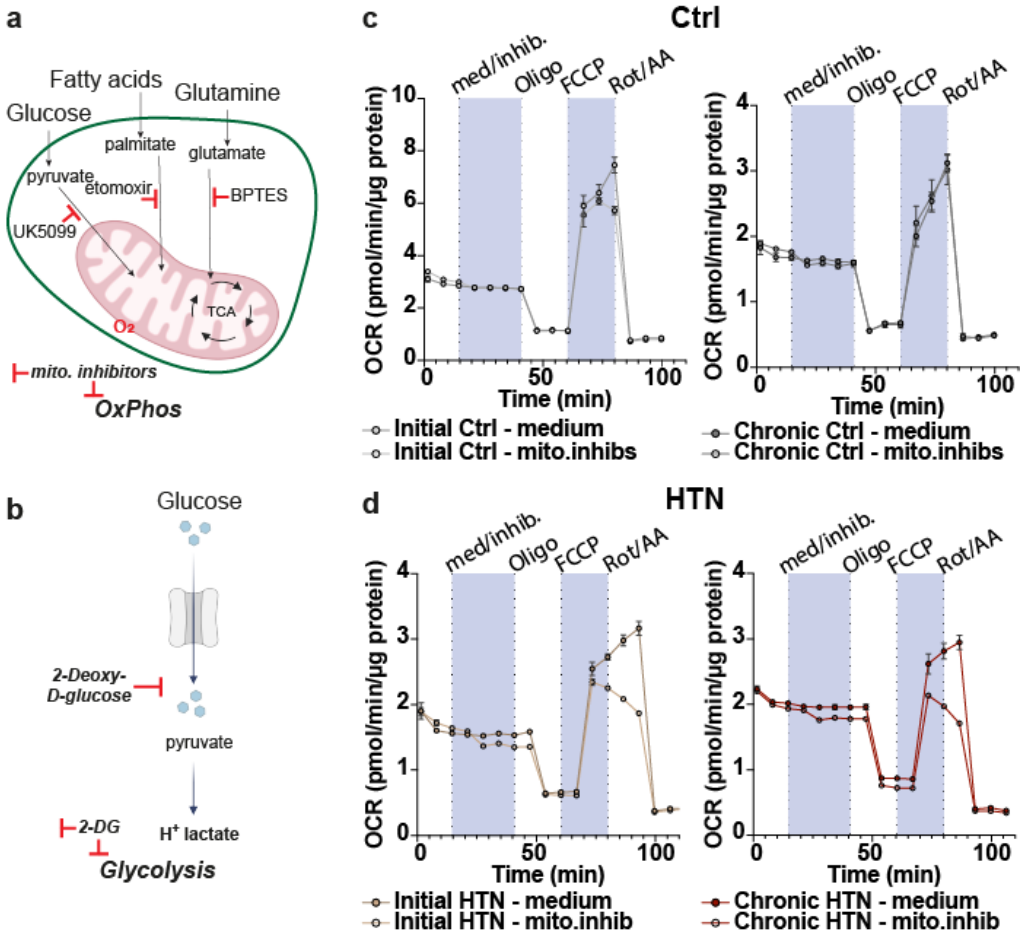

Fig. 26 Metabolic pathways inhibition in control and hypertensive pericytes

(a) Schematic representation of the application of metabolic inhibitors used to target pericyte mitochondrial pathways. UK5099 inhibits the mitochondrial pyruvate carrier, etomoxir blocks fatty acid oxidation, and BPTES inhibits glutaminase, thereby disrupting glutamine metabolism. (b) Schematic representation of glycolysis inhibition using 2-deoxy-glucose (2-DG) to block hexokinase, which impedes glucose metabolism and reduces ATP production. (c) Oxygen consumption rate (OCR) plot of initial and chronic control (Ctrl) pericytes measured over time in the presence (med/inhib.) and absence (medium) of mitochondrial inhibitors. The addition of oligomycin (Oligo), FCCP, and rotenone/antimycin A (Rot/AA) illustrates the impact of mitochondrial pathway inhibition on OCR. (d) Similar to panel (c), but for initial and chronic hypertensive (HTN) pericytes. The OCR traces demonstrate the effect of mitochondrial inhibitors in the already compromised mitochondrial function in HTN pericytes. b, created in Biorender.com.

Our results revealed that under normal conditions, initial and chronic Ctrl pericytes exhibit a robust mitochondrial function, characterized by high levels of basal respiration, spare respiratory capacity, ATP-related respiration, and maximal respiration. However, upon treatment with mitochondrial inhibitors, these parameters significantly decline (Fig. 27a). Basal respiration and spare respiratory capacity were significantly reduced, thus indicating an effective inhibition of mitochondrial pathways (Fig. 27a). The decline in max. respiration further confirmed the dependency of Ctrl pericytes on mitochondrial OxPhos for ATP production (Fig. 27a).

Initial HTN pericytes displayed reduced levels of basal respiration, spare respiratory capacity, ATP-related respiration, and max. respiration compared to Ctrl pericytes, thereby evidencing inherent mitochondrial dysfunction (Fig. 26d). Upon treatment with mitochondrial inhibitors, both initial and chronic HTN pericytes demonstrate a significant decrease spare respiratory capacity and maximal respiration that indicate effective inhibition of mitochondrial pathways (Fig. 27b). Interestingly, proton leak was significantly reduced in chronic HTN pericytes upon mitochondrial inhibition, which evidences an altered mitochondrial membrane integrity and reduced mitochondrial uncoupling (Fig. 27b).

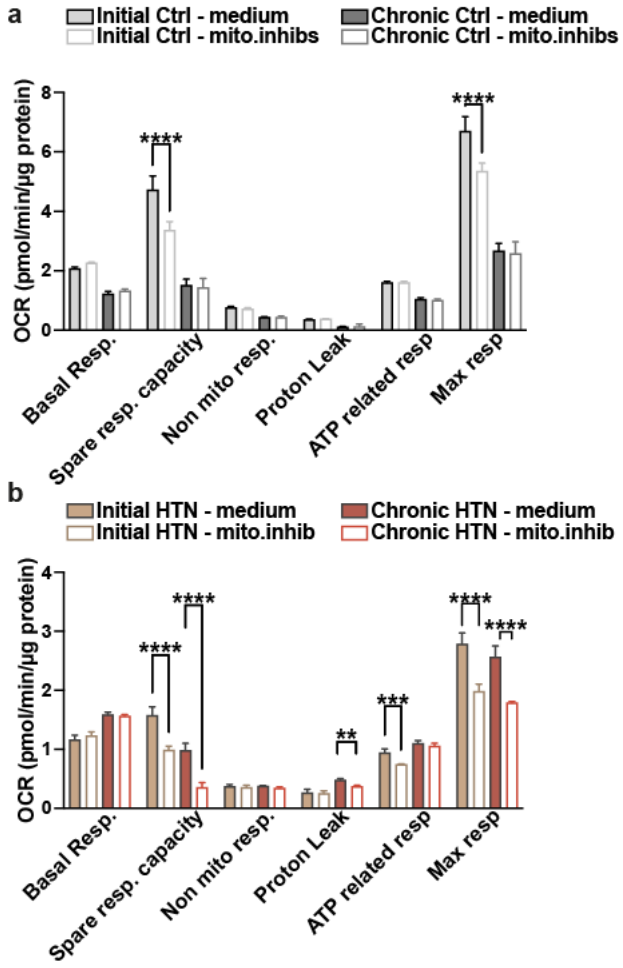

Fig. 27 Effect of mitochondrial inhibitors on mitochondrial respiration in Ctrl and HTN pericytes

(a) Bar graphs representing OCR parameters of mitochondrial respiration in Ctrl pericytes in the presence (mito.inhibitors) and absence (cell medium) of mitochondrial inhibitors (b) Similar to a, bar graphs representing OCR parameters of mitochondrial respiration in HTN pericytes in presence and absence of mitochondrial inhibitors. Measurements were performed in triplicate for each group at each time point. Bar graphs represent means ± s.e.m., with initial groups (Ctrl and HTN) derived from n = 8 biological samples each, and chronic groups (Ctrl and HTN) from n = 10 each. Data are presented as mean ± s.e.m, $^{**}p < 0.01$, $^{***}p < 0.001$, and $^{****}p < 0.0001$.

Further delving into the metabolic profile of pericytes, Ctrl pericytes continuously displayed a strong preference for mitochondrial ATP as their primary ATP production pathway (Fig. 28a, b). Upon exposure to mitochondrial inhibitors, Ctrl pericytes significantly increase glycolysis as evidence by the rise in glycolytic ATP production (Fig. 28a, b). This response reflects the ability of Ctrl pericytes to adapt rapidly to bioenergetic stressors altering their energy production from mitochondrial OxPhos to glycolysis.

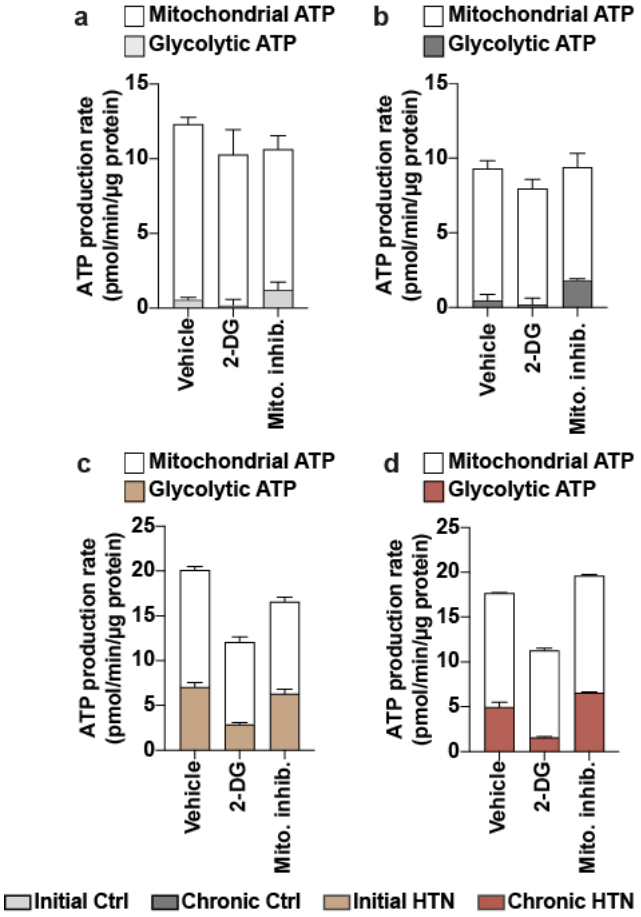

Fig. 28 Effect of metabolic inhibitors on ATP production in Ctrl and HTN pericytes

Bar graphs representing the ATP production rate (pmol/min/µg protein) derived from mitochondrial OxPhos and glycolytic pathways in (a) initial Ctrl, and (b) late Ctrl, showing a predominant dependence on mitochondrial ATP (c) Bar graphs representing ATP production rate in initial HTN, and (d) late HTN pericytes demonstrating a continued preference for glycolysis. Pericytes were treated with vehicle (medium), 2-deoxy-D-glucose (2-DG), and mitochondrial inhibitors (Mito. inhibs). Measurements were performed in triplicate for each group at each time point, with initial groups (Ctrl and HTN) derived from n = 8 biological samples each, and chronic groups (Ctrl and HTN) from n = 10 each.

Considering that hypertensive pericytes rely on glycolysis as their primary energy source, we sought to reduce their primary energy production pathway using 2-DG, a glycolysis inhibitor. In HTN pericytes, there is a marked dependence on glycolysis for ATP production, even before the use of mitochondrial inhibitors (Fig. 28c, d). The application of 2-deoxy-D-glucose resulted in a significant metabolic challenge, evidenced by a significant decrease in total ATP production. Although these cells display the potential to shift towards OxPhos, the transition was not fully compensated for the glycolytic blockade. When glycolysis was inhibited, chronic HTN pericytes experienced a substantial reduction in both glycolytic and mitochondrial ATP production, revealing a fixed metabolic programming that heavily favors glycolysis despite the potential availability of mitochondrial pathways.

4 Results

Microglial response under hypertensive stress

Microglia are found closely opposed to the outer vascular wall of parenchymal blood vessels. The focus of this chapter is to characterize the phenotypical microglial features in the non-transgenic Spontaneously Hypertensive Stroke-Prone Rat (SHRSP), and in human post-mortem brain tissue of elderly subjects with cSVD. Continuing from the vascular alterations observed in cerebral pericytes under chronic hypertensive stress, this section presents additional evidence of microvascular pathology, BBB disruption, immune cell infiltration and microglia profile in the context of chronic arterial hypertension.

4.1 Microvascular pathology and immune cell infiltration in hypertension-induced BBB disruption

To provide a clearer understanding of the temporal dynamics of BBB integrity and its association with microglial responses in chronic HTN, we examined isolated microvascular fragments (Fig. 29).

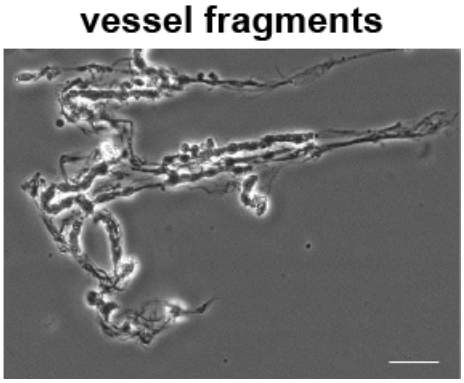

Fig. 29 Isolation and visualization of microvascular vessel fragments from rodent brain tissue

Representative image of isolated microvascular vessel fragments from rodent brain tissue. Vessel fragments were obtained to investigate the structural integrity and molecular composition of microvessels in the context of hypertension-induced BBB disruption. Phase-contrast image of isolated microvessel derived from brain cortices plated on a microscope slide (scale bar, 50 µm).

Our results showed a significant decrease in the expression of key tight junction proteins, claudin-5 (*Cldn5*) and occludin (*Ocln*), during the early chronic HTN (Fig. 30a). This decrease evidenced an impaired BBB integrity as an early sign of chronic arterial HTN. However, in the late chronic HTN, BBB permeability seemed to remain unchanged (Fig. 30a). Moreover, we found that the expression of vascular cell adhesion molecule-1 (*Vcam1*) and intercellular adhesion molecule-1 (*Icam1*) increased with age (Fig. 30b). Due to the decrease in tight junction molecules in early chronic HTN and the increase in adhesion molecules in late chronic HTN, we hypothesized that leukocytes were being recruited. We observed a substantial increase in leukocyte infiltration in both the cortex and hippocampus during early chronic HTN, which correlated with the

downregulation of tight junction proteins (Fig. 31). This finding confirmed that hypertension-induced BBB disruption facilitates the entry of leukocytes, a process that may be further exacerbated by aging and suggested the presence of a neuroinflammatory response.

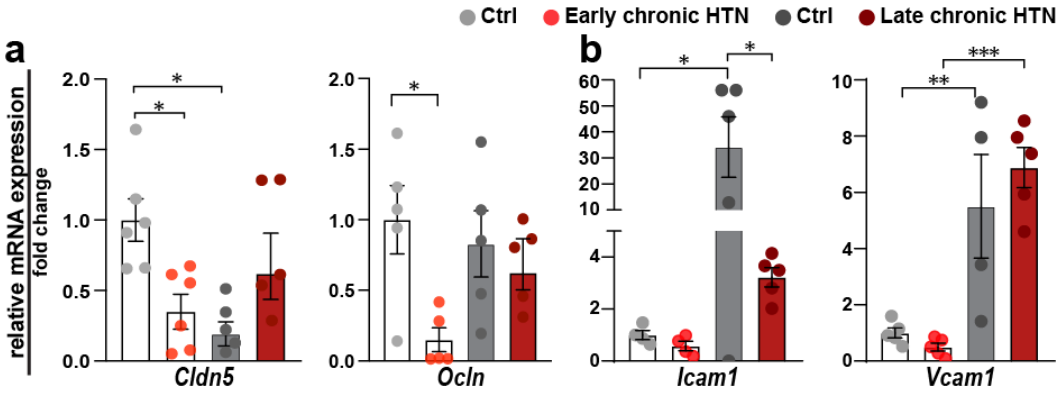

Fig. 30 Differential mRNA expression of tight junction and adhesion molecules in early and late chronic HTN

Relative mRNA expression levels of tight junction proteins and adhesion molecules in microvessels isolated from Ctrl and HTN brain tissues. (a) Expression of claudin-5 (*Cldn5*) and occludin (*Ocln)*. (b) Expression of intercellular adhesion molecule 1 (*Icam1*) and vascular cell adhesion molecule 1 (*Vcam1*). Fold changes were calculated by normalizing gene expression levels to GAPDH. The resulting data were further normalized on mean values of normotensive controls. Data are presented as mean ± s.e.m. For statistical significance: *$p < 0.05$, **$p < 0.01$, ***$p < 0.001$.

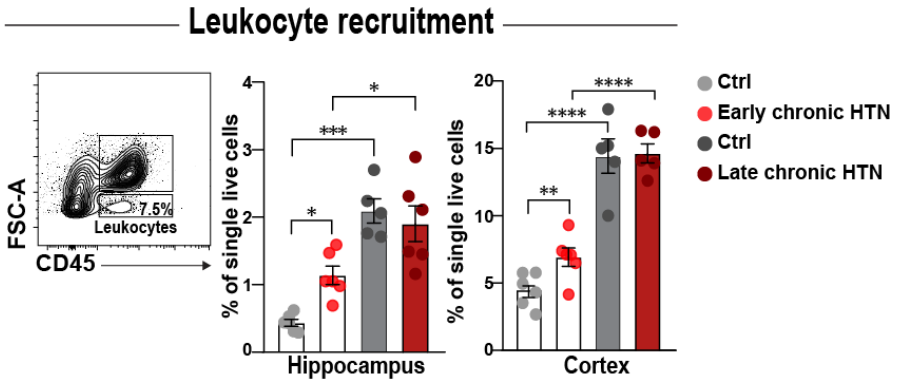

Fig. 31 Increased leukocyte recruitment in hippocampus and cortex during early and late chronic HTN

Flow cytometric analysis displaying the recruitment of leukocytes in the hippocampus and cortex during early and late chronic HTN. Representative flow cytometry plot identifying leukocytes represented as the frequency of low FSC-A vs. $CD45^+$ events from total single live cells (see Fig. 35 for full gating strategy). Quantification of leukocyte recruitment in the hippocampus and cortex, displayed as the percentage of single live cells. Data are presented as mean ± s.e.m., with statistical significance indicated as *$p < 0.05$, **$p < 0.01$, ***$p < 0.001$, ****$p < 0.0001$.

Therefore, to further explore the role that microglia play in this context, we investigated vascular-associated microglia (VAMs) in the hippocampus and cortex of SHRSP during early and late chronic HTN (Fig. 32). Our findings revealed an increased prevalence of VAMs in both the HTN hippocampus and HTN cortex in early and late chronic HTN, which evidenced the potential impact of microglia on BBB function and neuroinflammation.

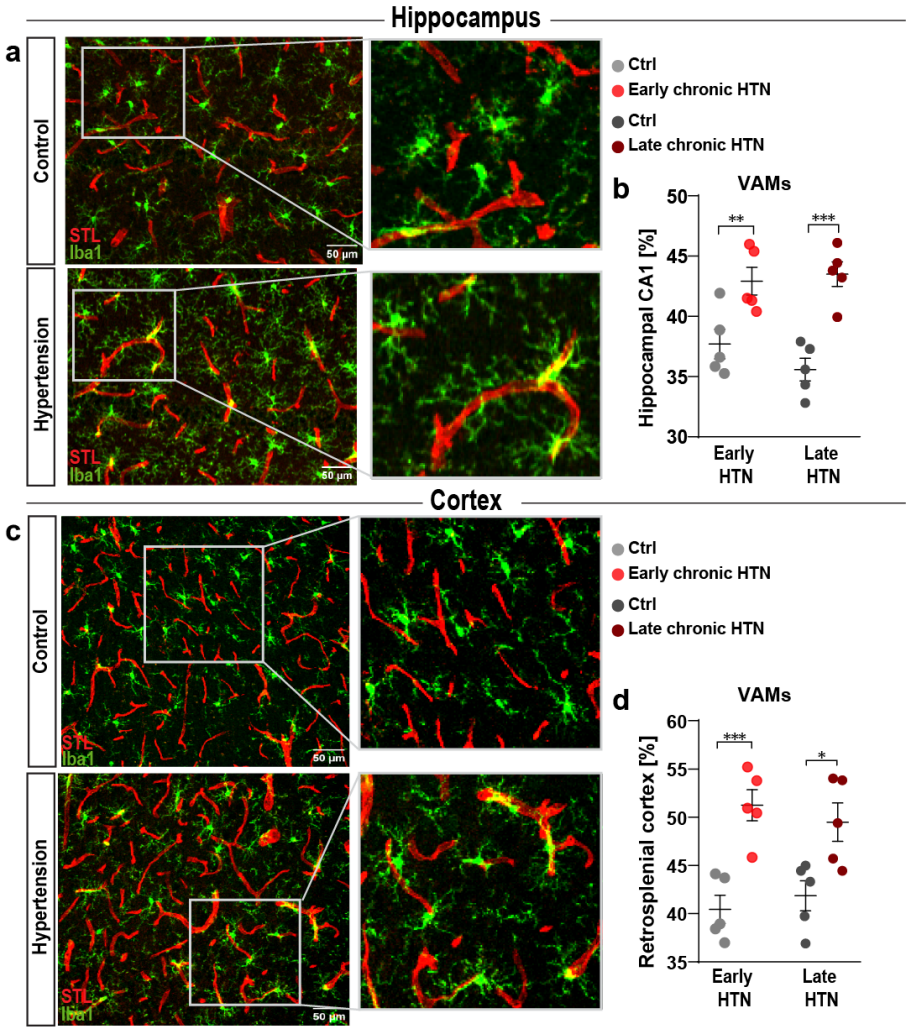

Fig. 32 Increased Vascular-Associated Microglia in Hippocampus and cortex during early and late chronic HTN

(a, c) Representative immunofluorescence image showing vascular-associated microglia (VAMs) in the hippocampal CA1 region and retrosplenial cortex of age-matched Ctrl and HTN rodents. VAMs are identified by IBA1 and STL stainings. The enlarged insets highlight the VAMs closely associated to the vasculature. Scale bar: 50 µm. (b, d) Frequency of VAMs in the respective region presented as a percentage of the total microglia population. Z-stack images were acquired taken from 10 fields of view per animal per region. Each dot represents average aggregate data of all FOVs. Data are presented as mean ± s.e.m., with statistical significance indicated as $*p < 0.05$, $**p < 0.01$, and $***p < 0.001$. IBA1, ionized calcium-binding adapter molecule 1 (microglial marker); STL, solanum tuberosum lectin-fluorescein isothiocyanate (endothelial marker).

4.2 Microglial morphological changes in hypertensive cSVD

Given the rise in VAMs in HTN brains within both the hippocampus and cortex, we aimed to investigate microglial morphology, as it reflects to certain extent the level of microglial reactivity. To this end, we conducted targeted IBA1 microglial IF staining on coronal brain slices. We then acquired high-resolution confocal images from the hippocampal CA1 region (Fig. 33a) and retrosplenial cortex (Fig. 34a), followed by single-cell morphology analysis using 3D reconstruction and skeleton analysis (Fig. 33b, Fig. 34b). In the hippocampus of the SHRSP model, we observed significant morphological changes in microglia in response to HTN. High-resolution confocal images and 3D reconstructions revealed an increase in somatic area in microglia from HTN rodents compared to controls (Fig. 33c). These changes were evident in both early and late chronic HTN. Additionally, the number of endpoints, which reflects the complexity of microglial processes, was significantly higher in late HTN (Fig. 33d). Furthermore, the maximum branch length (Fig. 33e) increased in late HTN and the 3D ramification index (Fig. 33f) was reduced, evidencing an enhancement in branching complexity within HTN microglia.

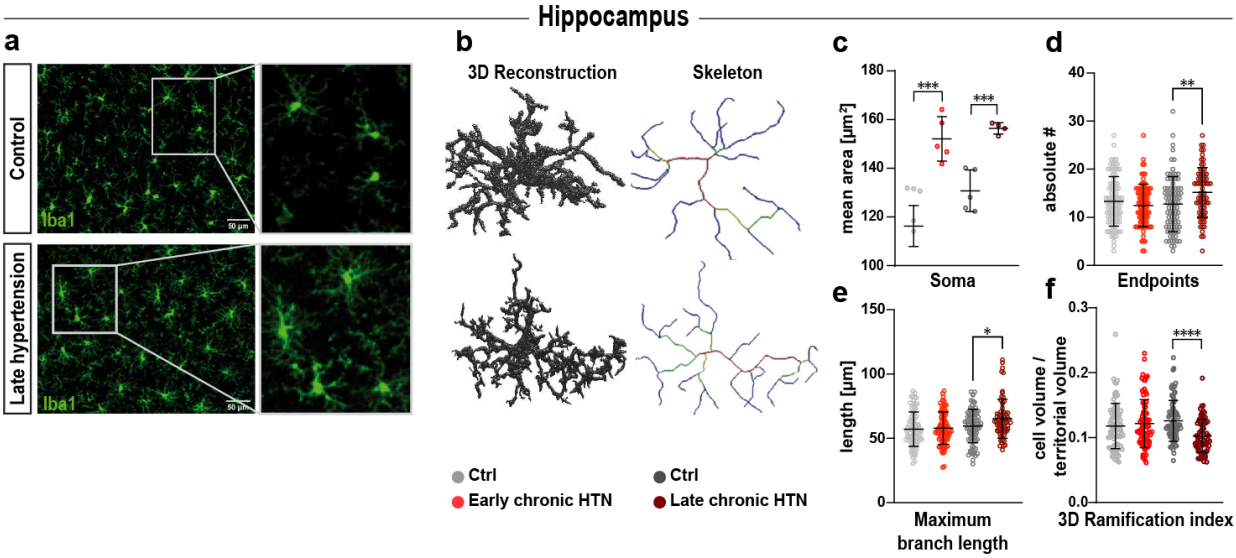

Fig. 33 Hypertensive microglia exhibit increased soma size and branching complexity in the hippocampus

Representative IBA1 immunofluorescence images of 15-20 microglia cells of 4 fields of view per animal in the hippocampal CA1 region from Ctrl and late chronic HTN rodents. Scale bar: 50 µm. (b) 3D microglia reconstruction and skeletonization displaying increased complexity in HTN rodents. (c-f) Quantification of microglial morphological parameters: (c) soma area, (d) number of endpoints, (e) maximum branch length, and (f) 3D ramification index. 15-20 microglial cells were analyzed from 5 independent rodents for each group and brain region. Individual data points in (c) indicate averaged microglia data per rodent, or individual microglia within a defined region (d-f). Data are presented as mean ± s.e.m. Statistical significance: *$p < 0.05$, **$p < 0.01$, ***$p < 0.001$, ****$p < 0.0001$.

Similarly, in the cortex, HTN microglia exhibited notable morphological changes. Confocal microscopy images (Fig. 34a) and subsequent 3D reconstructions (Fig. 34b) revealed an increased somatic area in HTN microglia compared to Ctrl (Fig. 34c). The number of endpoints did not significantly differ between groups (Fig. 34d), but maximum branch length (Fig. 34e) and 3D ramification index (Fig. 34f) were significantly altered in late chronic HTN rodents. In the context of chronic HTN, this morphological approach revealed that the longer HTN persisted, the more cell territory microglia occupied, evidencing that microglia increase their somata already in the early phase of HTN and becomes enlarged as a result of a chronic systemic hypertensive states.

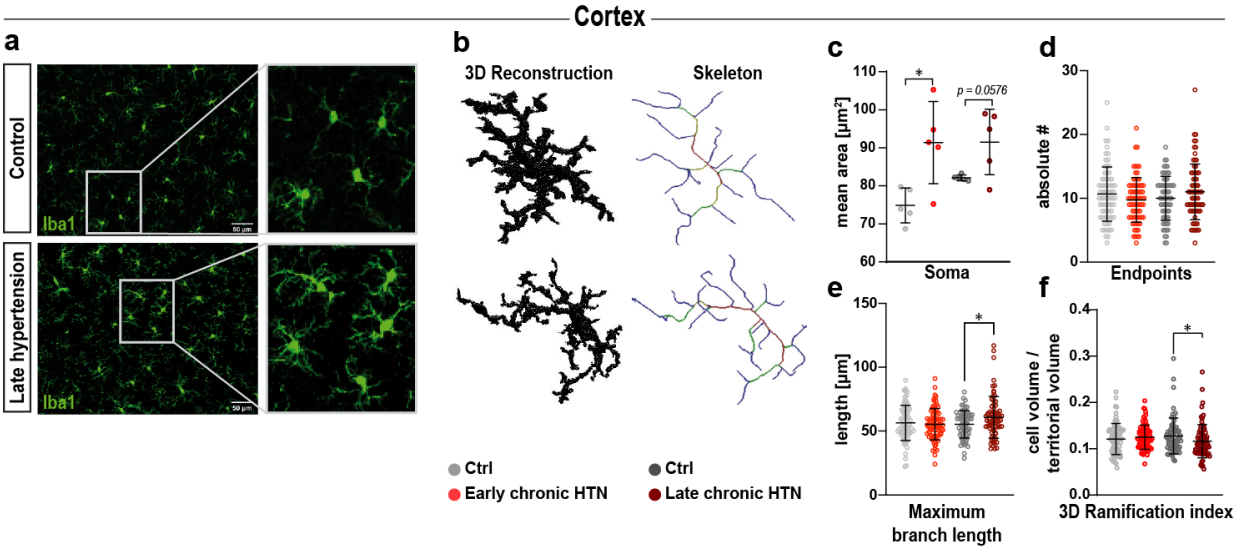

Fig. 34 Cortical microglia exhibit increased branching complexity in chronic HTN

(a) Representative IBA1 immunofluorescence images of 15-20 microglia cells of 4 fields of view per animal in the retrosplenial cortex from Ctrl and late chronic HTN rodents. Scale bar: 50 µm. (b) 3D microglia reconstruction and skeletonization displaying increased complexity in HTN rodents. Quantification of microglial morphological parameters: (c) soma area, (d) number of endpoints, (e) maximum branch length, and (f) 3D ramification index. 15-20 microglial cells were analyzed from 5 independent rodents for each group and brain region. Individual data points in (c) indicate averaged microglia data per rodent, or individual microglia within a defined region (d-f). Data are presented as mean ± s.e.m. Statistical significance: $*p < 0.05$.

Given that the morphology of microglia partially reflects its response, the next step was to specifically identify and characterize microglial populations by analyzing changes in microglia surface marker expression in both early and late chronic hypertensive states.

4.3 Phenotypical characterization of microglia using flow cytometric analysis

To investigate the phenotypical profile of microglia in response to chronic HTN, we analyzed microglia populations derived from the hippocampus (Fig. 35a) and cortex (Fig. 35b) of Ctrl and HTN rodents. We employed a gating strategy to identify individual live cells, excluding doublets,

cell debris, and non-viable cells using a live/dead dye. Traditionally, microglia are identified as $CD11b^{+}CD45^{int}$, whereas $CD11b^{+}CD45^{high}$ population corresponds for other CNS macrophages (166). However, microglia respond to inflammatory states upregulating CD45 (84,167), resulting in an incorrect classification of bone marrow derived macrophages. Therefore, the main populations of cells were identified through Forward Scatter light (FSC) and CD45 expression for both early and late chronic HTN with their respective age-matched normotensive Ctrl. Target cells were further gated as $CD45^{+}$ and $CD11b/c^{+}$ positive cells. Cells positive for CD45, CD11b/c and P2Y purinoceptor 12 (P2Y12) were classified as microglia from hippocampus (Fig. 35a) and cortex (Fig. 35b). P2Y12 has been identified as a receptor selectively expressed on microglia and can be used as a marker to distinguish CNS resident microglia from blood-derived myeloid cells (94,168). We have developed such gating strategy considering microglia activation appropriate for its senescent and inflammatory response that yields them indistinguishable from recruited myeloid cells.

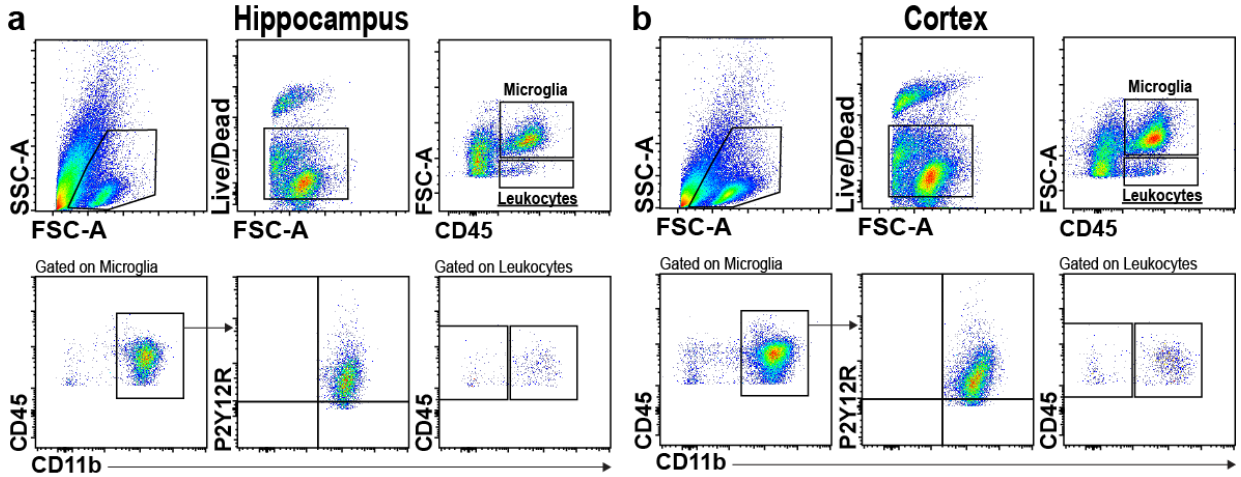

Fig. 35 Gating strategy for the identification of microglia in the hippocampus and cortex

Identification of microglia derived from (a) hippocampus and (b) cortex of Ctrl and HTN rodents via FACS analysis. Representative flow cytometry plots of early chronic HTN cells illustrating the gating strategy used to identify microglial populations. Initially, cells were gated on FSC-A vs. side scatter SSC-A to exclude debris. Live cells were then selected using a live/dead dye, gating on FSC-A to exclude dead cells. Main populations of cells were identified through FSC and CD45. Microglia and leukocytes were distinguished based on CD45 expression, with microglia identified as $CD45^{+}CD11b/c^{+}$ cells. Further gating was performed on P2Y12R expression to specifically identify resident microglia.

First, median fluorescence intensity (MFI) for FSC on $CD45^{+}CD11b/c^{+}P2Y12R^{+}$ was used to investigate microglial physical properties in the hippocampus (Fig. 36) and cortex (Fig. 37). Thereafter, our analysis was focused solely on CD45, CD11b/c, P2Y12 gated microglia to

investigate the density of markers associated with anti-inflammatory and pro-inflammatory microglial pathways.

Flow cytometric analysis of hippocampal microglia showed distinct differences in cell frequency, size, and count between Ctrl and HTN. Specifically, the percentage of single live cells identified as microglia significantly decreased in the late Ctrl group (Fig. 36a). Furthermore, the median fluorescence intensity (MFI) of forward scatter (FSC-A), indicator of cell size, revealed a significant increase in both late Ctrl and late chronic HTN microglia, evidencing microglial hypertrophy in response to age and chronic HTN (Fig. 36b). Last, the absolute number of microglia was significantly reduced in the late chronic HTN compared to their age-matched Ctrl, pointing to loss or redistribution of microglia in the hippocampus under prolonged hypertensive stress (Fig. 36c).

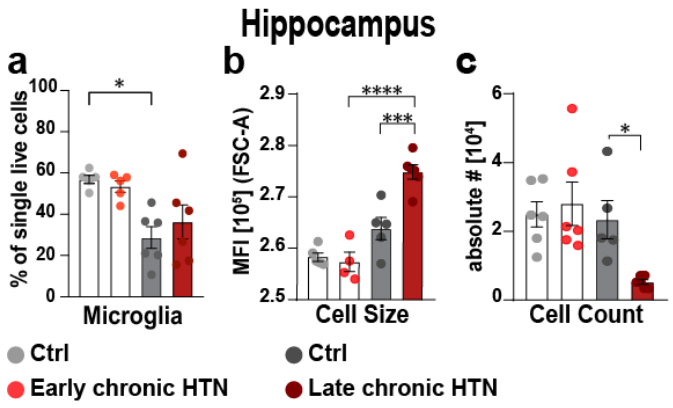

Fig. 36 Microglial frequency, cell size, and cell count in the hippocampus during chronic hypertension

(a) bar graphs representing the percentage of single live cells identified as microglia (b) bar graphs representing the MFI of forward scatter (FSC-A) indicative of cell size (c) bar graphs representing the absolute number of microglia. Data are presented as mean ± s.e.m. *$p < 0.05$, ***$p < 0.001$, and ****$p < 0.0001$.

Following the analysis of hippocampal microglia, cortical microglia was also investigated to discern any regional differences in microglial response to chronic HTN. Flow cytometric data revealed that, similar to the hippocampus, the percentage of single live microglia cells significantly decreased in both late Ctrl and late chronic HTN compared to their younger counterparts (Fig. 37a). Moreover, the MFI of FSC-A, demonstrated significant hypertrophy in cortical microglia in late Ctrl, with late chronic HTN displaying a more pronounced enlargement (Fig. 37b). This hypertrophy mirrors the morphological changes observed in hippocampal microglia and demonstrate a generalized microglial response to hypertensive stress in these brain regions. Furthermore, the absolute number of cortical microglia increased significantly in the late Ctrl group, whereas no difference was observed in the late chronic HTN cortex when compared to their younger counterparts (Fig. 37c).

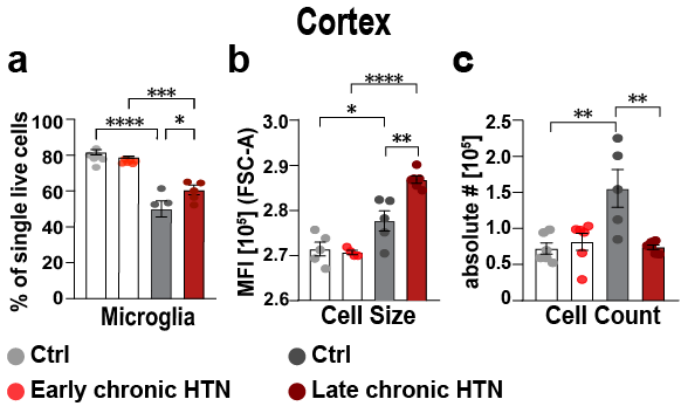

Fig. 37 Microglial frequency, cell size, and cell count in the cortex during chronic hypertension

(a) bar graphs representing the percentage of single live cells identified as microglia (b) bar graphs representing the MFI of forward scatter (FSC-A) indicative of cell size (c) bar graphs representing the absolute number of microglia. Data are presented as mean ± s.e.m. $*p < 0.05$, $**p < 0.01$, $***p < 0.001$, $****p < 0.0001$.

4.4 Age and hypertension-dependent differences in the marker expression profile of hippocampal microglia

To characterize microglial phenotypes in homeostasis, early and chronic HTN, we profiled microglia using eight distinctive markers (CD45, CD11b/c, P2Y12, CX3CR1, CD200r, CD163, MHCII (RT1B) and CD86). We first investigated age-associated changes and found an increased age-dependent expression of CD45 in HTN as well as in Ctrl groups (Fig. 38), confirming previous findings where aging alone yields an increase in microglial CD45 expression (84,172). Additionally, age-dependent inhibition of CD11b/c, CX3CR1, CD163, and CD86 surface markers was observed in both groups. Even though microglia cell surface expression of integrins CD11b/c was age-dependently downregulated in Ctrl and chronic HTN, its overall expression was significantly higher in HTN rodents at both time points. The functional role of CX3CR1 in modulating microglia morphology is supported by findings that CX3CR1-deficient microglia exhibit a transcriptome consistent of accelerated aging (173), aligning with our results of an age-dependent CX3CR1 reduction. Additionally, we observed a significant age-related increase in microglia expressing RT1B (MHC-II) in the Ctrl group. Studies have shown that the expression of MHC class II molecules in the CNS is age-dependent, not only restricted to regulate inflammatory stimuli (174,175). In HTN rodents, a significant upregulation of P2Y12 was observed in early chronic HTN, which was later suppressed, resulting in an age-dependent decrease exclusive to hypertension. Scavenger receptor CD163, known to ameliorate inflammation in the aging brain (176), revealed a decreased expression in both groups as an age-dependent effect. Elevated CD200R expression, associated with the activation of anti-inflammatory pathways, was significant upregulated in early chronic HTN. Interestingly, a prominent upregulation of membrane co-stimulatory receptor CD86 was observed in early chronic HTN. CD86, responsible for immune cell

proliferation, classifies microglia as primed or in transition to an activated inflammatory phenotype. Given that the expression of markers characteristic of both anti-inflammatory and pro-inflammatory pathways were found significantly higher in early chronic HTN when compared to Ctrl, we aimed to explore between multiple sub-populations responsible for the activation of these pathways.

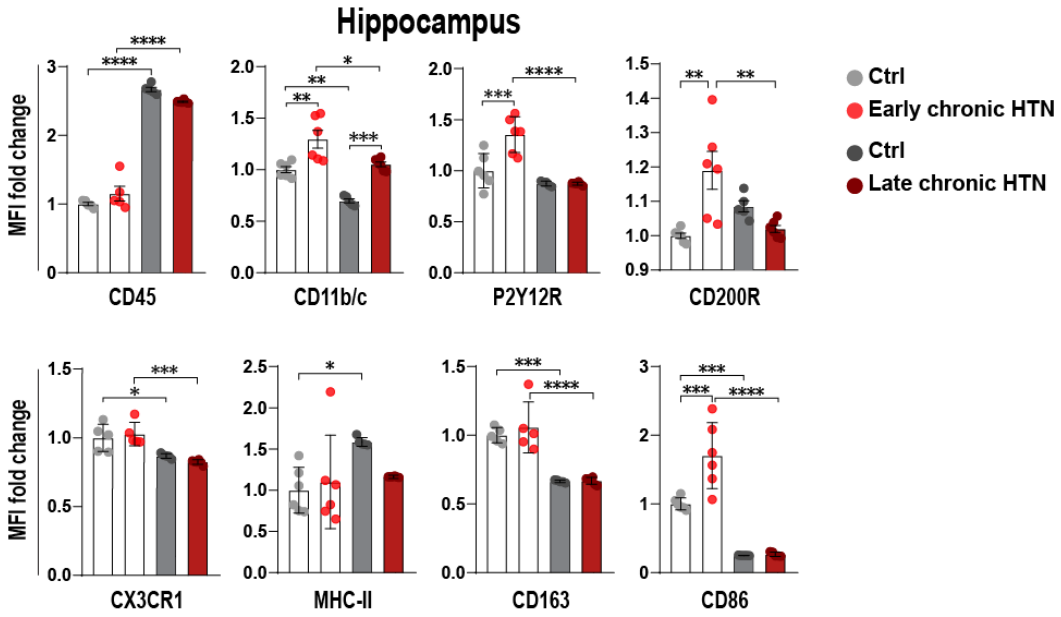

Fig. 38 Hippocampal microglia cell reactivity, age-related profile and dynamic activation in chronic HTN

Bar charts displaying the median fluorescence intensity (MFI) fold change for CD45, CD11b/c, P2Y12R, CD200R, CX3CR1, MHC-II (RT1B), CD163, and CD86 on hippocampal microglia. Fold changes were obtained by comparing the average expression normalized to the early Ctrl group. Data are presented as mean ± s.e.m. *$p < 0.05$, **$p < 0.01$, ***$p < 0.001$, ****$p < 0.0001$.

4.5 Identification of distinct hippocampal microglial subpopulations using automated clustering multidimensional analysis

After manually gating microglia using traditional methods, we applied an unbiased, multidimensional approach to investigate the composition and phenotypic variations of microglia subpopulations. By using Uniform Manifold Approximation and Projection (UMAP) visualization, we mapped hippocampal microglia subpopulations for early and late chronic HTN (Fig. 39). This computational technique places cells with similar phenotypes close together, allowing for an automated clustering analysis to assess the different subpopulations within the microglia population (Fig. 39a-c, e-g). Distinct phenotypic variations were identified within the microglia

subpopulations by visualizing the co-expression of surface molecules in a heatmap for detailed sub-cluster analysis (Fig. 39d, h)

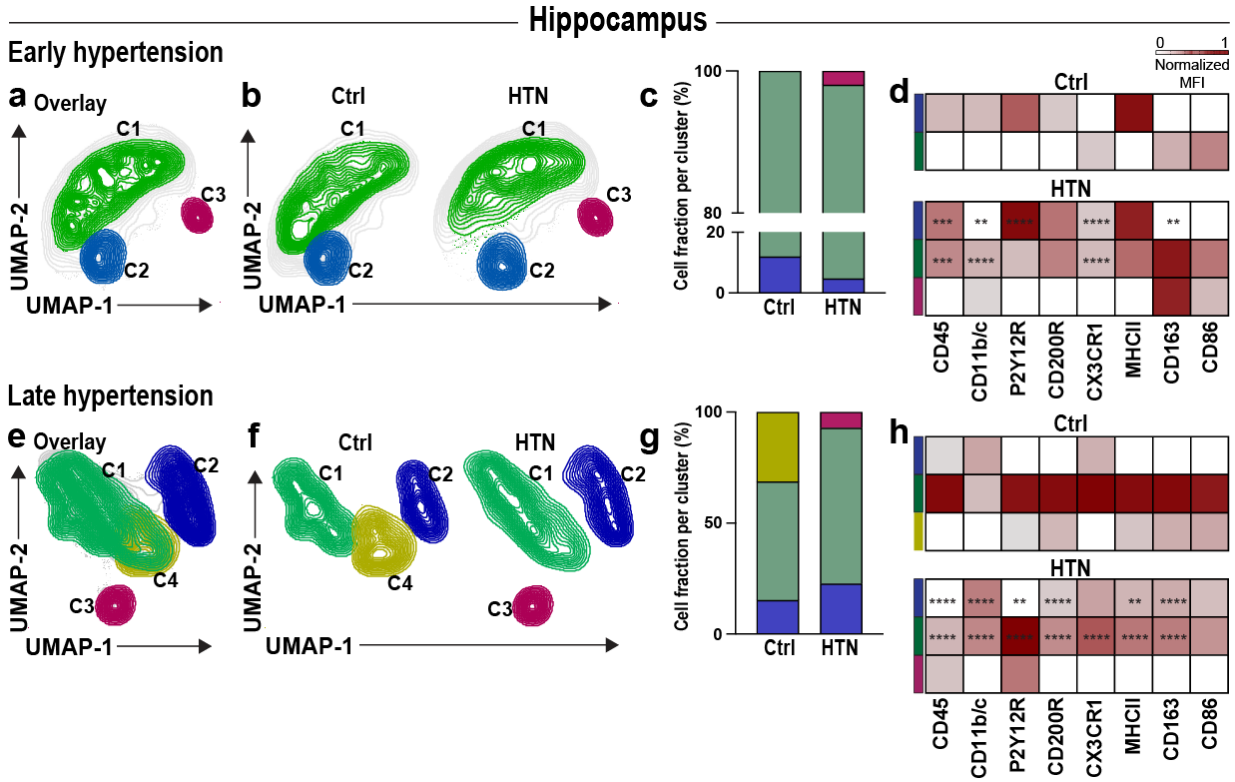

Fig. 39 Unsupervised clustering reveals phenotypic variations in hippocampal microglia sub-populations during early and late chronic hypertension

(a) Overlay of UMAP plots displaying microglial sub-populations identifying three distinct clusters (C1, C2, C3) in early HTN for control (Ctrl) and hypertensive (HTN) groups analyzed by flow cytometric analysis (b) Representative UMAP plots for Ctrl and HTN groups during early HTN, identifying microglia sub-clusters corresponding to each cohort. (c) Relative frequencies of microglia cell fraction per cluster (%) in Ctrl and HTN groups during early HTN, demonstrating the distribution of microglial sub-populations. (d) Heatmap displaying the normalized median fluorescence intensity (MFI) for each cluster during early HTN exhibiting significant differences in the expression of analyzed surface markers (CD45, CD11b/c, P2Y12R, CD200R, CX3CR1, MHC-II, CD163, CD86) between Ctrl and HTN groups. (e) Overlay of UMAP plots displaying microglial sub-populations identifying four distinct clusters (C1, C2, C3, C4) in late HTN for Ctrl and HTN groups. (f) Representative UMAP plots for Ctrl and HTN groups during late HTN, identifying microglia sub-clusters corresponding to each cohort. (g) Relative frequencies of microglia cell fraction per cluster (%) in Ctrl and HTN groups during late HTN. (h) Heatmap displaying the normalized MFI for each cluster during late HTN exhibiting significant differences in the expression of the analyzed surface markers between Ctrl and HTN groups. Statistical significance in the Heatmaps is denoted as follows: $^{**}p < 0.01$, $^{***}p < 0.001$, $^{****}p < 0.0001$.

Our results uncovered a specialized group of microglia that exhibit particular markers (CD86, CD11b/c, and CD163) exclusively in early chronic HTN, which is represented by cluster 3 (C3) (Fig. 39b-d). In the early chronic HTN stage, a reduction in the population density of microglial cells within cluster 2 (C2) was observed (Fig. 39c) showing that a substantial portion of these cells

might be transitioning, as indicated by their presence in cluster 3 (C3). Further examination revealed that HTN cluster 2 (C2) exhibited higher expression of P2Y12R than Ctrl microglia (Fig. 39d) supporting the observation that the upregulation of P2Y12R in the overall hippocampal microglial assessment (Fig. 38) was attributable to this specific cluster.

In late Ctrl, a specific subset of microglia, referred to as cluster 4 (C4) (Fig. 39f, g), accounted for one-third of the total microglia population. These cells, which exhibited similar characteristics, were positioned closely together in a 2D UMAP plot, showing transition from cluster 1 (C1) (characterized by homeostatic markers) and cluster 2 (C2) (Fig. 39f, g). During late chronic HTN, a shift in microglia population was observed, with a decline in cluster 1 (C1) and an increase in cluster 2 (C2) (Fig. 39f, g). This shift was associated with a decrease in the expression of CD200R, CD45, CD163, MHC-II, P2Y12R, and CX3CR1 in cluster 1 (C1) and an increase in CD11b/c expression. Additionally, cluster 2 (C2) displayed significantly higher expression of CD200R, CD45, CD163, RT1B (MHC-II), CD11b/c, and P2Y12R revealing the presence of a second reactive microglial cluster. Lastly, in late chronic HTN, the appearance of cluster 3 (C3) displayed distinctive expression of CD45 and P2Y12 receptor that was not found in Ctrl (Fig. 39f-h). Our automated clustering method exposed distinct differences in phenotypic features and co-expression patterns of surface molecules during the early and late stages of chronic HTN.

4.6 Age and hypertension-dependent differences in the marker expression profile of cortical microglia

In the cortex, as observed in the hippocampus, there was an age-dependent increase in CD45 expression in Ctrl and HTN rodents (Fig. 40). Additionally, cellular senescence was characterized by significant age-dependent upregulation of the inhibitory immune receptor CD200R and downregulation of CD11b/c, CD163, and CD86 surface markers in both groups.

Furthermore, the Ctrl group exhibited an increase in RT1B (MHC-II) and fractalkine receptor CX3CR1 expression as they aged. In contrast, HTN rodents showed a higher level of RT1B (MHC-II) in early chronic HTN compared to age-matched Ctrl, but it decreased in late chronic HTN, resulting in a lower level than Ctrl. CX3CR1 expression also followed a similar pattern, with a significant drop in HTN rodents in late chronic HTN.

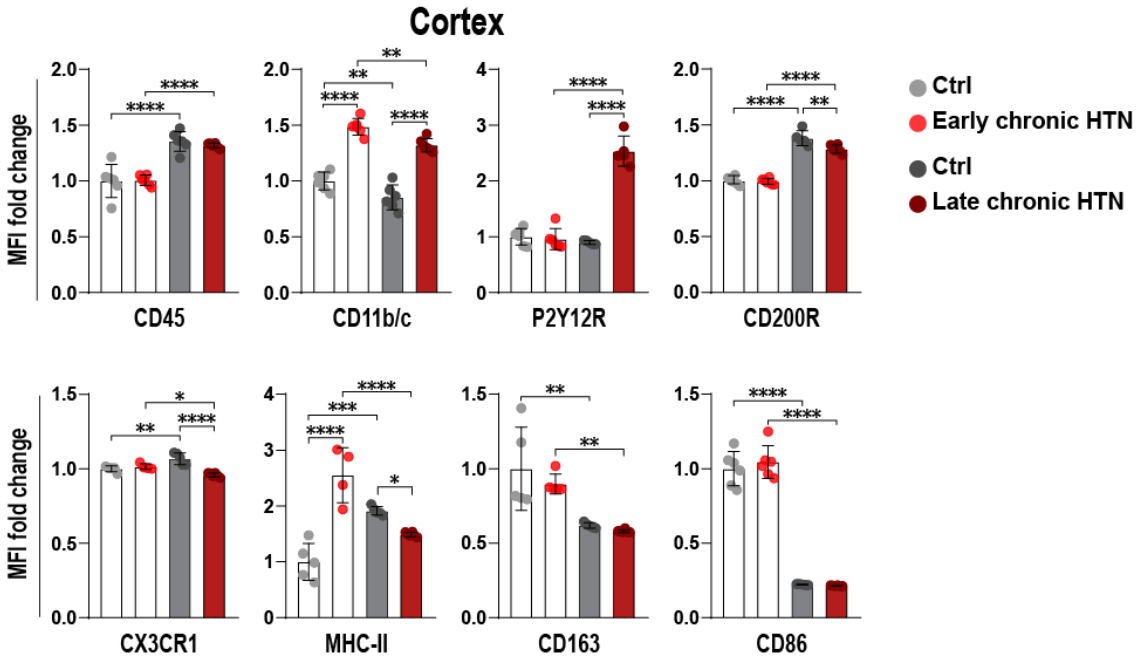

Fig. 40 Cortical microglia cell reactivity, age-related profile and dynamic activation in chronic HTN

Bar charts displaying the median fluorescence intensity (MFI) fold change for CD45, CD11b/c, P2Y12R, CD200R, CX3CR1, MHC-II (RT1B), CD163, and CD86 on cortical microglia. Fold changes were obtained by comparing the average expression normalized to the early Ctrl group. Data are presented as mean ± s.e.m. *$p < 0.05$, **$p < 0.01$, ***$p < 0.001$, ****$p < 0.0001$.

These results reveal that in senescent Ctrl microglia, there is an upregulation of RT1B (MHC-II). However, in late chronic HTN, there is a shift towards an anti-inflammatory microglial phenotype. Interestingly, the P2Y12 receptor was strongly upregulated in late chronic HTN, indicating enhanced microglial chemotaxis.

4.7 Identification of distinct cortical microglial subpopulations using automated clustering multidimensional analysis

Phenotypic variations in microglia subpopulations in the cortex were analyzed using the unsupervised graph-based clustering approach, resulting in 2D maps of microglia subpopulations in early chronic (Fig. 41a) and late chronic HTN (Fig. 41e). In early chronic HTN, six distinct clusters were identified in Ctrl brains, whereas HTN brains exhibited only five clusters. In late chronic HTN, five clusters were observed in Ctrl brains, compared to seven clusters in HTN brains. These subpopulations were defined based on specific patterns of pro- and anti-inflammatory pathways. In early chronic HTN, the largest fraction of microglia localized similarly in Ctrl and HTN in cluster 1 (C1) (Fig. 41a-c). Distinctly, some clusters were absent or unique to a specific group. For instance, cluster 5 (C5), characterized by high expression of CD45, CD11b/c, P2Y12R, CD200R, and MHC-II, was entirely absent in HTN brains. Cluster 2 (C2) was present in both

groups but had a higher proportion of microglia in HTN brains. Cluster 3 (C3) in HTN brains showed increased expression of CD200R and CX3CR1 but lower levels of CD45 and CD86, while cluster 4 (C4) exhibited higher levels of CD45 and CD11b/c (Fig. 41d).

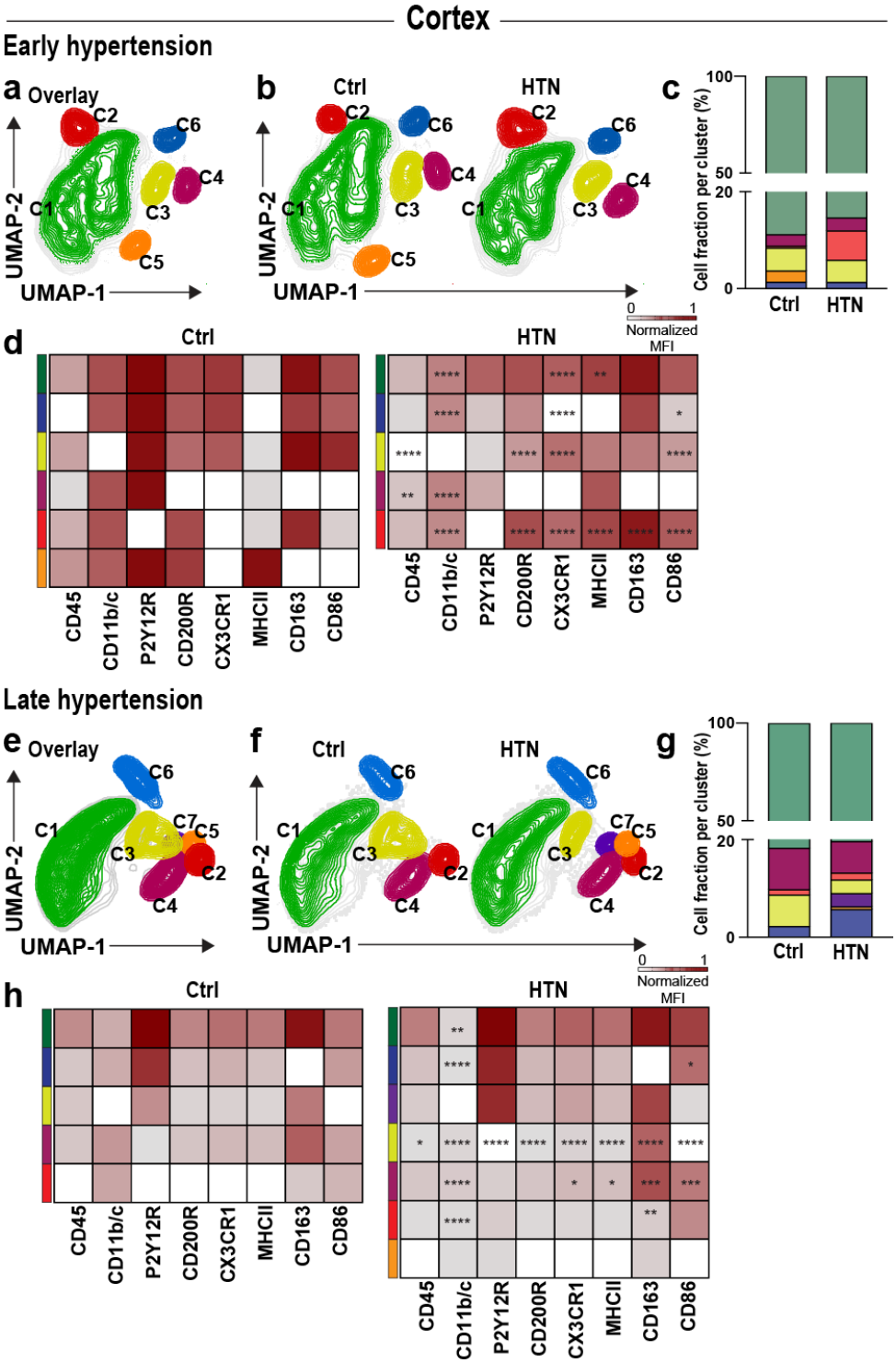

Fig. 41 Unsupervised clustering reveals phenotypic variations in cortical microglia sub-populations during early and late chronic hypertension

(a) Overlay of UMAP plots displaying microglial sub-populations identifying six distinct clusters (C1, C2, C3, C4, C5, C6) in early HTN for control (Ctrl) and hypertensive (HTN) groups. (b) Representative UMAP plots for Ctrl and HTN groups during early HTN, identifying microglia sub-clusters corresponding to each cohort. (c) Relative frequencies of microglia cell fraction per cluster (%) in Ctrl and HTN groups during early HTN. (d) Heatmap displaying the normalized median fluorescence intensity (MFI) for each cluster during early HTN exhibiting significant differences in the expression of the analyzed surface markers (CD45, CD11b/c, P2Y12R, CD200R, CX3CR1, MHC-II, CD163, CD86) between Ctrl and HTN groups. (e) Overlay of UMAP plots displaying microglial sub-populations identifying seven distinct clusters (C1, C2, C3, C4, C5, C6, C7) in late HTN for Ctrl and HTN groups. (f) Representative UMAP plots for Ctrl and HTN groups during late HTN, identifying microglia sub-clusters corresponding to each cohort. (g) Relative frequencies of microglia cell fraction per cluster (%) in Ctrl and HTN groups during late HTN. (h) Heatmap displaying the normalized MFI for each cluster during late HTN, exhibiting significant differences in the expression of the analyzed surface markers between Ctrl and HTN groups. Statistical significance in the heatmaps is denoted as follows: $^{**}p < 0.01$, $^{***}p < 0.001$, $^{****}p < 0.0001$.

In late chronic HTN, microglia were primarily localized in cluster 1 (C1) in both Ctrl and HTN groups (Fig. 41e-g). A lower fraction of HTN microglia was found in cluster 3 (C3), which showed higher reactivity with increased expression of CD200R, CX3CR1, CD163, MHC-II, and CD11b/c (Fig. 41h). Furthermore, two additional clusters (C5 and C7) were identified in HTN brains that were absent in the Ctrl group. Microglia in cluster 7 (C7) expressed high levels of CD45, P2Y12R, CD200R, CX3CR1, MHC-II, and CD163, while microglia in cluster 5 (C5) expressed CD11b/c, P2Y12R and CD163.

The variations in cortical microglia during early and late chronic HTN were more complex than those in the hippocampus, as shown by a larger number of distinct clusters. Although both regions exhibited unique cluster compositions, the cortex displayed a more complex array of sub-populations, with certain clusters being absent or unique to HTN brains. The changes in surface marker patterns from early to late HTN indicate that the predominant density of microglia in cluster 1 (C1) remained relatively consistent, evidencing that certain microglial sub-populations arise due to hypertension-induced changes, while others are linked to the aging process.

4.8 Distinct microglial morphological characteristics observed in the cortex of patients with hypertensive cerebral small vessel disease

After the detailed analyses microglial phenotypes in the rodent model of cSVD, we extended our investigation to human subjects to compare our morphological findings. Considering the complex interplay between microglia and hypertensive cSVD observed in the SHRSP, we sought to determine if comparable microglial alterations occur in the human brain of elderly individuals who

had been diagnosed with hypertensive cSVD. This condition was confirmed and characterized by the presence of white matter lesions (WML), vessel hyalinosis, and enlarged perivascular spaces in the subcortical white matter and basal ganglia (Fig. 42).

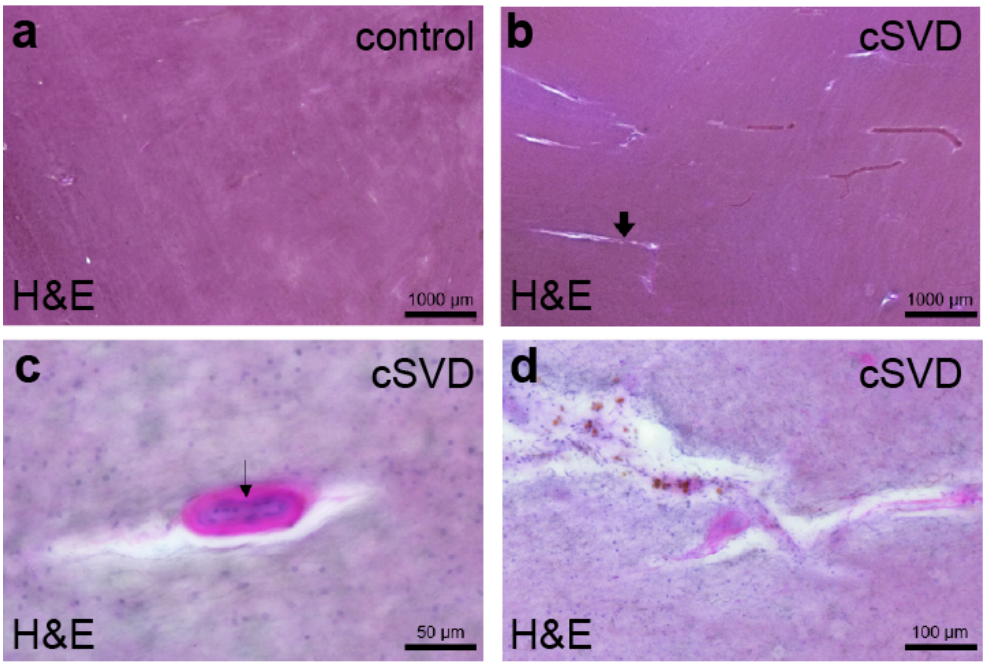

Fig. 42 Histopathological alterations in the brain tissue of patients with cerebral small vessel disease compared to controls

Pathological hallmarks of arteriosclerosis (AS) in the human brain visualized in the subcortical white matter with the modified H&E stain in 100µm-thick brain sections. In comparison with control cases (a), overview images show tortuous vessels running in enlarged perivascular spaces (thick black arrow) in the white matter cSVD cases (b), scale bar: 1000 µm (c) Higher magnification image of cSVD brain tissue showing white matter vessel with hyalinosis in the tunica media. The arrow points to a vessel with thickened walls due to hyalinosis (thin black arrow), scale bar: 50 µm. (d) cSVD brain tissue illustrating enlarged perivascular spaces, aggregates of brown hemosiderin in the perivascular space of a white matter vessel indicative of old microbleed, scale bar: 100 µm.

Our analysis revealed a notable increase in the number of $IBA1^+$ microglia per mm^2 in cSVD tissue samples (Fig. 43a-e). Quantification of vascular-associated microglia (VAMs) revealed a significant increase in their density relative to the total number of $IBA1^+$ cells in cSVD individuals compared to Ctrl (Fig. 43f). Detailed microglial morphological analysis showed that $IBA1^+$ cells in cSVD cases exhibited a significantly enlarged somatic area compared to Ctrl (Fig. 43g), a trend in higher branching area (Fig. 43h), and these microglia displayed a significant reduced 2D ramification index (Fig. 43i). These findings align with the results observed in the SHRSP model.

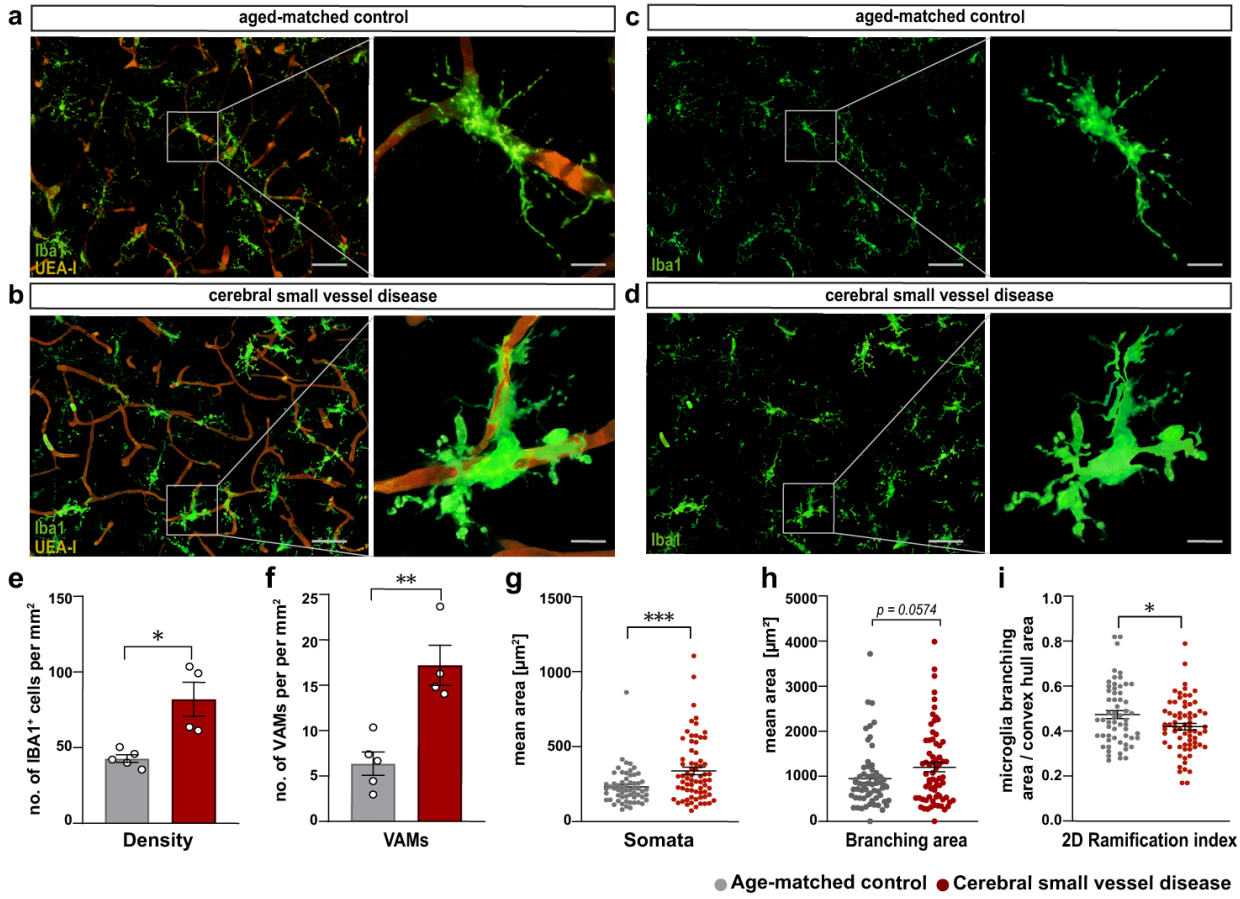

Fig. 43 Distinct microglial morphological features observed in post-mortem tissue from patients with hypertensive cerebral small vessel disease

(a-d) Representative confocal images of individual vascular-associated IBA1$^+$ microglia (VAMs) in the cingulate cortex in post-mortem tissue of age-matched controls (a, c), and cSVD individuals (b, d) individuals. Insets highlight detailed morphological differences between groups (scale bar overview image = 100 µm; single cell = 25 µm). (e) Quantification of IBA1$^+$ microglial density within a defined area of 1,013,205 µm^3 standardized to 1mm^2, displaying a significant increase in cSVD cases compared to Ctrl. (f) Number of VAMs per mm² within the defined region demonstrating a significant increase in cSVD individuals. (g-i) Quantification of different morphological features of microglia (soma size, average branch area and ramification index). Individual data points indicate averaged microglia data from an individual donor (e, f) or individual microglia within the defined region (g-i). Columns and error bars show mean ± s.e.m; (a-f), n = 5 controls, n = 4 cSVD subjects. (g-i), n = 145 microglia in age-matched controls, n = 222 microglia in cSVD individuals. Statistical significance is denoted as follows: *$p < 0.05$, **$p < 0.01$, and ***$p < 0.001$.

5 Discussion

Hypertensive cerebral small vessel disease (cSVD) represents a significant challenge in the field of neurovascular research, as it leads to cognitive decline and increased risk of stroke. It is essential to understand the cellular and molecular mechanisms that contribute to this condition to develop effective therapeutic strategies. This research focuses on two key components of the NVU: cerebral pericytes and microglia. By examining how these cells adapt their phenotype and metabolism under hypertensive conditions, the aim was to uncover their roles in vascular pathology and neuroinflammation associated with cSVD.

In this dissertation, the responses of pericytes and microglia to chronic arterial hypertension were investigated by studying rodent models and human post-mortem brain tissue. The findings in this thesis reveal significant phenotypic and metabolic changes in pericytes, as well as distinct patterns of microglial activation, which collectively contribute to the progression of hypertensive cSVD. By integrating these findings, in this chapter, I present a comprehensive perspective on how hypertension influences the NVU, which provide a new understanding into potential therapeutic targets for mitigating the impact of chronic hypertensive states on the brain.

5.1 Phenotypic and metabolic adaptations in pericytes under hypertensive stress

5.1.1 Pericyte phenotypic changes

In the field of brain vascular biology, our understanding of hypertensive vascular pathology has advanced significantly; however, the phenotypic and metabolic mechanisms of such changes, particularly at the level of cerebral pericytes, remain underexplored. Our *in vivo* and *in vitro* studies have demonstrated significant phenotypic changes in pericytes under hypertensive conditions, characterized by increased co-expression of NG2 and CD13, indicative of a stressed vascular phenotype adapting to ongoing hypertensive insult. These cellular transformations correlate with a profound metabolic reprogramming where pericytes shift towards a glycolysis-dominant metabolism already in the initial phase of hypertension, emphasizing a paradigm shift in the metabolic programming of brain pericytes. This shift is not merely a passive reaction to altered physiological conditions but a proactive adaptation that can profoundly influence vascular metabolism and function (177,178).

Pericytes, traditionally recognized for their role in capillary blood flow regulation and BBB integrity (37,45,49), emerged from our study as central players in the metabolic reprogramming associated with hypertension. We detected, even in the initial stages of hypertension, a modest yet significant diversification in pericyte marker expression early on, with increases in NG2 and CD13 co-expression, indicating an early cellular response to rising blood pressure. Our findings revealed a critical transformation in pericyte phenotype, marked by the upregulation of NG2 and CD13 and the concurrent downregulation of PDGFRß. After CNS injury, NG2-reactive pericytes can be found on microvessels (51), where they function as inflammation sensors and assist with immunosurveillance and effector functions for the recruitment of neutrophils and macrophages. Our findings suggest that NG2 pericytes may exert a particular role in hypertension-induced CNS injury that is linked to immune cell recruitment and neuroinflammation. Therefore, it seems probable that NG2 pericytes are also players in the development of cSVD, by increasing BBB permeability, inflammatory infiltrates, and progressive CNS damage. Increased expression of CD13 is a hallmark of an inflammatory response as it facilitates monocyte and endothelial cell adhesion, which is a critical event in the progression of vascular diseases (179). The significant increase of CD13 pericytes in HTN is consistent with literature showing that CD13 plays a pivotal role in inflammation and vascular remodeling (179,180). Specifically, CD13 functions as a mediator of monocyte adhesion to endothelial cells (180), potentially contributing to the inflammatory environment associated with cSVD. However, these studies were performed to determine the role of CD13 as an adhesion molecule in trafficking of inflammatory cells to the site of injury following myocardial infarction induced by permanent coronary artery occlusion. Here, we postulate that CD13 pericytes at sites of brain microvascular injury may mediate inflammatory cell adhesion contributing to brain vascular remodeling. The distinct expression of these markers observed in our results highlight a specific involvement of NG2 and CD13 in disease-specific vascular remodeling processes in the brain. NG2 acting as a general stress response marker, with its increased expression occurring upon in vitro stress and hypertensive conditions, whereas the upregulation of CD13 specific to hypertensive stress emphasizes its role in severe vascular responses, potentially leading to pathological changes. Overall, this phenotypic shift suggests that pericytes are transitioning from their typical function towards a phenotypical state that is prepared for acute stress responses and tissue repair.

5.1.2 Gene expression and molecular pathways

The gene expression profile of microvessels across various stages of hypertension demonstrates a complex interplay of mechanisms that drive vascular pathology in chronic hypertension. The early stage of chronic hypertension was characterized by an upregulation of genes involved in lipid metabolism, angiogenesis, and inflammatory responses, suggesting an active process of vascular remodeling. Key genes, such as *Agtr1a, Ren*, and *Acta2*, enhance systemic blood pressure regulation through their roles in the renin-angiotensin system, directly affecting pericyte contractility and vascular tone. Specifically, the *Agtr1*a gene encodes the angiotensin II type 1A receptor, which is essential for vascular and hemodynamic responses to angiotensin II. Studies have demonstrated that targeting this receptor leads to decreased blood pressure, reduced vascular tone responses, and significantly extends the lifespan of mice (181–183). Renin, encoded by the *Ren* gene, catalyzes the conversion of angiotensinogen to angiotensin I, which is a crucial step in the renin-angiotensin-aldosterone system that influences fluid balance and vascular tone both vital for the regulation of blood pressure (184). Furthermore, alpha-smooth muscle actin, encoded by the *Acta2* gene, plays a crucial role in the contractile function of vascular smooth muscle cells and pericytes. In conditions such as pulmonary hypertension *Acta2*-expressing pericytes undergo expansion and partial smooth muscle cell differentiation, contributing to arteriolar muscularization (185). This leads to dysregulated signaling pathways that favor endothelial cell activation and inflammation (185). The activation of the renin-angiotensin system at the early chronic HTN stage highlights the crucial function of these genes in regulating vascular responses and preserving vascular integrity amid hypertensive conditions.

Similarly, Notch3, supports the restructuring of vascular architecture by influencing both pericyte function and endothelial cell interactions essential for adapting to increased hypertensive stress and maintaining vascular integrity (186,187). And Protease-Activated Receptor 1 (PAR1), encoded by the *F2r* gene, plays a crucial role in vascular homeostasis, inflammation, and thrombosis, all of which are essential processes in vascular remodeling and the response to hypertension (188). Parallel to these regulatory genes, a significant vascular inflammatory response was evident from the upregulation of *Tnf, Ccl2, Ccl5, Il1b, Il6, Ifng*, and *Nos2*, genes that orchestrate a robust immune response by mobilizing immune cells, exacerbate vascular inflammation, and contribute to atherosclerotic lesion formation (189–194). With the surge in *Ccl5*, an upregulation of *Il10* was detected, which may potentially serve as a compensatory mechanism to mitigate excessive inflammatory damage and preserve vascular function. This is because IL-10 has been shown to

exert an up-regulatory effect on the anti-hypertensive activity of CCL5 (195). Structural remodeling can be additionally mediated by *Mmp9* and *Vegfb*. This interaction is vital for both physiological and pathological vascular responses (196,197), as it plays a role in both normal and abnormal vessel growth. *Mmp9* is responsible for breaking down and reorganizing the extracellular matrix, which is essential for vascular repair, while *Vegfb* promotes pathological angiogenesis (198), especially when VEGF levels are elevated. This can lead to vascular damage and the growth of abnormal blood vessels, indicating an adaptive yet potentially harmful response.

In the late chronic phase of HTN, a notable change occurs with a decrease in the expression of numerous genes that were previously upregulated, which could suggest a potential exhaustion of metabolic and adaptive capacities. However, the significant upregulation of *Sod1* is noteworthy. *Sod1* is crucial in mitigating oxidative stress by catalyzing the dismutation of superoxide radicals into oxygen and hydrogen peroxide. The increased expression of *Sod1* in late chronic HTN may indicate a heightened oxidative stress environment within vascular cells (199). This adaptive response may serve to counteract increased oxidative damage caused by prolonged hypertension (12), aiming to maintain cellular function and prevent oxidative injury (200). However, persistent high expression of *Sod1* could also reflect the continuous stress state of vascular cells, potentially leading to additional pathological changes if the oxidative pressure exceeds the cell's antioxidative capacities.

5.1.3 Impact of hypertensive extracellular vesicles

This thesis reveals that hypertensive pdEVs have a specific ability to disrupt pericyte mitochondrial function. This disruption is demonstrated by a decrease in mitochondrial membrane potential, which suggests compromised mitochondrial integrity and function. Mitochondrial dysfunction characterized by augmented electron leakage from the electron transport chain culminates in the generation of reactive oxygen species (ROS), which are closely associated with hypertension, leading to a cycle of ROS-induced cell damage and oxidative stress (201).

In the investigation of the systemic effects of hypertension on vascular cell biology, significant alterations in mitochondrial function were found when control pericytes were exposed to plasma-derived EVs from hypertensive rodents without the presence of other soluble factors or cytokines. This research shows that circulating EVs in hypertensive states have a unique capacity to disrupt cellular bioenergetics that extends beyond plasma interactions with primary vascular compartments. The decrease in mitochondrial membrane potential in response to hypertensive EVs,

but not to plasma alone, highlights the potency and specificity of EVs as carriers of pro-pathogenic signals. This suggests that hypertensive pdEVs have a direct negative impact on mitochondrial integrity and function, which compromises cellular energy production, revealing a novel pathway through which hypertension may cause vascular damage.

These results are particularly interesting considering the well-known role of EVs in facilitating intercellular communication, as well as their capacity to transport a range of bioactive molecules, such as inflammatory mediators, microRNAs, and other non-coding RNAs, which can significantly affect the behavior of recipient cells (99,100).

The capacity of hypertensive EVs to impair mitochondrial function in pericytes may represent a mechanistic pathway through which hypertension exerts systemic effects, leading to the disruption of vascular and potentially neurovascular functions. This interaction points out the broader implications of this findings, linking localized vascular dysfunction to systemic vascular health. In the setting of hypertension, where elevated systemic inflammatory markers are prevalent (12) , the influence of circulating EVs becomes a critical determinant in the perpetuation of vascular pathology. The release of hypertensive EVs by other organs could specifically induce mitochondrial dysfunction in pericytes, which might contribute to the metabolic shifts observed at the level of the BBB, favoring glycolysis over oxidative phosphorylation as a survival strategy in response to altered systemic conditions. Such alterations in the cellular mechanisms governing the NVU in hypertension may lead to pathological changes, affecting cerebral autoregulation, neurovascular coupling, and vasculo-neuronal coupling ultimately contributing to cognitive decline and neurodegenerative diseases (202–204).

5.1.4 Metabolic reprogramming in pericytes

The metabolic requirements of pericytes were investigated revealing that hypertensive pericytes alter their phenotype towards glycolysis to maintain an increased metabolic demand and mitigate oxidative stress, a strategy reminiscent of cancer cells (205,206).

This glycolytic shift in hypertensive pericytes, similar to the Warburg effect seen in cancer cells, suggests that pericytes despite the availability of oxygen, prefer a less efficient pathway to generate ATP to sustain vital functions under stress (113,206). This metabolic reprogramming may be a consequence to support cellular survival, vascular stability and neuronal health, particularly in situations of chronic hypertension. However, unlike tumor cells (206), which leverage this

metabolic shift to support rapid proliferation, pericytes in hypertensive states seem to mainly rely on glycolysis to sustain their essential functions under stress, thereby supporting vascular stability. And while this adaptation might be beneficial for short-term survival, it may lead to long-term cellular exhaustion and vascular dysfunction.

The implications of these findings extend beyond mere cellular survival influencing the entire NVU, contributing to the inflammatory processes frequently observed in chronic hypertension. Pericytes, which are responsible for regulating cerebral blood flow, may lose their ability to do so effectively due to altered signaling pathways mediated by nitric oxide and inflammatory mediators such as TNFα and IL-6, where the chronic activation of this inflammatory cascade disrupts not only pericytes, but also endothelial cells and astrocytes, compounding the deleterious effects on cerebral homeostasis. As a result, the resulting vascular dysfunction can promote or exacerbate neuronal damage. The glycolytic shift in hypertensive pericytes is particularly evident in the context of mitochondrial dysfunction, which persists in late chronic HTN. Despite their glycolytic preference, chronic HTN pericytes struggle to increase energy production under stress due to mitochondrial inefficiencies. This observation suggests that in advanced stages of the disease, hypertensive pericytes operate near their maximal capacity, a critical state that risks compromising their cellular integrity under prolonged or severe stress.

These data demonstrate that while early HTN pericytes retain some ability to utilize mitochondrial pathways for energy production, chronic conditions result in heavy reliance on glycolysis. However, this dependance on glycolysis can contribute to their susceptibility when faced with conditions that limit this energy pathway, indicating a significant shift away from the ability to adapt metabolically. This change in energy utilization points to an adjustment that, while initially compensatory, may become detrimental due to impaired mitochondrial function. The metabolic inflexibility of chronic HTN pericytes could be attributed to saturation of mitochondrial capacity, where the demand for ATP and biosynthetic precursors exceeds the ability of mitochondria to function efficiently. This profound metabolic shift in pericytes may influence their interaction with other NVU components such as endothelial cells, neurons, microglia, and astrocytes, potentially exacerbating inflammatory responses and contributing to vascular leakage and BBB dysfunction (86). The metabolic vulnerability of pericytes demonstrates an important aspect of hypertensive pathology and offers a novel target for therapeutic interventions.

5.1.5 Therapeutic implications

The potential therapeutic targets that arise from the significant metabolic reprogramming and phenotypic changes observed in hypertensive pericytes are to be considered. These strategies can be aimed at restoring the metabolic flexibility of pericytes to enhance mitochondrial function that could mitigate some of the severe complications associated with chronic hypertension. Furthermore, targeting specific pathways identified in our gene expression profiles, such as the renin-angiotensin system or inflammatory mediators, may provide new avenues for therapeutic intervention. These findings illustrate the importance of adopting a comprehensive approach to treating hypertensive vascular diseases, one that takes into account the broad cellular responses and metabolic adaptations of vascular cells.

In conclusion, the findings in this thesis present an extensive assessment of the physiological and cellular responses of vascular cells to chronic arterial hypertension, thereby deepening our understanding on the significant phenotypic and metabolic transformations pericytes undergo in chronic hypertensive states.

By understanding and potentially manipulating these wide-ranging cellular responses, particularly metabolic pathways, through targeted interventions that promote metabolic flexibility, severe complications associated with long-term high blood pressure may be lessened, and cognitive abilities could be preserved. This approach may introduce a new era of treating hypertensive vascular diseases, in which a holistic and metabolic modulation to vascular cells becomes a keystone in therapeutic approaches.

5.2 Microglial response to hypertensive stress

An in-depth examination of microglial reactivity during chronic hypertension was provided in this thesis, expanding our knowledge of microglial dynamics and challenging the simplistic view of uniform microglial activation. The primary objective of this research was to characterize and understand microglial reactivity within the framework of hypertensive cSVD, an area previously unexplored. Here, distinct microglial subpopulations were identified based on surface markers indicative of pro-inflammatory responses, homeostasis maintenance, and repair mechanisms. Rather than viewing microglia as a homogeneous population responding linearly to pathology, these findings reveal a complex landscape where different microglial subpopulations perform

diverse functions. This paradigm shift, similar to recent findings in other diseases (91), enhances our understanding of microglial biology and characterizes the complexity of microglial reactivity that can pave the way for novel therapeutic strategies. Furthermore, microglial changes associated with aging were examined, which is biologically significant given the increasing recognition of aging as a key factor in the development of neurodegenerative diseases. Understanding how microglia adapt to aging and how they respond to additional stressors like chronic arterial HTN is vital for comprehending age-related neurological conditions. This dual focus on aging and hypertension provides a detailed view of microglial dynamics that offers a foundation for future research aimed at mitigating the impact of these factors on brain health.

5.2.1 Microglia heterogeneity in chronic hypertension and its implication for BBB leakage and cerebrovascular remodeling

SHRSP rats develop a vascular risk profile, which comprises arterial hypertension that is sufficient for SHRSP rats to develop spontaneous ischemic lesions between 32w and 36w old (60,134,142). Thus, in order to acquire a cross-sectional perspective of microglia in both the cortex and hippocampus in the context of life-long chronic HTN, the morphological and phenotypic changes of microglia were analyzed at a rodent age of 25 weeks, which corresponds to midlife hypertension, and were compared to those of 34-week-old rodents with early-stage cSVD. The hypothesis was that there is a chronic adaptation of microglia throughout the progression of the disease, as opposed to the sudden brain injury that affects the brain upon induced acute brain injury. In the pursuit to understand the biological implications of microglial reactivity, this study has identified a link between specific microglial reactivity and early BBB breakdown. It was observed that cortex microglia upregulate CD11c and MHCII, while hippocampal microglia upregulate CD11c and CD86 during the early stages of HTN. These surface markers, which are associated with pro-inflammatory microglial responses, suggest that microglia may play a role in initiating BBB breakdown. The mechanism likely involves the pro-inflammatory state of adjacent microglia, which enhances the significant transmigration of leukocytes observed in both hippocampal and cortical regions. The influx of these immune cells amplifies the overall inflammatory response, further contributing to BBB vulnerability. Although definitive causation cannot be established at this point, the correlation between microglial activation and BBB leaks provides a compelling explanation for the development of vascular cognitive impairment. This finding lays the groundwork for future investigations that will focus on targeting specific microglial subsets to mitigate BBB permeability and neuroinflammation.

Microglia, characterized by their heterogeneity, exhibit significant diversity under pathological conditions (81,91). In this study, chronic hypertension was associated with a variety of phenotypical characteristics. Notably, an overexpression of the P2Y12 receptor (P2Y12R) was found, potentially influencing chemotactic and phagocytic microglial activities. Previous studies have demonstrated that the microglial response to capillary lesions relies on P2Y12R for BBB repair (93,94). Additionally, P2Y12R accumulation at endothelial contacts is essential for vasodilation, and its focal loss has been linked to synaptic degeneration, emphasizing the connection between vascular inflammation and neural dysfunction (92).

Microglia can exist in various reactive states, including primed and senescent states. These analyses revealed two distinct microglial states related to chronic hypertension, each contributing to neuroinflammatory signals. Microglia that exhibit pro-inflammatory characteristics undergo morphological changes and secrete cytokines, causing significant damage to the vasculature and the neuronal tissues (207,208). The resulting reactive microglial phenotype observed in early chronic HTN could either be a cause or a result from the significant BBB disturbances observed. On one hand, the elevated expression of P2Y12R in chronic HTN may prompt microglial migration to vascular sites, leading to classical microglial pro-inflammatory activation, modulating its cytoskeletal network for phagocytosis, and subsequent vessel wall remodeling, thereby disturbing the BBB allowing the ingress of leukocytes into the CNS, which perpetuates microglial activation (209). On the other hand, increased leukocyte adhesion and vessel wall remodeling due to systemic hypertension-induced inflammation might trigger a resolving microglial activation pattern that aids in BBB repair. These findings illustrate the important role of microglia reactivity towards BBB disturbances and cerebrovascular remodeling in chronic HTN, as they can exacerbate vascular injury, lead to perivascular cell reactivity, and ultimately affecting glymphatic clearance and protein deposit removal around the NVU.

5.2.2 Implications of altered microglia morphological features in hypertensive cSVD

Microglia in both the hippocampus and cortex exhibit notable morphological changes under hypertensive conditions. These changes included increased somatic area and ramification complexity, indicative of an activated state. The presence of larger, more complex microglia suggests heightened reactivity and a potential role in exacerbating vascular and neuronal damage. These morphological changes are consistent with increased microglial activation and may reflect adaptive responses to prolonged hypertension.

This study identified distinctive microglial characteristics within the context of hypertensive cSVD. Specifically, an increased presence of microglia with thicker processes, enlarged somata, a decreased ramification index, and a higher association with the vasculature. These morphological changes suggest a functional shift in microglia, potentially linked to metabolic alterations and their ability to respond to vascular disturbances (88,209,210). While previous studies have noted amoeboid microglia in the white matter in response to HTN (211), our findings in the gray matter highlight potential regional differences in microglial reactivity, at least specific to hypertensive cSVD. Various rodent models of hypertension have consistently shown increased microglial cell volume and complexity in the gray matter (146). In our rodent model, we observed enlarged microglial somata and increased ramification complexity in the gray matter. The enlarged somata and microglial association to the vasculature were morphological features already present at the early stage of chronic HTN, whereas the increased ramification complexity appeared during the late stage of chronic HTN. These changes could impact the glymphatic clearance system, contributing to neurovascular injury. Previous research has indicated that brain tissue surrounding blood vessels in patients with cSVD is affected even before the emergence of lesions such as microbleeds or lacunar strokes (16,141,212). These changes surrounding small brain capillaries can lead to a loss of vascular contractibility, resulting in an inability to meet the high metabolic demands of the aging brain. Evidence suggests that preexisting hypertension exacerbates secondary neurodegeneration beyond its immediate impact on neurovascular injury (12,213). These findings emphasize the importance of managing vascular risk factors and midlife hypertension to preserve vascular and brain health homeostasis in older age.

5.2.3 Revealing the vulnerability of the hippocampus in hypertensive cSVD

Our investigation highlights the susceptibility of the hippocampus in hypertensive cSVD. It is well-documented that cognitive decline linked to cSVD frequently involves memory issues and cortical symptoms, such as executive dysfunction and attention deficits (214). Recent research has shown that age-related BBB disruption in the hippocampus occurs early in the aging human brain, particularly in cases of mild cognitive impairment (215). This early BBB leakage could provide insights into similar pathological processes in hypertensive cSVD. Additionally, cardiovascular risk factors are known to affect memory function through white matter hyperintensities (13), potentially increasing the vulnerability of various brain regions to the combined effects of aging and hypertension (216). Thus, it is reasonable to hypothesize that hypertensive cSVD might exhibit similar occurrences.

The results showed that already in early chronic HTN, resembling midlife human chronic HTN, hippocampal microglia portrayed a highly dynamic contrasting phenotype. For instance, pro-inflammatory phenotype evidenced by upregulation of CD11b/c and CD86 and on the other, an anti-inflammatory and chemotactic response by P2Y12 and CD200r upregulation. In midlife hypertensive cortex however, the overall microglia activation was polarized to its pro-inflammatory pathway shown by increased expression of CD11b/c and RT1B (MHC-II). A strong expression of RT1B (MHC-II) microglia may precede its final differentiation into disease associated microglia (DAMs) identified seemingly different by sc-RNA-seq (217). Pro-inflammatory microglia polarization is characterized by morphological changes and secretion of cytokines which may cause vascular and neuronal damage due to a prolonged exposure to pro-inflammatory mediators (207,208). These findings suggest a delicate balance between inflammation and protection in response to early BBB leaks (218,219).

It is well-established that the hippocampus is affected in both experimental (220,221) and clinical cSVD(222), directly contributing to the development of vascular cognitive impairment. Moreover, blood pressure (BP) management significantly impacts cognitive function. For instance, studies have shown that BP reduction through medications like amlodipine can improve memory impairment associated with hypertension (223). Consistent with these memory improvements, amlodipine has been found to reduce microglial activation, suggesting a link between microglial reactivity and cognitive function. These findings underscore the need for further exploration into the direct association between hypertension, microglial alterations, and cognitive decline. However, our study design did not address the complex effects of late-life hypertension on the aging brain which are rather complex (224), necessitating further research.

Aligning with current perspectives (17), this research enhances the understanding of early changes that precede or follow the development of brain arteriolosclerosis (B-ASC) in the context of hypertension. Our data support the interlinkage between hypertension, vessel wall alterations, and neuroinflammation, as highlighted by recent reviews (17,61). This study extends this understanding by offering a detailed profile of dynamic, region-specific neuroinflammatory responses and microglial phenotypes. By examining microglial phenotypical changes during the early phases of hypertension, we provide valuable insights into the neuroinflammatory aspects of microvascular disease. Additionally, our findings can aid in the classification of cSVD subtypes and contribute to the development of targeted therapies, emphasizing the importance of identifying early targets to

potentially prevent or manage advanced B-ASC stages. This deeper understanding of microglial heterogeneity and dynamics in hypertensive states may have significant implications for future therapeutic strategies and personalized medicine in cSVD.

5.2.4 Age-dependent and pathological changes in cortical microglia marker expression profile suggest microglia reactivity and primed states in chronic hypertension

The interplay between vascular inflammation, arterial function, and age-related diseases is complex and multifaceted (61). Chronic hypertension has been shown to cause age-dependent and pathological changes in cortical microglia. These changes suggest that microglia reactivity and primed states are critical for the regulation of anti-inflammatory signals. The dysfunction in the CD200-CD200R system, in particular, is commonly associated with aging brains (225). The upregulation of the inhibitory immune receptor CD200R with aging in Ctrl, whereas a significant reduction in late chronic hypertensive brains was observed, suggest an inefficient regulation of age-related pro-inflammatory conditions in HTN brains that can lead to deficient feedback loops in the induction of inflammatory mechanisms. These mechanisms can contribute to vascular inflammation and neurodegeneration (226–229). Our results point to a dysfunction in the CD200-CD200R system, which is necessary for the activation of anti-inflammatory signals supported by previous findings where a significant decrease in CD200R mRNA expression by microglia in hippocampus was found in brains of AD patients (225).

During the aging process, significant changes occur in the CNS immune repertoire that have been identified through high-dimensional analyses (230,231). Our hypothesis is that in subjects with hypertension, there is early regional microglia activation surrounding the brain's smallest capillaries, which polarizes subpopulations of microglia towards a pro-inflammatory phenotype. In late-stage hypertension, there is a persistent increase in anti-inflammatory microglia clusters, which could reflect a compensation mechanism to reduce local neuroinflammation. However, if this neuroinflammation is not reduced, it can lead to chronic microglia activation and self-perpetuating damage to neural tissue. The 'primed' microglia profile, which is a result of normal aging, triggers prolonged neuroinflammatory responses that alter neuro-immune communication and increase the risk of co-morbidities such as depression, cognitive impairment, and dementia (232–235).

While the hippocampus and cortex exhibit distinctive microglia cluster compositions, the larger size of the cortex suggests a greater spatial and functional complexity, potentially requiring a more

diverse array of microglia subpopulations. Future research could benefit from spatial proteomics analysis or multiple-target immunohistochemistry.

5.2.5 Microglial heterogeneity and subpopulations

Our analysis identified distinct microglial subpopulations and heterogeneity with unique phenotypic profiles that emerge under chronic HTN.

Hippocampal microglial subpopulations

Early chronic HTN in the hippocampus led to the identification of distinct microglial subpopulations that expressed specific surface marker expressions. UMAP analysis, along with automated clustering, revealed unique clusters, particularly cluster 3 (C3), which expressed CD86, CD11b/c, and CD163 exclusively in early chronic HTN. This cluster likely represents a reactive microglial population that responds to early vascular perturbations and BBB disruption. The data obtained from cluster 2 (C2) in the HTN group revealed an increase in the expression of P2Y12R and CX3CR1 when compared to normotensive Ctrl. This heightened expression suggests an enhanced chemotactic and surveillance activity, which may serve as a compensatory mechanism to maintain homeostasis in response to the initial hypertensive insults. On the other hand, aged Ctrl demonstrated the presence of a subpopulation, cluster 4 (C4), which was absent in late HTN and comprised a substantial portion of the microglial population. The disappearance of this cluster in hypertensive states highlights the impact of prolonged HTN on the diversity and function of microglia. In the later stages of chronic HTN, a notable change was observed from cluster 1 (C1) to a higher presence in cluster 2 (C2), which displayed increased expressions of CD200R, CD45, CD163, MHC-II, CD11b/c, and P2Y12R. This shift indicates a progression towards a more reactive state, suggesting ongoing adaptation and possibly the exhaustion of homeostatic mechanisms in response to prolonged hypertensive stress.

Cortical microglial subpopulations

The cortex demonstrated a highly complex pattern of microglial heterogeneity in early chronic HTN. The analysis revealed six clusters in Ctrl brains, while only five were present in HTN brains. It is important to note that cluster 5 (C5), which expressed CD45, CD11b/c, P2Y12R, CD200R, and MHC-II, was absent in HTN brains. This absence could signify the potential vulnerability or loss of a specific microglial phenotype due to the HTN conditions. In late-stage chronic HTN, an increase was observed in the number of microglial clusters. HTN brains showed seven distinct clusters, whereas Ctrl brains showed only five. This increased complexity highlights the extensive

reorganization of microglial populations in response to prolonged HTN. Cluster 3 (C3), which was marked by elevated levels of CD200R, CX3CR1, CD163, MHC-II, and CD11b/c, displayed higher reactivity and an intensified inflammatory and surveillance role. Additionally, the emergence of clusters 5 (C5) and C7 in late HTN, which were absent in Ctrl, further emphasizes the adaptive yet potentially maladaptive responses of microglia to chronic vascular stress. Cluster 7 (C7) exhibited particularly high levels of CD200R, CD45, CD163, MHC-II, CD11b/c, P2Y12R, and CX3CR1, indicating a highly reactive and multifunctional phenotype. The variations in phenotype between early and late stages of HTN in both the hippocampus and cortex illustrate the plasticity and heterogeneity of microglia, which are driven by the intricate interplay between aging and HTN, and that may play specialized roles in the pathogenesis of cSVD contributing to the complexity of neuroinflammatory responses.

5.2.6 Distinct microglial morphological features in human hypertensive cSVD

Extending our investigation to human subjects allowed us to validate and compare our findings from the SHRSP model to the human context of hypertensive cSVD. Similar morphological changes between humans and rodents were discovered, with the findings suggesting that alterations in microglial morphology, characterized by amplified somata and changes in the ramification index, denote a transition in microglial function (88,209,210). In post-mortem brain tissue samples from elderly individuals diagnosed with hypertensive cSVD, significant changes in microglial morphology and density were observed, which were consistent with the patterns observed in the SHRSP model. In particular, our analysis revealed a marked increase in the density of $IBA1^+$ microglia per mm^2 in the cingulate cortex of cSVD patients compared to age-matched controls. This increased microglial density indicates an activated microglial state, which may contribute to the observed vascular and neural pathologies. Additionally, the total number of vascular-associated microglia (VAMs) were measured and this analysis revealed an increase in their density relative to the total number of $IBA1^+$ cells in individuals with cSVD as compared to controls. This finding emphasizes the significance of microglia in vascular surveillance and suggests their potential involvement in the pathology of cSVD. The increased presence of VAMs could signify a response to vascular damage, BBB disruption, or ongoing neuroinflammatory processes in cSVD.

A detailed morphological examination of individual microglial cells in the cingulate cortex of cSVD patients revealed that in cSVD cases, microglia displayed a significantly larger somatic area compared to controls. This enlargement of the soma is indicative of an activated state, suggesting

that these cells are responding to a pathological environment by either engaging in phagocytosis or by having diminished phagocytic capabilities, resulting in their enlargement. Our results revealed that there is a significant difference in the size and shape of microglial cells in cases of cSVD compared to age-matched controls. Specifically, we observed enlarged soma and elongated, thickened processes, which may indicate a reactive response of microglia to the presence of cSVD and a potential disruption in their metabolic activity. However, our findings differ from those of a recent autopsy study that focused on the white matter and reported the presence of ameboid microglia in response to hypertension (211). This observation emphasizes the possibility of regional differences between white and grey matter in microglial reactivity. To our knowledge, no study has explored microglia morphology in human grey matter during hypertensive cSVD. Multiple rodent models of hypertension have consistently demonstrated an expansion in microglial somata, accompanied by enhanced microglia branching in grey matter tissue (146). These morphological modifications were linked to elevated levels of CD11b, which is a marker of microglial reactivity. Furthermore, these changes demonstrated the potential for reversal through the use of anti-hypertensive medications, such as amlodipine (223). Morphological modifications may suggest that microglia's capabilities to efficiently carry out phagocytosis or manage the accumulation of debris and cellular waste from chronic HTN and vascular damage have been compromised. Furthermore, the study revealed an increase in the phagolysosomal marker CD68 in microglia from HTN mice. However, it is crucial to recognize that an elevation of the CD68 marker does not necessarily indicate an improvement in phagocytic functions. Instead, it could signify an increase in the engulfment of lysosomal structures or a decrease in clearance rate, which would slow down microglial catabolism. Consequently, it is plausible that the observed increase in soma size and thickened processes during chronic HTN conditions might be related to potential metabolic changes, leading to the distinct morphological features observed. Moreover, our observations revealed a trend towards an increase in branching complexity in cSVD microglia, and a significantly reduced ramification index. This finding, which appears paradoxical at first glance, suggests that although microglia extend more processes in an effort to monitor and respond to their environment, these processes are less complex and potentially less effective in maintaining homeostasis. This alteration in morphology may have an impact on the glymphatic clearance system, ultimately leading to neurovascular injury and impaired clearance of metabolic waste. Therefore, while some studies have reported amoeboid microglia on white matter in response to hypertension, our observations in the gray matter of the cingulate cortex differ, suggesting that

microglial responses vary significantly between brain regions. These regional differences delineate the importance of considering the specific microenvironment and local vascular conditions when studying microglial behavior. The morphological changes observed in microglia in cSVD patients, such as an increase in soma size and altered branching patterns, align with the findings from the SHRSP model, providing a validation for our preclinical results. These modifications may impact the capacity of microglia to interact with other cells within the NVU and affect their role in preserving BBB integrity and facilitating immune responses.

5.3 Proposed role of Pericyte-Microglia lactate shuttle in hypertensive cerebral small vessel disease

The research presented in this dissertation illustrates the potential metabolic interplay between pericytes and microglia within the context of hypertensive cSVD. Under hypertensive conditions, it is now known that pericytes undergo glycolytic reprogramming, resulting in increased lactate production. This lactate is hypothesized to be transferred to adjacent microglia, particularly those associated with the vasculature via the recently described receptor on microglia, the monocarboxylate transporter 4 (MCT4) receptor (236,237). This proposed pericyte-microglia lactate shuttle offers a novel mechanism of cellular interaction that may be pivotal in understanding the metabolic dynamics in hypertensive cSVD.

Lactate has long transitioned from being considered a mere waste product to being recognized as a vital brain metabolite involved in numerous cellular processes (reviewed in (237)). This recognition is well illustrated by the astrocyte-neuron lactate shuttle, where astrocytes produce lactate that neurons subsequently uptake via MCTs (238). This lactate then serves as a source of energy for OxPhos and other crucial metabolic pathways that ensure microglial survival and preserve synaptic plasticity and neuronal function (239). This mechanism reinforces the hypothesis that lactate serves as both a bioenergetic substrate and signaling molecules across various brain cells.

Microglia exhibit a remarkable capacity for metabolic flexibility, which allows them to participate actively in various biological processes, including blood vessel sprouting, neural precursor cell regulation, synapse formation and elimination, and the continuous surveillance of brain parenchyma (240,241). Given the demanding nature of their constant motility and phagocytic activities, it is plausible that they require sustained ATP levels to support these functions. They can utilize lactate to meet their energy requirements, particularly under conditions of metabolic stress or inflammation. It has recently been shown that microglia express key enzymes and transporters

necessary for lactate metabolism, including MCT1 and MCT4, which facilitate lactate import, and lactate dehydrogenase B (LDHB), which converts lactate to pyruvate, thus fueling the tricarboxylic acid (TCA) cycle (236). This recent study demonstrated that lactate can modulate several microglial functions, including proliferation, migration, and phagocytosis. *In vitro* experiments have shown that microglia can utilize lactate to support their energy needs and regulate their inflammatory responses (239,242,243). This metabolic reprogramming is vital for microglial function during neuroinflammation and repair processes, suggesting that lactate could play a significant role in microglial activation and response during hypertensive cSVD.

Given the critical role of pericytes in maintaining BBB integrity and their ability to produce lactate under stress conditions, it is plausible to propose a pericyte-microglia lactate shuttle. In this theoretical model, pericytes under hypertensive stress increase their glycolytic activity, resulting in increased lactate production. This lactate is subsequently taken up by microglia via the MCT4 transporter potentially fueling their energy demands. This mechanism can be particularly relevant during the chronic low-grade inflammation characteristic of hypertensive cSVD.

6 Conclusions

The present dissertation provided a comprehensive investigation of the consequences of persistent hypertension on cerebral pericytes and microglia, two essential components of the NVU. This thesis aimed to characterize the phenotypic and metabolic modifications that pericytes undergo during hypertensive states by employing the SHRSP rodent model. Additionally, by utilizing both the SHRSP model and human post-mortem brain tissue, the dynamic nature of microglia in the context of hypertensive cSVD was investigated, thereby demonstrating the complex interplay between vascular and immune responses in the context of hypertensive cSVD.

The gene expression analysis revealed an upregulation of genes that play a crucial role in lipid metabolism, angiogenesis, and inflammatory responses during the early stages of chronic HTN, indicating an active process of vascular remodeling. As HTN progressed to its late chronic stages, there was a noticeable decrease in the expression of these genes, suggesting a potential exhaustion of metabolic and adaptive capacities. Furthermore, pericytes exhibited substantial phenotypic and metabolic reprogramming under hypertensive conditions. Plasma-derived EVs from HTN rodents significantly impaired mitochondrial function in Ctrl pericytes, demonstrating the strong influence of these EVs as biomarkers and as active participants in the exacerbation of vascular pathology across the NVU. These findings corroborate the potential of targeting EVs and metabolic pathways in therapeutic strategies to mitigate the vascular complications associated with chronic hypertension.

In the context of chronic HTN, microglia displayed a range of phenotypic characteristics and subpopulations. This thesis identified specific microglial subpopulations based on surface markers indicative of pro-inflammatory responses, homeostasis maintenance, and repair functions. These findings demonstrate the dynamic nature of microglia in the context of hypertensive cSVD and illustrate the various stages of phenotypic adaptation in the hippocampus and cortex during two chronic hypertensive states. These findings also support the notion that the combination of endothelial alterations during early chronic HTN, coupled with microglial reactivity and the influence of aging, shapes a synergistic relationship that may contribute to the development of cSVD. This research has revealed that chronic HTN induces microglial morphological changes, modifies BBB permissiveness, and promotes neuroinflammation, potentially priming the brain for injury. The presence of systemic inflammation has been documented in the pathogenesis of hypertension, but it remains unclear whether the observed CNS inflammation and overreacting

microglia in chronic HTN are a cause or consequence of cSVD pathogenesis. Notably, a higher percentage of microglia were found in close contact with blood vessels, suggesting a shift in phenotype towards constant vascular support or damage perpetuation.

The research presented in this dissertation focuses on the potential metabolic interplay between pericytes and microglia in hypertensive cSVD. Under hypertensive conditions, pericytes increased glycolysis, producing lactate, which can potentially be transferred to microglia via the MCT4 receptor. This proposed lactate shuttle between pericytes and microglia presents a novel mechanism of cellular interaction and is vital for understanding the metabolic processes in hypertensive cSVD. Given pericytes' role in maintaining the integrity of the BBB and their ability to produce lactate under stress, the pericyte-microglia lactate shuttle is a promising model to study further metabolic changes during the progression of hypertensive cSVD. Future research should focus on validating this mechanism and exploring therapeutic interventions that target metabolic pathways in cSVD.

7 Future directions

Future research should focus on clarifying the molecular mechanisms that govern the phenotypic and metabolic transformation of pericytes and microglia during chronic HTN. Utilizing advanced techniques such as single-cell RNA sequencing of pericytes and spatial transcriptomics can offer profound information into the specific genetic changes and cellular interactions that drive these processes. The considerable influence of plasma-derived EVs on pericyte function emphasizes their potential as biomarkers and therapeutic targets. Future research should focus on identifying the particular cargo within EVs that contributes to vascular pathology, as well as investigating the potential protective or restorative effect of non-pathological EVs on damaged cells. Interventions aimed at modulating EV release or altering their content may offer novel approaches to prevent or lessen vascular damage in hypertension.

The discovery of distinct microglial subtypes with varying functions in regulating inflammation, maintaining homeostasis, and repair offers promising prospects for personalized therapies. Further research should focus on developing methods to specifically target and modulate specific microglial subtypes to increase their beneficial effects while limiting their involvement in neuroinflammation and barrier disruption. This could involve the therapeutic application of EVs, gene therapy, or cell-based interventions.

Future research should also focus on validating the proposed pericyte-microglia lactate shuttle and exploring its implications for therapeutic interventions targeting metabolic pathways in cSVD. This mechanism, where pericytes under hypertensive stress increase their glycolytic activity and produce lactate, which is then taken up by microglia via the MCT4 transporter, could be pivotal in understanding the metabolic dynamics in hypertensive cSVD. Investigating this lactate shuttle in more detail could provide new insights into cellular interactions and metabolic regulation within the NVU during hypertensive cSVD.

To effectively transfer the results from the SHRSP model to clinical practice it is necessary to conduct longitudinal studies in humans. These studies should aim to correlate alterations in pericyte density and phenotype to clinical symptomatology in patients with chronic hypertension and cSVD. Utilizing non-invasive imaging methods, such as advanced MRI, in conjunction with cerebrospinal fluid and blood biomarkers specifically derived from cerebral pericytes, could aid in tracking these cellular changes over an extended period of time.

The significance of our study findings indicates the necessity of intervening early in hypertension progression to prevent or delay the advancement of cSVD and its associated vascular cognitive decline. Potential interventions may comprise pharmacological agents that target specific molecular pathways identified in our research, including inhibitors of the renin-angiotensin system, anti-inflammatory agents, or metabolic modulators. Furthermore, it is important to explore lifestyle modifications, such as diet and exercise, which have been demonstrated to affect vascular health, as complementary approaches. Considering the diverse reactions exhibited by microglia and pericytes in response to chronic hypertension, the implementation of personalized medicine approaches should be considered. By conducting genetic profiling of patients, it may be possible to identify those who are at a greater risk for vascular complications and subsequently guide the selection of customized therapeutic approaches. Additionally, the utilization of patient-specific induced pluripotent stem cells could facilitate the modeling of individual responses of the vasculature to hypertension, thus enabling the testing of potential interventions in a personalized manner.

In summary, the results of this dissertation indicate the potential to apply preclinical findings to a clinical setting. By utilizing molecular and cellular markers identified in these studies, early and targeted interventions may be able to delay or prevent the progression of cSVD and its accompanying cognitive sequelae. Implementing personalized medicine strategies, which incorporate genetic and phenotypic profiling, could further improve the effectiveness of these interventions by customizing them to the unique needs of individual patients. Ultimately, this thesis builds up our scientific comprehension of hypertensive cSVD and lays the groundwork for pioneering clinical approaches that could substantially improve patient outcomes. By bridging the gap from bench to bedside, we move closer to a future where the devastating effects of chronic hypertensive vascular disease on the brain can effectively be managed and mitigated.

8 Strengths and limitations

In this thesis the metabolic reprogramming and phenotypic shifts of cerebral pericytes in response to chronic arterial hypertension was demonstrated, offering valuable insights into hypertensive vascular pathology. This study advances our understanding of hypertensive vascular pathology by demonstrating how metabolic inflexibility and mitochondrial dysfunction in cerebral pericytes contribute to cerebrovascular disease progression. The contribution of these results is significant because it offers a novel insight into the pathophysiology of cSVD and points towards metabolic modulation as a promising therapeutic approach. Furthermore, these findings highlight the role of EVs in pericyte dysfunction, emphasizing their potential as biomarkers and therapeutic targets, adding a valuable dimension to our understanding of vascular pathology in chronic arterial hypertension. Moreover, microglia heterogeneity was characterized by incorporating high-resolution morphological variables and single-cell surface protein phenotypic characterization. By employing both supervised and unsupervised analyses, this research examined the dynamic changes of the microglia landscape in the hippocampus and cortex of Wistar and SHRSP rats, which to our knowledge, this methodology filled a gap in the current literature regarding the effects of chronic arterial hypertension on microglia phenotype. These findings provide evidence of the diversity within microglia sub-populations and confirmed a spectrum of microglia phenotypes explicitly associated with chronic arterial hypertension.

Despite the strengths, our study has certain limitations. The reliance on the SHRSP rat model, while invaluable, may not fully capture the complexity of human pathology due to species-specific differences. The exclusive focus on pericytes and EVs, although detailed, did not account for broader cellular interactions within the NVU, potentially overlooking other critical mechanisms influencing disease progression. The *in vitro* conditions used to study pericytes may not entirely replicate the *in vivo* microenvironment, possibly oversimplifying the interactions between pericytes and other cellular components. The relatively small sample size of human post-mortem tissue limits the generalizability of our findings, although obtaining larger sample sizes in this specific population is challenging. Furthermore, our study did not include functional assessments of microglia, focusing primarily on phenotypical changes. Future studies should aim to characterize the functional implications of these alterations in the context of cSVD. Despite these limitations, our study advances the understanding of hypertensive vascular pathology and suggests metabolic modulation as a promising therapeutic strategy.

References

1. James PA, Oparil S, Carter BL, Cushman WC, Dennison-Himmelfarb C, Handler J, et al. 2014 Evidence-based guideline for the management of high blood pressure in adults: Report from the panel members appointed to the Eighth Joint National Committee (JNC 8). Vol. 311, JAMA. American Medical Association; 2014. p. 507–20.

2. Palta P, Albert MS, Gottesman RF. Heart health meets cognitive health: evidence on the role of blood pressure [Internet]. Vol. 20, www.thelancet.com/neurology. 2021. Available from: www.thelancet.com/neurology

3. Iadecola C, Duering M, Hachinski V, Joutel A, Pendlebury ST, Schneider JA, et al. Vascular Cognitive Impairment and Dementia: JACC Scientific Expert Panel. Vol. 73, Journal of the American College of Cardiology. Elsevier USA; 2019. p. 3326–44.

4. Livingston G, Huntley J, Sommerlad A, Ames D, Ballard C, Banerjee S, et al. Dementia prevention, intervention, and care: 2020 report of the Lancet Commission. Vol. 396, The Lancet. Lancet Publishing Group; 2020. p. 413–46.

5. Cai Z, Wang C, He W, Tu H, Tang Z, Xiao M, et al. Cerebral small vessel disease and Alzheimer's disease. Vol. 10, Clinical Interventions in Aging. Dove Medical Press Ltd.; 2015. p. 1695–704.

6. Wardlaw JM, Smith C, Dichgans M. Small vessel disease: mechanisms and clinical implications. Vol. 18, The Lancet Neurology. Lancet Publishing Group; 2019. p. 684–96.

7. Pantoni L. Cerebral small vessel disease: from pathogenesis and clinical characteristics to therapeutic challenges. Vol. 9, The Lancet Neurology. 2010. p. 689–701.

8. Li C, Zhu Y, Ma Y, Hua R, Zhong B, Xie W. Association of Cumulative Blood Pressure With Cognitive Decline, Dementia, and Mortality. J Am Coll Cardiol. 2022 Apr 12;79(14):1321–35.

9. Rensma SP, van Sloten TT, Launer LJ, Stehouwer CDA. Cerebral small vessel disease and risk of incident stroke, dementia and depression, and all-cause mortality: A systematic review and

meta-analysis. Vol. 90, Neuroscience and Biobehavioral Reviews. Elsevier Ltd; 2018. p. 164–73.

10. Wardlaw JM, Doubal F, Armitage P, Chappell F, Carpenter T, Muñoz Maniega S, et al. Lacunar stroke is associated with diffuse Blood-Brain barrier dysfunction. Ann Neurol. 2009 Feb;65(2):194–202.

11. Dupré N, Drieu A, Joutel A. Pathophysiology of cerebral small vessel disease: a journey through recent discoveries. Journal of Clinical Investigation [Internet]. 2024 May 15;134(10). Available from: https://www.jci.org/articles/view/172841

12. Ungvari Z, Toth P, Tarantini S, Prodan CI, Sorond F, Merkely B, et al. Hypertension-induced cognitive impairment: from pathophysiology to public health. Vol. 17, Nature Reviews Nephrology. Nature Research; 2021. p. 639–54.

13. Low A, Mak E, Rowe JB, Markus HS, O'Brien JT. Inflammation and cerebral small vessel disease: A systematic review. Ageing Res Rev. 2019 Aug;53:100916.

14. Zhang CE, Wong SM, Uiterwijk R, Backes WH, Jansen JFA, Jeukens CRLPN, et al. Blood–brain barrier leakage in relation to white matter hyperintensity volume and cognition in small vessel disease and normal aging. Brain Imaging Behav. 2019 Apr 15;13(2):389–95.

15. Taheri S, Gasparovic C, Huisa BN, Adair JC, Edmonds E, Prestopnik J, et al. Blood-brain barrier permeability abnormalities in vascular cognitive impairment. Stroke. 2011 Aug;42(8):2158–63.

16. Walsh J, Tozer DJ, Sari H, Hong YT, Drazyk A, Williams G, et al. Microglial activation and blood-brain barrier permeability in cerebral small vessel disease. Brain. 2021 May 1;144(5):1361–71.

17. Blevins BL, Vinters H V., Love S, Wilcock DM, Grinberg LT, Schneider JA, et al. Brain arteriolosclerosis. Vol. 141, Acta Neuropathologica. Springer Science and Business Media Deutschland GmbH; 2021.

18. Wilson DM, Cookson MR, Van Den Bosch L, Zetterberg H, Holtzman DM, Dewachter I. Hallmarks of

neurodegenerative diseases. Vol. 186, Cell. Elsevier B.V.; 2023. p. 693–714.

19. Jandke S, Garz C, Schwanke D, Sendtner M, Heinze HJ, Carare RO, et al. The association between hypertensive arteriopathy and cerebral amyloid angiopathy in spontaneously hypertensive stroke-prone rats. Brain Pathology. 2018 Nov 1;28(6):844–59.

20. Mestre H, Tithof J, Du T, Song W, Peng W, Sweeney AM, et al. Flow of cerebrospinal fluid is driven by arterial pulsations and is reduced in hypertension. Nat Commun. 2018 Dec 1;9(1).

21. Sweeney MD, Montagne A, Sagare AP, Nation DA, Schneider LS, Chui HC, et al. Vascular dysfunction—The disregarded partner of Alzheimer's disease. Vol. 15, Alzheimer's and Dementia. Elsevier Inc.; 2019. p. 158–67.

22. Shajahan S, Peters R, Carcel C, Woodward M, Harris K, Anderson CS. Hypertension and Mild Cognitive Impairment: State-of-the-Art Review. Am J Hypertens. 2024 Jan 12;

23. Lecordier S, Manrique-Castano D, El Moghrabi Y, ElAli A. Neurovascular Alterations in Vascular Dementia: Emphasis on Risk Factors. Vol. 13, Frontiers in Aging Neuroscience. Frontiers Media S.A.; 2021.

24. Low A, Mak E, Rowe JB, Markus HS, O'Brien JT. Inflammation and cerebral small vessel disease: A systematic review. Ageing Res Rev. 2019 Aug;53:100916.

25. Iadecola C. The Neurovascular Unit Coming of Age: A Journey through Neurovascular Coupling in Health and Disease. Vol. 96, Neuron. Cell Press; 2017. p. 17–42.

26. Attwell D, Buchan AM, Charpak S, Lauritzen M, MacVicar BA, Newman EA. Glial and neuronal control of brain blood flow. Vol. 468, Nature. 2010. p. 232–43.

27. Presa JL, Saravia F, Bagi Z, Filosa JA. Vasculo-Neuronal Coupling and Neurovascular Coupling at the Neurovascular Unit: Impact of Hypertension. Vol. 11, Frontiers in Physiology. Frontiers Media S.A.; 2020.

28. Yang AC, Vest RT, Kern F, Lee DP, Agam M, Maat CA, et al. A human brain vascular atlas reveals diverse mediators of Alzheimer's risk. Nature. 2022 Mar 31;603(7903):885–92.

29. Obermeier B, Daneman R, Ransohoff RM. Development, maintenance and disruption of the blood-brain barrier. Vol. 19, Nature Medicine. 2013. p. 1584–96.

30. Knox EG, Aburto MR, Clarke G, Cryan JF, O'Driscoll CM. The blood-brain barrier in aging and neurodegeneration. Vol. 27, Molecular Psychiatry. Springer Nature; 2022. p. 2659–73.

31. Sweeney MD, Kisler K, Montagne A, Toga AW, Zlokovic B V. The role of brain vasculature in neurodegenerative disorders. Vol. 21, Nature Neuroscience. Nature Publishing Group; 2018. p. 1318–31.

32. Zlokovic B V. The Blood-Brain Barrier in Health and Chronic Neurodegenerative Disorders. Vol. 57, Neuron. 2008. p. 178–201.

33. Armulik A, Genové G, Mäe M, Nisancioglu MH, Wallgard E, Niaudet C, et al. Pericytes regulate the blood-brain barrier. Nature. 2010 Nov 25;468(7323):557–61.

34. Daneman R, Zhou L, Kebede AA, Barres BA. Pericytes are required for blood-brain barrier integrity during embryogenesis. Nature. 2010 Nov 25;468(7323):562–6.

35. Hartmann DA, Underly RG, Grant RI, Watson AN, Lindner V, Shih AY. Pericyte structure and distribution in the cerebral cortex revealed by high-resolution imaging of transgenic mice. Neurophotonics. 2015 May 27;2(4):041402.

36. Bergers G, Song S. The role of pericytes in blood-vessel formation and maintenance. Vol. 7, Neuro-Oncology. 2005. p. 452–64.

37. Armulik A, Genové G, Betsholtz C. Pericytes: Developmental, Physiological, and Pathological Perspectives, Problems, and Promises. Vol. 21, Developmental Cell. 2011. p. 193–215.

38. Winkler EA, Bell RD, Zlokovic B V. Central nervous system pericytes in health and disease. Vol. 14, Nature Neuroscience. 2011. p. 1398–405.

39. Sweeney MD, Ayyadurai S, Zlokovic B V. Pericytes of the neurovascular unit: Key functions and signaling pathways. Vol. 19, Nature Neuroscience. Nature Publishing Group; 2016. p. 771–83.

40. Bell RD, Winkler EA, Sagare AP, Singh I, LaRue B, Deane R, et al. Pericytes Control Key Neurovascular Functions and Neuronal Phenotype in the Adult Brain and during Brain Aging. Neuron. 2010 Nov 4;68(3):409–27.

41. Eilken HM, Diéguez-Hurtado R, Schmidt I, Nakayama M, Jeong HW, Arf H, et al. Pericytes regulate VEGF-induced endothelial sprouting through VEGFR1. Nat Commun. 2017 Dec 1;8(1).

42. Rustenhoven J, Jansson D, Smyth LC, Dragunow M. Brain Pericytes As Mediators of Neuroinflammation. Vol. 38, Trends in Pharmacological Sciences. Elsevier Ltd; 2017. p. 291–304.

43. Longden TA, Zhao G, Hariharan A, Lederer WJ. Pericytes and the Control of Blood Flow in Brain and Heart. Vol. 85, Annual Review of Physiology. Annual Reviews Inc.; 2023. p. 137–64.

44. Hariharan A, Robertson CD, Garcia DCG, Longden TA. Brain capillary pericytes are metabolic sentinels that control blood flow through a KATP channel-dependent energy switch. Cell Rep. 2022 Dec 27;41(13).

45. Dalkara T, Gursoy-Ozdemir Y, Yemisci M. Brain microvascular pericytes in health and disease. Vol. 122, Acta Neuropathologica. 2011. p. 1–9.

46. Uemura MT, Maki T, Ihara M, Lee VMY, Trojanowski JQ. Brain Microvascular Pericytes in Vascular Cognitive Impairment and Dementia. Vol. 12, Frontiers in Aging Neuroscience. Frontiers Media S.A.; 2020.

47. Berthiaume AA, Schmid F, Stamenkovic S, Coelho-Santos V, Nielson CD, Weber B, et al. Pericyte remodeling is deficient in the aged brain and contributes to impaired capillary flow and structure. Nat Commun. 2022 Dec 1;13(1).

48. Kofler NM, Cuervo H, Uh MK, Murtomäki A, Kitajewski J. Combined deficiency of Notch1 and Notch3 causes pericyte dysfunction, models CADASIL, and results in arteriovenous malformations. Sci Rep. 2015 Nov 13;5.

49. Kisler K, Nelson AR, Rege S V., Ramanathan A, Wang Y, Ahuja A, et al. Pericyte degeneration leads to neurovascular uncoupling and limits

oxygen supply to brain. Nat Neurosci. 2017 Feb 23;20(3):406–16.

50. Török O, Schreiner B, Schaffenrath J, Tsai HC, Maheshwari U, Stifter SA, et al. Pericytes regulate vascular immune homeostasis in the CNS. Available from: https://doi.org/10.1073/pnas.2016587118

51. Stark K, Eckart A, Haidari S, Tirniceriu A, Lorenz M, Von Brühl ML, et al. Capillary and arteriolar pericytes attract innate leukocytes exiting through venules and 'instruct' them with pattern-recognition and motility programs. Nat Immunol. 2013 Jan;14(1):41–51.

52. Proebstl D, Voisin MB, Woodfin A, Whiteford J, D'Acquisto F, Jones GE, et al. Pericytes support neutrophil subendothelial cell crawling and breaching of venular walls in vivo. Journal of Experimental Medicine. 2012 Jun 4;209(6):1219–34.

53. Sweeney MD, Sagare AP, Zlokovic B V. Blood–brain barrier breakdown in Alzheimer disease and other neurodegenerative disorders. Nat Rev Neurol. 2018 Mar 29;14(3):133–50.

54. Winkler EA, Sengillo JD, Sagare AP, Zhao Z, Ma Q, Zuniga E, et al. Blood-spinal cord barrier disruption contributes to early motor-neuron degeneration in ALS-model mice. Proc Natl Acad Sci U S A. 2014 Mar 18;111(11).

55. Winkler EA, Sagare AP, Zlokovic B V. The pericyte: A forgotten cell type with important implications for alzheimer's disease? In: Brain Pathology. Blackwell Publishing Ltd; 2014. p. 371–86.

56. Ghosh M, Balbi M, Hellal F, Dichgans M, Lindauer U, Plesnila N. Pericytes are involved in the pathogenesis of cerebral autosomal dominant arteriopathy with subcortical infarcts and leukoencephalopathy. Ann Neurol. 2015 Dec 1;78(6):887–900.

57. Weller RO, Subash M, Preston SD, Mazanti I, Carare RO. Perivascular drainage of amyloid-β peptides from the brain and its failure in cerebral amyloid angiopathy and Alzheimer's disease. In: Brain Pathology. 2008. p. 253–66.

58. Dziewulska D, Lewandowska E. Pericytes as a new target for pathological processes in CADASIL.

Neuropathology. 2012 Oct;32(5):515–21.

59. Carare RO, Hawkes CA, Jeffrey M, Kalaria RN, Weller RO. Review: Cerebral amyloid angiopathy, prion angiopathy, CADASIL and the spectrum of protein elimination failure angiopathies (PEFA) in neurodegenerative disease with a focus on therapy. Neuropathol Appl Neurobiol. 2013 Oct;39(6):593–611.

60. Schreiber S, Bueche CZ, Garz C, Braun H. Blood brain barrier breakdown as the starting point of cerebral small vessel disease? - New insights from a rat model. Vol. 5, Experimental and Translational Stroke Medicine. 2013.

61. Fang C, Magaki SD, Kim RC, Kalaria RN, Vinters H V., Fisher M. Arteriolar neuropathology in cerebral microvascular disease. Vol. 49, Neuropathology and Applied Neurobiology. John Wiley and Sons Inc; 2023.

62. Zimmermann KW. Der Ieinere Bau der Blutcapillaren. 1923.

63. Birbrair A. Pericyte Biology - Novel Concepts [Internet]. Birbrair A, editor. Cham: Springer International Publishing; 2018. (Advances in Experimental Medicine and Biology; vol. 1109). Available from: http://link.springer.com/10.1007/978-3-030-02601-1

64. Yamazaki T, Mukouyama YS. Tissue Specific Origin, Development, and Pathological Perspectives of Pericytes. Vol. 5, Frontiers in Cardiovascular Medicine. Frontiers Media S.A.; 2018.

65. Baek SH, Maiorino E, Kim H, Glass K, Raby BA, Yuan K. Single Cell Transcriptomic Analysis Reveals Organ Specific Pericyte Markers and Identities. Front Cardiovasc Med. 2022 Jun 1;9.

66. Vanlandewijck M, He L, Mäe MA, Andrae J, Ando K, Del Gaudio F, et al. A molecular atlas of cell types and zonation in the brain vasculature. Nature. 2018 Feb 22;554(7693):475–80.

67. Bhattacharya A, Kaushik DK, Lozinski BM, Yong VW. Beyond barrier functions: Roles of pericytes in homeostasis and regulation of neuroinflammation. Vol. 98, Journal of Neuroscience Research. John Wiley and Sons Inc; 2020. p. 2390–405.

68. Smyth LCD, Rustenhoven J, Scotter EL, Schweder P, Faull RLM, Park TIH, et al. Markers for human brain pericytes and smooth muscle cells. J Chem Neuroanat. 2018 Oct 1;92:48–60.

69. Nikolakopoulou AM, Montagne A, Kisler K, Dai Z, Wang Y, Huuskonen MT, et al. Pericyte loss leads to circulatory failure and pleiotrophin depletion causing neuron loss. Nat Neurosci. 2019 Jul 1;22(7):1089–98.

70. Gautam J, Cao Y, Yao Y. Pericytic Laminin Maintains Blood-Brain Barrier Integrity in an Age-Dependent Manner. Transl Stroke Res. 2020 Apr 1;11(2):228–42.

71. Teichert M, Milde L, Holm A, Stanicek L, Gengenbacher N, Savant S, et al. Pericyte-expressed Tie2 controls angiogenesis and vessel maturation. Nat Commun. 2017 Jul 18;8.

72. Gaceb A, Özen I, Padel T, Barbariga M, Paul G. Pericytes secrete pro-regenerative molecules in response to platelet-derived growth factor-BB. Journal of Cerebral Blood Flow and Metabolism. 2018 Jan 1;38(1):45–57.

73. Saunders WB, Bohnsack BL, Faske JB, Anthis NJ, Bayless KJ, Hirschi KK, et al. Coregulation of vascular tube stabilization by endothelial cell TIMP-2 and pericyte TIMP-3. Journal of Cell Biology. 2006 Oct 9;175(1):179–91.

74. Yamanaka G, Takata F, Kataoka Y, Kanou K, Morichi S, Dohgu S, et al. The neuroinflammatory role of pericytes in epilepsy. Vol. 9, Biomedicines. MDPI AG; 2021.

75. Duan L, Zhang X Di, Miao WY, Sun YJ, Xiong G, Wu Q, et al. PDGFRβ Cells Rapidly Relay Inflammatory Signal from the Circulatory System to Neurons via Chemokine CCL2. Neuron. 2018 Oct 10;100(1):183-200.e8.

76. Rafalski VA, Merlini M, Akassoglou K. Pericytes: The Brain's Very First Responders? Vol. 100, Neuron. Cell Press; 2018. p. 11–3.

77. Barbaro NR, De Araújo TM, Tanus-Santos JE, Anhê GF, Fontana V, Moreno H. Vascular Damage in Resistant Hypertension: TNF-Alpha Inhibition Effects on Endothelial Cells. Biomed Res Int. 2015;2015.

78. Mozos I, Malainer C, Horbanczuk J, Gug C, Stoian D, Luca CT, et al. Inflammatory markers for arterial stiffness in cardiovascular diseases. Vol. 8, Frontiers in Immunology. Frontiers Media S.A.; 2017.

79. Matsumoto J, Takata F, Machida T, Takahashi H, Soejima Y, Funakoshi M, et al. Tumor necrosis factor-α-stimulated brain pericytes possess a unique cytokine and chemokine release profile and enhance microglial activation. Neurosci Lett. 2014 Aug 22;578:133–8.

80. Colonna M, Butovsky O. Microglia Function in the Central Nervous System During Health and Neurodegeneration. 2017; Available from: https://doi.org/10.1146/annurev-immunol-

81. Hammond TR, Dufort C, Dissing-Olesen L, Giera S, Young A, Wysoker A, et al. Single-Cell RNA Sequencing of Microglia throughout the Mouse Lifespan and in the Injured Brain Reveals Complex Cell-State Changes. Immunity. 2019 Jan 15;50(1):253-271.e6.

82. Hickman S, Izzy S, Sen P, Morsett L, El Khoury J. Microglia in neurodegeneration. Vol. 21, Nature Neuroscience. Nature Publishing Group; 2018. p. 1359–69.

83. Stratoulias V, Venero JL, Tremblay M, Joseph B. Microglial subtypes: diversity within the microglial community. EMBO J. 2019 Sep 2;38(17).

84. Honarpisheh P, Lee J, Banerjee A, Blasco-Conesa MP, Honarpisheh P, d'Aigle J, et al. Potential caveats of putative microglia-specific markers for assessment of age-related cerebrovascular neuroinflammation. J Neuroinflammation. 2020 Dec 1;17(1).

85. Toledano Furman N, Gottlieb A, Prabhakara KS, Bedi S, Caplan HW, Ruppert KA, et al. High-resolution and differential analysis of rat microglial markers in traumatic brain injury: conventional flow cytometric and bioinformatics analysis. Sci Rep. 2020 Dec 1;10(1).

86. Morton L, Arndt P, Garza AP, Henneicke S, Mattern H, Gonzalez M, et al. Spatio-temporal dynamics of microglia phenotype in human and murine cSVD: impact of acute and chronic hypertensive states. Acta

Neuropathol Commun. 2023 Dec 1;11(1).

87. Bendorius M, Po C, Muller S, Jeltsch-David H. From systemic inflammation to neuroinflammation: The case of neurolupus. Vol. 19, International Journal of Molecular Sciences. MDPI AG; 2018.

88. Haruwaka K, Ikegami A, Tachibana Y, Ohno N, Konishi H, Hashimoto A, et al. Dual microglia effects on blood brain barrier permeability induced by systemic inflammation. Nat Commun. 2019 Dec 1;10(1).

89. Domingues HS, Portugal CC, Socodato R, Relvas JB. Oligodendrocyte, astrocyte, and microglia crosstalk in myelin development, damage, and repair. Vol. 4, Frontiers in Cell and Developmental Biology. Frontiers Media S.A.; 2016.

90. Leng F, Edison P. Neuroinflammation and microglial activation in Alzheimer disease: where do we go from here? Vol. 17, Nature Reviews Neurology. Nature Research; 2021. p. 157–72.

91. Paolicelli RC, Sierra A, Stevens B, Tremblay ME, Aguzzi A, Ajami B, et al. Microglia states and nomenclature: A field at its crossroads. Vol. 110, Neuron. Cell Press; 2022. p. 3458–83.

92. Császár E, Lénárt N, Cserép C, Környei Z, Fekete R, Pósfai B, et al. Microglia modulate blood flow, neurovascular coupling, and hypoperfusion via purinergic actions. Journal of Experimental Medicine. 2022 Mar 7;219(3).

93. Lou N, Takano T, Pei Y, Xavier AL, Goldman SA, Nedergaard M. Purinergic receptor P2RY12-dependent microglial closure of the injured blood-brain barrier. Proc Natl Acad Sci U S A. 2016 Jan 26;113(4):1074–9.

94. Moore CS, Ase AR, Kinsara A, Rao VTS, Robinson MM, Leong SY, et al. P2Y12 expression and function in alternatively activated human microglia. Neurol Neuroimmunol Neuroinflamm. 2015 Apr 1;2(2):e80.

95. Masuda T, Sankowski R, Staszewski O, Prinz M. Microglia Heterogeneity in the Single-Cell Era. Vol. 30, Cell Reports. Elsevier B.V.; 2020. p. 1271–81.

96. Masuda T, Sankowski R, Staszewski O, Böttcher C, Amann L, Sagar, et al. Spatial and temporal heterogeneity of

mouse and human microglia at single-cell resolution. Nature. 2019 Feb 21;566(7744):388–92.

97. Keren-Shaul H, Spinrad A, Weiner A, Matcovitch-Natan O, Dvir-Szternfeld R, Ulland TK, et al. A Unique Microglia Type Associated with Restricting Development of Alzheimer's Disease. Cell. 2017 Jun 15;169(7):1276-1290.e17.

98. Tay TL, Mai D, Dautzenberg J, Fernández-Klett F, Lin G, Sagar S, et al. A new fate mapping system reveals context-dependent random or clonal expansion of microglia. Nat Neurosci. 2017 Jun 1;20(6):793–803.

99. Buzas EI. The roles of extracellular vesicles in the immune system. Nature Reviews Immunology. Nature Research; 2022.

100. Crewe C, Funcke JB, Li S, Joffin N, Gliniak CM, Ghaben AL, et al. Extracellular vesicle-based interorgan transport of mitochondria from energetically stressed adipocytes. Cell Metab. 2021 Sep 7;33(9):1853-1868.e11.

101. Welsh JA, Goberdhan DCI, O'Driscoll L, Buzas EI, Blenkiron C, Bussolati B, et al. Minimal information for studies of extracellular vesicles (MISEV2023): From basic to advanced approaches. J Extracell Vesicles. 2024 Feb 1;13(2).

102. Van Niel G, D'Angelo G, Raposo G. Shedding light on the cell biology of extracellular vesicles. Vol. 19, Nature Reviews Molecular Cell Biology. Nature Publishing Group; 2018. p. 213–28.

103. Prusiner SB, Woerman AL, Mordes DA, Watts JC, Rampersaud R, Berry DB, et al. Evidence for α-synuclein prions causing multiple system atrophy in humans with parkinsonism. Proc Natl Acad Sci U S A. 2015 Sep 22;112(38):E5308–17.

104. Aguzzi A, Rajendran L. The Transcellular Spread of Cytosolic Amyloids, Prions, and Prionoids. Vol. 64, Neuron. 2009. p. 783–90.

105. Hill AF. Extracellular vesicles and neurodegenerative diseases. Vol. 39, Journal of Neuroscience. Society for Neuroscience; 2019. p. 9269–73.

106. Urabe F, Kosaka N, Ito K, Kimura T, Egawa S, Ochiya T. Extracellular vesicles as biomarkers and therapeutic targets for cancer. Extracellular Vesicles in Cell Physiology Am J

Physiol Cell Physiol [Internet]. 2020;318:29–39. Available from: www.ajpcell.org

107. Asai H, Ikezu S, Tsunoda S, Medalla M, Luebke J, Haydar T, et al. Depletion of microglia and inhibition of exosome synthesis halt tau propagation. Nat Neurosci. 2015 Nov 1;18(11):1584–93.

108. Yamamoto S, Niida S, Azuma E, Yanagibashi T, Muramatsu M, Huang TT, et al. Inflammation-induced endothelial cell-derived extracellular vesicles modulate the cellular status of pericytes. Sci Rep. 2015;5.

109. Yuan X, Wu Q, Wang P, Jing Y, Yao H, Tang Y, et al. Exosomes Derived From Pericytes Improve Microcirculation and Protect Blood–Spinal Cord Barrier After Spinal Cord Injury in Mice. Front Neurosci. 2019 Apr 16;13.

110. Jiang Y, Hong S, Zhu X, Zhang L, Tang H, Jordan KL, et al. IL-10 partly mediates the ability of MSC-derived extracellular vesicles to attenuate myocardial damage in experimental metabolic renovascular hypertension. Front Immunol. 2022 Sep 20;13.

111. Pascal R. Life, metabolism and energy. In: Astrochemistry and Astrobiology. Springer Berlin Heidelberg; 2013. p. 243–69.

112. Antonio Blanco GB. Medical Biochemistry. 1st ed. 2017.

113. Brier MR, Blazey T, Raichle ME, Morris JC, Benzinger TLS, Vlassenko AG, et al. Increased white matter glycolysis in humans with cerebral small vessel disease. Nat Aging. 2022 Nov 1;2(11):991–9.

114. Goyal MS, Vlassenko AG, Blazey TM, Su Y, Couture LE, Durbin TJ, et al. Loss of Brain Aerobic Glycolysis in Normal Human Aging. Cell Metab. 2017 Aug 1;26(2):353-360.e3.

115. Magistretti PJ. Imaging brain aerobic glycolysis as a marker of synaptic plasticity. Vol. 113, Proceedings of the National Academy of Sciences of the United States of America. National Academy of Sciences; 2016. p. 7015–6.

116. Fox NC, Schott JM. Imaging cerebral atrophy: normal ageing to Alzheimer's disease. The Lancet. 2004 Jan;363(9406):392–4.

117. Goyal MS, Hawrylycz M, Miller JA, Snyder AZ, Raichle ME. Aerobic

glycolysis in the human brain is associated with development and neotenous gene expression. Cell Metab. 2014 Jan 7;19(1):49–57.

118. Raichle ME. The restless brain: how intrinsic activity organizes brain function. Philosophical Transactions of the Royal Society B: Biological Sciences. 2015 May 19;370(1668):20140172.

119. Goyal MS, Blazey T, Metcalf N V., McAvoy MP, Strain JF, Rahmani M, et al. Brain aerobic glycolysis and resilience in Alzheimer disease. Proc Natl Acad Sci U S A. 2023 Feb 14;120(7).

120. Mustapha M, Nassir CMNCM, Aminuddin N, Safri AA, Ghazali MM. Cerebral Small Vessel Disease (CSVD) – Lessons From the Animal Models. Vol. 10, Frontiers in Physiology. Frontiers Media S.A.; 2019.

121. Hazama F, Chue C -H, Kataoka H, Sasahara M, Amano S. PATHOGENESIS OF LACUNA-LIKE CYST FORMATION AND DIFFUSE DEGENERATION OF THE WHITE MATTER IN THE BRAIN OF STROKE-PRONE SPONTANEOUSLY HYPERTENSIVE RATS. Clin Exp Pharmacol Physiol. 1995;22:S260–1.

122. Okamoto K, Aoki K. Development of a Strain of Spontaneously Hypertensive Rats. Jpn Circ J. 1963;27(3):282–93.

123. Okamoto K, Yamori Y, Nagaoka A. Establishment of the stroke-prone spontaneously hypertensive rat (SHR). Circ Res. 1974;

124. Shibota M, Akinobu N, Akio Shino, Takeshi Fujita. Renin-angiotensin system in stroke-prone spontaneously hypertensive rats. 1979;

125. Nabika T, Ohara H, Kato N, Isomura M. The stroke-prone spontaneously hypertensive rat: Still a useful model for post-GWAS genetic studies? Vol. 35, Hypertension Research. 2012. p. 477–84.

126. Yamori Y, Horie R, Handa H, Sato M, Fukase M. Pathogenetic Similarity of Strokes in Stroke-Prone Spontaneously Hypertensive Rats and Humans. Stroke [Internet]. 1976; Available from: http://ahajournals.org

127. Yamori Y, Horie R. Developmental Course of Hypertension and Regional Cerebral Blood Flow in Stroke-prone

Spontaneously Hypertensive Rats. Stroke [Internet]. 1977; Available from: http://ahajournals.org

128. Henning EC, Warach S, Spatz M. Hypertension-induced vascular remodeling contributes to reduced cerebral perfusion and the development of spontaneous stroke in aged SHRSP rats. Journal of Cerebral Blood Flow and Metabolism. 2010 Apr;30(4):827–36.

129. Obata JE, Nakamura T, Takano H, Naito A, Kimura H, Yoshida Y, et al. Increased gene expression of components of the renin± angiotensin system in glomeruli of genetically hypertensive rats [Internet]. Vol. 18, Journal of Hypertension. 1247±1255 & Lippincott Williams & Wilkins; 2000. Available from: http://journals.lww.com/jhypertension

130. Kim S, Tokuyama M, Hosoi M, Yamamoto K. Original Contributions Adrenal and Circulating Renin-Angiotensin System in Stroke-Prone Hypertensive Rats. Hypertension [Internet]. 1992; Available from: http://ahajournals.org

131. Rentzsch B, Todiras M, Iliescu R, Popova E, Campos LA, Oliveira ML, et al. Transgenic angiotensin-converting enzyme 2 overexpression in vessels of SHRSP rats reduces blood pressure and improves endothelial function. Hypertension. 2008 Nov;52(5):967–73.

132. Jesmin S, Sakuma I, Togashi H, Yamaguchi T, Ueno KI, Yoshioka M, et al. Altered Expression of Endothelin and its Receptors in the Brain of SHR-SP at Malignant Hypertensive Stage [Internet]. Vol. 44, J Cardiovasc Pharmacol^{TM} •. 2004. Available from: http://journals.lww.com/cardiovascularpharm

133. Daneshtalab N, Smeda JS. Alterations in the modulation of cerebrovascular tone and blood flow by nitric oxide synthases in SHRsp with stroke. Cardiovasc Res. 2010 Apr;86(1):160–8.

134. Schreiber S, Bueche CZ, Garz C, Kropf S, Angenstein F, Goldschmidt J, et al. The pathologic cascade of cerebrovascular lesions in SHRSP: Is erythrocyte accumulation an early phase. Journal of Cerebral Blood Flow and Metabolism. 2012 Feb;32(2):278–90.

135. Bailey EL, Wardlaw JM, Graham D, Dominiczak AF, Sudlow CLM, Smith C. Cerebral small vessel endothelial structural changes predate hypertension in stroke-prone spontaneously hypertensive rats: A blinded, controlled immunohistochemical study of 5- to 21-week-old rats. Neuropathol Appl Neurobiol. 2011 Dec;37(7):711–26.

136. Wardlaw JM, Smith C, Dichgans M. Mechanisms of sporadic cerebral small vessel disease: insights from neuroimaging [Internet]. Vol. 12, www.thelancet.com/neurology. 2013. Available from: www.thelancet.com/neurology

137. Fredriksson K, Nordborg C, Kalimo H, Johansson BB. Cerebral microangiopathy in stroke-prone spontaneously hypertensive rats* An immunohistochemical and ultrastructural study. Acta Neuropathologica . 1988;75:241–52.

138. Braun H, Schreiber S. Microbleeds in cerebral small vessel disease. Lancet Neurol. 2013 Aug;12(8):735–6.

139. Lee JM, Zhai G, Liu Q, Gonzales ER, Yin K, Yan P, et al. Vascular permeability precedes spontaneous intracerebral hemorrhage in stroke-prone spontaneously hypertensive rats. Stroke. 2007 Dec;38(12):3289–91.

140. Bailey EL, Mcbride MW, Beattie W, Mcclure JD, Graham D, Dominiczak AF, et al. Differential gene expression in multiple neurological, inflammatory and connective tissue pathways in a spontaneous model of human small vessel stroke. Neuropathol Appl Neurobiol. 2014 Dec 1;40(7):855–72.

141. Jandke S, Garz C, Schwanke D, Sendtner M, Heinze HJ, Carare RO, et al. The association between hypertensive arteriopathy and cerebral amyloid angiopathy in spontaneously hypertensive stroke-prone rats. Brain Pathology. 2018 Nov 1;28(6):844–59.

142. Mustapha M, Nassir CMNCM, Aminuddin N, Safri AA, Ghazali MM. Cerebral Small Vessel Disease (CSVD) – Lessons From the Animal Models. Vol. 10, Frontiers in Physiology. Frontiers Media S.A.; 2019.

143. Jandke S, Garz C, Schwanke D, Sendtner M, Heinze HJ, Carare RO, et al. The association between hypertensive arteriopathy and cerebral amyloid angiopathy in spontaneously

hypertensive stroke-prone rats. Brain Pathology. 2018 Nov 1;28(6):844–59.

144. Bailey EL, Wardlaw JM, Graham D, Dominiczak AF, Sudlow CLM, Smith C. Cerebral small vessel endothelial structural changes predate hypertension in stroke-prone spontaneously hypertensive rats: A blinded, controlled immunohistochemical study of 5- to 21-week-old rats. Neuropathol Appl Neurobiol. 2011 Dec;37(7):711–26.

145. Held F, Morris A, W. J., Pirici D, Niklass S, Sharp, et al. Vascular basement membrane alterations and β-amyloid accumulations in an animal model of cerebral small vessel disease. Clin Sci. 2017;

146. Kaiser D, Weise G, Möller K, Scheibe J, Pösel C, Baasch S, et al. Spontaneous white matter damage, cognitive decline and neuroinflammation in middle-aged hypertensive rats: An animal model of early-stage cerebral small vessel disease. Acta Neuropathol Commun. 2014 Jan 27;2(1).

147. Crouch EE, Doetsch F. FACS isolation of endothelial cells and pericytes from mouse brain microregions. Nat Protoc. 2018 Apr 1;13(4):738–51.

148. Nakagawa S, Deli MA, Kawaguchi H, Shimizudani T, Shimono T, Kittel Á, et al. A new blood-brain barrier model using primary rat brain endothelial cells, pericytes and astrocytes. Neurochem Int. 2009 Mar;54(3–4):253–63.

149. Lee YK, Uchida H, Smith H, Ito A, Sanchez T. The isolation and molecular characterization of cerebral microvessels. Nat Protoc. 2019 Nov 1;14(11):3059–81.

150. Livak KJ, Schmittgen TD. Analysis of relative gene expression data using real-time quantitative PCR and the 2-ΔΔCT method. Methods. 2001;25(4):402–8.

151. Shihan MH, Novo SG, Le Marchand SJ, Wang Y, Duncan MK. A simple method for quantitating confocal fluorescent images. Biochem Biophys Rep. 2021 Mar 1;25.

152. Garza AP, Morton L, Pállinger É, Buzás EI, Schreiber S, Schott BH, et al. Initial and ongoing tobacco smoking elicits vascular damage and distinct inflammatory response linked to

neurodegeneration. Brain Behav Immun Health. 2023 Mar 1;28.

153. Debska-Vielhaber G, Miller I, Peeva V, Zuschratter W, Walczak J, Schreiber S, et al. Impairment of mitochondrial oxidative phosphorylation in skin fibroblasts of SALS and FALS patients is rescued by in vitro treatment with ROS scavengers. Exp Neurol. 2021 May 1;339.

154. Braak H, Braak E. Acta H ' pathologica Neuropathological stageing of Alzheimer-related changes. Vol. 82, Acta Neuropathol. 1991.

155. Braak H, Tredici K Del, Rüb U, De Vos RAI, Jansen Steur ENH, Braak E. Staging of brain pathology related to sporadic Parkinson's disease. Vol. 24, Neurobiology of Aging. 2003.

156. Forsberg KME, Zhang Y, Reiners J, Ander M, Niedermayer A, Fang L, et al. Endothelial damage, vascular bagging and remodeling of the microvascular bed in human microangiopathy with deep white matter lesions. Acta Neuropathol Commun. 2018 Nov 23;6(1):128.

157. Yilmazer-Hanke D, Mayer T, Müller HP, Neugebauer H, Abaei A, Scheuerle A, et al. Histological correlates of postmortem ultra-high-resolution single-section MRI in cortical cerebral microinfarcts. Acta Neuropathol Commun. 2020 Mar 13;8(1).

158. Tomimoto H. Subcortical vascular dementia. Vol. 71, Neuroscience Research. 2011. p. 193–9.

159. Choy F, Wong C, Yatawara C, Low A, Foo H, Yi B, et al. Cerebral Small Vessel Disease Influences Hippocampal Subfield Atrophy in Mild Cognitive Impairment. Available from: http://surfer.nmr.mgh.harvard.

160. Lee PL, Kuo CY, Wang PN, Chen LK, Lin CP, Chou KH, et al. Regional rather than global brain age mediates cognitive function in cerebral small vessel disease. Brain Commun. 2022;4(5).

161. Mattern H. Openly available sMall vEsseL sEgmenTaTion pipelinE (OMELETTE). Openly available sMall vEsseL sEgmenTaTion pipelinE (OMELETTE). Proc. Intl. Soc. Mag. Reson. Med. virtual meeting: ISMRM; 2021.

162. Frangi AF, Niessen WJ, Vincken KL, Viergever MA. Multiscale Vessel Enhancement Filtering*.

163. Fraz MM, Basit A, Remagnino P, Hoppe A, Barman SA. Retinal vasculature segmentation by morphological curvature, reconstruction and adapted hysteresis thresholding. In: 2011 7th International Conference on Emerging Technologies, ICET 2011. 2011.

164. N. Otsu. A Threshold Selection Method from Gray-Level Histograms. IEEE Trans Syst Man Cybern. 1979 Jan;9(1):62–6.

165. York EM, Ledue JM, Bernier LP, Macvicar BA. 3dmorph automatic analysis of microglial morphology in three dimensions from ex vivo and in vivo imaging. eNeuro. 2018 Nov 1;5(6).

166. Martin E, El-Behi M, Fontaine B, Delarasse C. Analysis of microglia and monocyte-derived macrophages from the central nervous system by flow cytometry. Journal of Visualized Experiments. 2017 Jun 22;2017(124).

167. Sedgwick JD, Schwender S, Imrich H, D6rries R, Butchert GW. Isolation and direct characterization of resident microglial cells from the normal and inflamed central nervous system (encephalomyelitis/macrophage/antigen-presenting ceII/coronavirus/autolmmunity). Vol. 88, Proc. Nadl. Acad. Sci. USA. 1991.

168. Van Wageningen TA, Vlaar E, Kooij G, Jongenelen CAM, Geurts JJG, Van Dam AM. Regulation of microglial TMEM119 and P2RY12 immunoreactivity in multiple sclerosis white and grey matter lesions is dependent on their inflammatory environment. Acta Neuropathol Commun. 2019 Dec 11;7(1).

169. Brummelman J, Haftmann C, Núñez NG, Alvisi G, Mazza EMC, Becher B, et al. Development, application and computational analysis of high-dimensional fluorescent antibody panels for single-cell flow cytometry. Nat Protoc. 2019 Jul 1;14(7):1946–69.

170. Mair F, Hartmann FJ, Mrdjen D, Tosevski V, Krieg C, Becher B. The end of gating? An introduction to automated analysis of high dimensional cytometry data. Eur J Immunol. 2016 Jan 1;46(1):34–43.

171. Kirkman DL, Robinson AT, Rossman MJ, Seals DR, Edwards DG.

Mitochondrial contributions to vascular endothelial dysfunction, arterial stiffness, and cardiovascular diseases. Vol. 320, American Journal of Physiology - Heart and Circulatory Physiology. American Physiological Society; 2021. p. H2080–100.

172. Roesch S, Rapp C, Dettling S, Herold-Mende C. When immune cells turn bad—tumor-associated microglia/macrophages in glioma. Vol. 19, International Journal of Molecular Sciences. MDPI AG; 2018.

173. Gyoneva S, Hosur R, Gosselin D, Zhang B, Ouyang Z, Cotleur AC, et al. Cx3cr1-deficient microglia exhibit a premature aging transcriptome. Life Sci Alliance. 2019;2(6).

174. Sheffield LG, J Berman NE, J Microglial NE. Microglial Expression of MHC Class II Increases in Normal Aging of Nonhuman Primates. 1998.

175. Vagaska B, New SEP, Alvarez-Gonzalez C, D'Acquisto F, Gomez SG, Bulstrode NW, et al. MHC-class-II are expressed in a subpopulation of human neural stem cells in vitro in an IFNÎ 3-independent fashion and during development. Sci Rep. 2016 Apr 15;6.

176. Han X, Liu YJ, Liu BW, Ma ZL, Xia TJ, Gu XP. TREM2 and CD163 Ameliorate Microglia-Mediated Inflammatory Environment in the Aging Brain. Journal of Molecular Neuroscience. 2022 May 1;72(5):1075–84.

177. Biswas SK. Metabolic Reprogramming of Immune Cells in Cancer Progression. Vol. 43, Immunity. Cell Press; 2015. p. 435–49.

178. Pålsson-McDermott EM, O'Neill LAJ. Targeting immunometabolism as an anti-inflammatory strategy. Vol. 30, Cell Research. Springer Nature; 2020. p. 300–14.

179. Pereira FE, Cronin C, Ghosh M, Zhou SY, Agosto M, Subramani J, et al. CD13 is essential for inflammatory trafficking and infarct healing following permanent coronary artery occlusioninmice. Cardiovasc Res. 2013 Oct 1;100(1):74–83.

180. Ghosh M, Gerber C, Rahman MM, Vernier KM, Pereira FE, Subramani J, et al. Molecular mechanisms regulating CD13-mediated adhesion. Immunology. 2014;142(4):636–47.

181. Ito M, Oliveriot MI, Mannont PJ, Bestt CF, Maeda N, Smithies O, et al.

Regulation of blood pressure by the type 1A angiotensin II receptor gene (gene targeting/G protein-coupled receptor/hypertension) [Internet]. Vol. 92, Genetics. 1995. Available from: https://www.pnas.org

182. Nataraj C, Oliverio MI, Mannon RB, Mannon PJ, Audoly LP, Amuchastegui CS, et al. Angiotensin II regulates cellular immune responses through a calcineurin-dependent pathway. Journal of Clinical Investigation. 1999;104(12):1693–701.

183. Benigni A, Corna D, Zoja C, Sonzogni A, Latini R, Salio M, et al. Disruption of the Ang II type 1 receptor promotes longevity in mice. Journal of Clinical Investigation. 2009 Mar 2;119(3):524–30.

184. Paillard F, Chansel D, Brand E, Benetos A, Thomas F, Czekalski S, et al. Genotype-Phenotype Relationships for the Renin-Angiotensin-Aldosterone System in a Normal Population [Internet]. 1999. Available from: http://www.hypertensionaha.org

185. Cober ND, Mccourt E, Soares Godoy R, Deng Y, Schlosser K, Situ A, et al. Emergence of disease specific endothelial and stromal cell populations involved in arterial remodeling during development of pulmonary arterial hypertension. Available from: https://doi.org/10.1101/2023.09.06.555321

186. Wang YY, Pan LY, Moens CB, Appel B. Notch3 establishes brain vascular integrity by regulating pericyte number. Development (Cambridge). 2014 Jan 15;141(2):307–17.

187. Tefft JB, Bays JL, Lammers A, Kim S, Eyckmans J, Chen CS. Notch1 and Notch3 coordinate for pericyte-induced stabilization of vasculature. Am J Physiol Cell Physiol. 2022 Feb 1;322(2):C185–96.

188. Rajashree Rana, Tianfang Huang, Georgios Koukos, Elizabeth K. Fletcher, Susan E. Turner, Andrew Shearer, et al. Noncanonical Matrix Metalloprotease 1-Protease Activated Receptor 1 Signaling Drives Progression of Atherosclerosis. Arterioscler Thromb Vasc Biol. 2018;

189. Boyalla V, Gallego-Colon E, Spartalis M. Immunity and inflammation in cardiovascular disorders. Vol. 23, BMC Cardiovascular Disorders. BioMed Central Ltd; 2023.

190. Piaszyk-Borychowska A, Széles L, Csermely A, Chiang HC, Wesoły J, Lee CK, et al. Signal integration of IFN-I and IFN-II with TLR4 involves sequential recruitment of STAT1-Complexes and NFκB to enhance pro-inflammatory transcription. Front Immunol. 2019;10(JUN).

191. Brasier AR. The nuclear factor-B-interleukin-6 signalling pathway mediating vascular inflammation. Vol. 86, Cardiovascular Research. 2010. p. 211–8.

192. Warner SJC, Auger KR, Libby P. Human interleukin 1 induces interleukin 1 gene expression in human vascular smooth muscle cells. Journal of Experimental Medicine [Internet]. 1987; Available from: http://rupress.org/jem/article-pdf/165/5/1316/1667615/1316.pdf

193. Khyzha N, Khor M, Distefano P V, Wang L, Matic L, Hedin U, et al. Regulation of CCL2 expression in human vascular endothelial cells by a neighboring divergently transcribed long noncoding RNA. PNAS [Internet]. 2019; Available from: www.pnas.org/lookup/suppl/doi:10.

194. Elhage R, Ljunggren HG, Hansson GK. Proatherogenic role of interleukin-18: Effects on inflammation and action on vascular cells. Vol. 96, Cardiovascular Research. 2012. p. 176–80.

195. Kim HY, Kim HS. IL-10 up-regulates CCL5 expression in vascular smooth muscle cells from spontaneously hypertensive rats. Cytokine. 2014;68(1):40–9.

196. Ebrahem Q, Chaurasia SS, Vasanji A, Qi JH, Klenotic PA, Cutler A, et al. Cross-talk between vascular endothelial growth factor and matrix metalloproteinases in the induction of neovascularization in vivo. American Journal of Pathology. 2010;176(1):496–503.

197. Lee S, Jilan SM, Nikolova G V., Carpizo D, Luisa Iruela-Arispe M. Processing of VEGF-A by matrix metalloproteinases regulates bioavailability and vascular patterning in tumors. Journal of Cell Biology. 2005 May;169(4):681–91.

198. Ahmad A, Nawaz MI. Molecular mechanism of VEGF and its role in pathological angiogenesis. Vol. 123,

Journal of Cellular Biochemistry. John Wiley and Sons Inc; 2022. p. 1938–65.

199. Tsang CK wan, Liu Y, Thomas J, Zhang Y, Zheng XFS. Superoxide dismutase 1 acts as a nuclear transcription factor to regulate oxidative stress resistance. Nat Commun. 2014;5:3446.

200. Griendling KK, Camargo LL, Rios FJ, Alves-Lopes R, Montezano AC, Touyz RM. Oxidative Stress and Hypertension. Vol. 128, Circulation Research. Lippincott Williams and Wilkins; 2021. p. 993–1020.

201. Ide T, Tsutsui H, Kinugawa S, Utsumi H, Kang D, Hattori N, et al. Mitochondrial Electron Transport Complex I Is a Potential Source of Oxygen Free Radicals in the Failing Myocardium [Internet]. 1999. Available from: http://www.circresaha.org

202. Santisteban MM, Iadecola C, Carnevale D. Hypertension, Neurovascular Dysfunction, and Cognitive Impairment. Vol. 80, Hypertension. Lippincott Williams and Wilkins; 2023. p. 22–34.

203. Presa JL, Saravia F, Bagi Z, Filosa JA. Vasculo-Neuronal Coupling and Neurovascular Coupling at the Neurovascular Unit: Impact of Hypertension. Vol. 11, Frontiers in Physiology. Frontiers Media S.A.; 2020.

204. Youwakim J, Vallerand D, Girouard H. Neurovascular Coupling in Hypertension Is Impaired by IL-17A through Oxidative Stress. Int J Mol Sci. 2023 Feb 1;24(4).

205. Ward PS, Thompson CB. Metabolic Reprogramming: A Cancer Hallmark Even Warburg Did Not Anticipate. Vol. 21, Cancer Cell. Cell Press; 2012. p. 297–308.

206. Wang Y, Patti GJ. The Warburg effect: a signature of mitochondrial overload. Vol. 33, Trends in Cell Biology. Elsevier Ltd; 2023. p. 1014–20.

207. Streit WJ, Mrak RE, Griffin WST. Microglia and neuroinflammation: A pathological perspective. J Neuroinflammation. 2004 Jul 30;1.

208. Tang Y, Le W. Differential Roles of M1 and M2 Microglia in Neurodegenerative Diseases. Vol. 53, Molecular Neurobiology. Humana Press Inc.; 2016. p. 1181–94.

209. Merlini M, Rafalski VA, Rios Coronado PE, Gill TM, Ellisman M,

Muthukumar G, et al. Fibrinogen Induces Microglia-Mediated Spine Elimination and Cognitive Impairment in an Alzheimer's Disease Model. Neuron. 2019 Mar 20;101(6):1099-1108.e6.

210. Kaushik R, Morkovin E, Schneeberg J, Confettura AD, Kreutz MR, Senkov O, et al. Traditional Japanese Herbal Medicine Yokukansan Targets Distinct but Overlapping Mechanisms in Aged Mice and in the 5xFAD Mouse Model of Alzheimer's Disease. Front Aging Neurosci. 2018 Dec 17;10.

211. Solé-Guardia G, Custers E, de Lange A, Clijncke E, Geenen B, Gutierrez J, et al. Association between hypertension and neurovascular inflammation in both normal-appearing white matter and white matter hyperintensities. Acta Neuropathol Commun. 2023 Dec 1;11(1).

212. Arvanitakis Z, Capuano AW, Leurgans SE, Buchman AS, Bennett DA, Schneider JA. The Relationship of Cerebral Vessel Pathology to Brain Microinfarcts. Brain Pathology. 2017 Jan 1;27(1):77–85.

213. Evans LE, Taylor JL, Smith CJ, Pritchard HAT, Greenstein AS, Allan SM. Cardiovascular comorbidities, inflammation, and cerebral small vessel disease. Vol. 117, Cardiovascular Research. Oxford University Press; 2021. p. 2575–88.

214. Hamilton OKL, Backhouse E V., Janssen E, Jochems ACC, Maher C, Ritakari TE, et al. Cognitive impairment in sporadic cerebral small vessel disease: A systematic review and meta-analysis. Alzheimer's and Dementia. 2021 Apr 1;17(4):665–85.

215. Montagne A, Barnes SR, Sweeney MD, Halliday MR, Sagare AP, Zhao Z, et al. Blood-Brain barrier breakdown in the aging human hippocampus. Neuron. 2015 Jan 21;85(2):296–302.

216. Strassburger TL, Lee HC, Daly EM, Szczepanik J, Krasuski JS, Mentis MJ, et al. Interactive effects of age and hypertension on volumes of brain structures. Stroke. 1997;28(7):1410–7.

217. Mathys H, Adaikkan C, Gao F, Young JZ, Manet E, Hemberg M, et al. Temporal Tracking of Microglia Activation in Neurodegeneration at Single-Cell Resolution. Cell Rep. 2017 Oct 10;21(2):366–80.

218. Sun H, He X, Tao X, Hou T, Chen M, He M, et al. The CD200/CD200R signaling pathway contributes to spontaneous functional recovery by enhancing synaptic plasticity after stroke. J Neuroinflammation. 2020 May 30;17(1).

219. Manich G, Recasens M, Valente T, Almolda B, González B, Castellano B. Role of the CD200-CD200R Axis During Homeostasis and Neuroinflammation. Vol. 405, Neuroscience. Elsevier Ltd; 2019. p. 118–36.

220. Mori S, Kato M, Fujishima M. Impaired maze learning and cerebral glucose utilization in aged hypertensive rats. Hypertension. 1995;25(4 I):545–53.

221. Wyss JM, Chambless BD, Kadish I, Van Groen T. Age-related decline in water maze learning and memory in rats: strain differences [Internet]. 2000. Available from: www.elsevier.com/locate/neuaging

222. Johnson AC. Hippocampal Vascular Supply and Its Role in Vascular Cognitive Impairment. Vol. 54, Stroke. Wolters Kluwer Health; 2023. p. 673–85.

223. Kerkhofs D, Helgers R, Hermes D, Steinbusch HPJ, Van Essen H, Leenders P, et al. Amlodipine limits microglia activation and cognitive dysfunction in aged hypertensive mice. J Hypertens. 2023 Jul 1;41(7):1159–67.

224. Tayler HM, MacLachlan R, Güzel Ö, Miners JS, Love S. Elevated late-life blood pressure may maintain brain oxygenation and slow amyloid-β accumulation at the expense of cerebral vascular damage. Brain Commun. 2023;5(2).

225. Walker DG, Dalsing-Hernandez JE, Campbell NA, Lue LF. Decreased expression of CD200 and CD200 receptor in Alzheimer's disease: A potential mechanism leading to chronic inflammation. Exp Neurol. 2009 Jan;215(1):5–19.

226. Copland DA, Calder CJ, Raveney BJE, Nicholson LB, Phillips J, Cherwinski H, et al. Monoclonal antibody-mediated CD200 receptor signaling suppresses macrophage activation and tissue damage in experimental autoimmune uveoretinitis. American Journal of Pathology. 2007;171(2):580–8.

227. Meuth SG, Simon OJ, Grimm A, Melzer N, Herrmann AM, Spitzer P, et al. CNS inflammation and neuronal degeneration is aggravated by impaired CD200-CD200R-mediated macrophage silencing. J Neuroimmunol. 2008 Feb;194(1–2):62–9.

228. Zhang S, Wang XJ, Tian LP, Pan J, Lu GQ, Zhang YJ, et al. CD200-CD200R dysfunction exacerbates microglial activation and dopaminergic neurodegeneration in a rat model of Parkinson's disease. J Neuroinflammation. 2011 Nov 6;8.

229. Fang C, Magaki SD, Kim RC, Kalaria RN, Vinters H V., Fisher M. Arteriolar neuropathology in cerebral microvascular disease. Vol. 49, Neuropathology and Applied Neurobiology. John Wiley and Sons Inc; 2023.

230. Li X, Li C, Zhang W, Wang Y, Qian P, Huang H. Inflammation and aging: signaling pathways and intervention therapies. Vol. 8, Signal Transduction and Targeted Therapy. Springer Nature; 2023.

231. Shlesinger D, Hong KL, Shammas G, Page N, Sandu I, Agrafiotis A, et al. Single-cell immune repertoire sequencing of B and T cells in murine models of infection and autoimmunity. Genes Immun. 2022 Sep 1;23(6):183–95.

232. Bray CE, Witcher KG, Adekunle-Adegbite D, Ouvina M, Witzel M, Hans E, et al. Chronic Cortical Inflammation, Cognitive Impairment, and Immune Reactivity Associated with Diffuse Brain Injury Are Ameliorated by Forced Turnover of Microglia. Journal of Neuroscience. 2022 May 18;42(20):4215–28.

233. O'Neil SM, Witcher KG, McKim DB, Godbout JP. Forced turnover of aged microglia induces an intermediate phenotype but does not rebalance CNS environmental cues driving priming to immune challenge. Acta Neuropathol Commun. 2018 Nov 26;6(1):129.

234. O'Neil SM, Hans EE, Jiang S, Wangler LM, Godbout JP. Astrocyte immunosenescence and deficits in interleukin 10 signaling in the aged brain disrupt the regulation of microglia following innate immune activation. Glia. 2022 May 1;70(5):913–34.

235. Nomura A, Noto D, Murayama G, Chiba A, Miyake S. Unique primed status of microglia under the systemic autoimmune condition of lupus-prone mice. Arthritis Res Ther. 2019 Dec 30;21(1).

236. Monsorno K, Ginggen K, Ivanov A, Buckinx A, Lalive AL, Tchenio A, et al. Loss of microglial MCT4 leads to defective synaptic pruning and anxiety-like behavior in mice. Nat Commun. 2023 Dec 1;14(1).

237. Monsorno K, Buckinx A, Paolicelli RC. Microglial metabolic flexibility: emerging roles for lactate. Vol. 33, Trends in Endocrinology and Metabolism. Elsevier Inc.; 2022. p. 186–95.

238. Suzuki A, Stern SA, Bozdagi O, Huntley GW, Walker RH, Magistretti PJ, et al. Astrocyte-neuron lactate transport is required for long-term memory formation. Cell. 2011 Mar 4;144(5):810–23.

239. Tassinari ID, Rodrigues F da S, Bertram C, Mendes-da-Cruz DA, Guedes RP, Paz AH, et al. Lactate Protects Microglia and Neurons from Oxygen–Glucose Deprivation/Reoxygenation. Neurochem Res. 2024;

240. Sierra A, Paolicelli RC, Kettenmann H. Cien Años de Microglía: Milestones in a Century of Microglial Research. Trends Neurosci. 2019 Nov;42(11):778–92.

241. Paolicelli RC, Sierra A, Stevens B, Tremblay ME, Aguzzi A, Ajami B, et al. Microglia states and nomenclature: A field at its crossroads. Vol. 110, Neuron. Cell Press; 2022. p. 3458–83.

242. Cheng J, Zhang R, Xu Z, Ke Y, Sun R, Yang H, et al. Early glycolytic reprogramming controls microglial inflammatory activation. J Neuroinflammation. 2021 Dec 1;18(1).

243. Longhitano L, Vicario N, Forte S, Giallongo C, Broggi G, Caltabiano R, et al. Lactate modulates microglia polarization via IGFBP6 expression and remodels tumor microenvironment in glioblastoma. Cancer Immunology, Immunotherapy. 2023 Jan 1;72(1):1–20.

Declaration of honor

I hereby declare that I have written this dissertation titled

"Pericyte and Microglia Reprogramming in Hypertensive Cerebral Small Vessel Disease"

without the impermissible help of third parties and that none other than the aids indicated have been used; all sources of information are clearly marked, including my own publications.

I acknowledge that I received assistance for the collection and analysis of human post-mortem tissue. This assistance was limited to the collection and initial analysis of the tissue samples, and I have appropriately cited any data or insights derived from this collaboration.

In particular I have not consciously:

• fabricated data or rejected undesirable results,

• misused statistical methods with the aim of drawing other conclusions than those warranted by the available data

• plagiarized external data or publications

• presented the results of other researchers in a distorted way

I am aware that violations of copyright may lead to injunction and damage claims by the author and also to prosecution by law enforcement authorities. I hereby agree that the thesis may be electronically reviewed with the aim of identifying plagiarism. This work has not been submitted as a doctoral thesis in the same or a similar form in Germany, nor in any other country. It has not yet been published as a whole.

Magdeburg, June 04, 2024

Lorena Morton Moreno